Emerging Material Integration and Metrology for Ultra-Thin-Film High-Speed Photonic Devices

by Chandraman Patil

B.E. in Electronics Engineering, June 2017, Vidyalankar Institute of Technology, India
M.S. in Computer Engineering, May 2019, The George Washington University, USA

A Dissertation submitted to

The Faculty of
The School of Engineering and Applied Science
of The George Washington University
in partial fulfillment of the requirements
for the degree of Doctor of Philosophy

August 31, 2023

Dissertation directed by

Volker J. Sorger
Professor of Electrical and Computer Engineering

The School of Engineering and Applied Science of The George Washington University certifies that Chandraman Sadanand Patil has passed the Final Examination for the degree of Doctor of Philosophy as of June 13th, 2023. This is the final and approved form of the dissertation.

Emerging Material Integration and Metrology for Ultra-Thin-Film High-Speed Photonic Devices

Chandraman Sadanand Patil

Dissertation Research Committee:

Volker J. Sorger, Professor of Electrical and Computer Engineering, Dissertation Director

Shahrokh Ahmadi, Teaching Professor of Electrical and Computer Engineering, Committee Member

Hamed Dalir, Associate Professor of Electrical and Computer Engineering, University of Florida, Committee Member

Can Korman, Professor of Electrical and Computer Engineering, Committee Member

David Nagel, Research Professor of Electrical and Computer Engineering, Committee Member

© Copyright 2023 by Chandraman Sadanand Patil
All rights reserved.

Acknowledgments

I am immensely grateful to my parents and younger brother. Their constant support, sacrifice, and encouragement have been the pillars of my strength throughout this journey. Their belief in me, even during the most challenging times, has fueled my determination and inspired me to never give up. I am truly blessed to have such a loving and supportive family.

I would also like to thank my advisor, Professor Volker J. Sorger. His expertise, understanding, and unwavering commitment to research and development have been instrumental in shaping my doctoral journey. His guidance, mentorship, and enthusiasm for pushing the boundaries of knowledge have been invaluable. I am truly fortunate to have had the opportunity to work under his guidance. Additionally, I would like to express my gratitude to Professor Hamed Dalir. His guidance, support, and critical feedback have been invaluable in shaping the direction of my research. His expertise and thoughtful perspectives have challenged me to grow intellectually and have contributed significantly to the progress I have made.

Finally, I would like to thank me, for believing in me, I want to thank me for doing all this hard work. I want to thank me for having no days off. I want to thank me for never quitting. I want to thank me for always being a giver and trying to give more than I receive. I want to thank me for trying to do more right than wrong. I want to thank me for being always me.

Abstract

Emerging Material Integration and Metrology for Ultra-Thin-Film High-Speed Photonic Devices

This dissertation focuses on ultra-thin-film high-speed photonic devices that have emerged as a promising technology for various applications, including telecommunications, data centers, and optoelectronic sensing. This abstract presents an overview of the integration and metrology techniques employed to enable the development and optimization of these advanced photonic devices.

The integration of emerging materials plays a crucial role in the fabrication of ultra-thin-film photonic devices. These devices often rely on the integration of novel materials with unique optical and electronic properties, such as two-dimensional materials, quantum dots, transparent conductive oxides, or organic semiconductors. The successful integration of these materials requires careful consideration of compatibility, interface engineering, and deposition techniques to ensure high-performance device operation.

Additionally, accurate metrology techniques are vital for the characterization and optimization of ultra-thin-film photonic devices. Metrology methods, including spectroscopic ellipsometry, atomic force microscopy, and scanning electron microscopy, enable the measurement of critical parameters such as film thickness, roughness, and composition. Furthermore, advanced metrology techniques such as photoluminescence

spectroscopy and fabrication recipe optimization facilitate the investigation of optical properties, carrier dynamics, and device performance at ultra-fast timescales.

This dissertation highlights recent advancements in material integration and metrology techniques specifically tailored for ultra-thin-film high-speed photonic devices. It discusses the challenges associated with integrating novel materials into device architectures, as well as the importance of accurate metrology for device characterization. Novel development of techniques and tools for material integration will explain the novel outcomes in the form of the development of various optoelectronic devices using two-dimensional materials, topological insulators, transparent conductive oxide, and more. Furthermore, it emphasizes the need for continuous innovation in integration techniques and metrology methodologies to overcome the limitations of traditional fabrication processes and unlock the full potential of ultra-thin-film photonic devices. The integration of emerging materials and the development of robust metrology techniques are crucial steps toward the realization of high-performance ultra-thin-film photonic devices. These advancements have the potential to revolutionize various industries, enabling faster communication networks, more efficient data processing, and highly sensitive optoelectronic sensing systems. Continued research and development in this field will drive further progress in the integration and metrology techniques, ultimately paving the way for the widespread adoption of ultra-thin-film high-speed photonic devices in numerous applications.

Table of Contents

Acknowledgments ..... **iv**

Abstract ..... **v**

List of Figures ..... **x**

List of Tables ..... **xiii**

Introduction **1**

1.1 Background, Motivation & Problem Statements 1

1.2 Dissertation Outline 7

1.3 References - Chapter 1 9

Material Properties for Photonics **11**

1.4 Introduction 11

1.5 Transistion Di Metal Chalcogenides (TMDCs) 11

1.6 MXene 12

1.7 Topological Insulator 12

1.8 Transparent Conductive Oxide (TCO) 13

1.9 References - Chapter 2 15

Novel Material Integration Metrology and Methodologies Development **18**

1.10 Chip Substrate Preparation 18

1.11 Highly Accurate, Reliable, and Non-Contaminating Two-Dimensional Material Transfer System (2DMTS) 20

1.11.1 Introduction 20

1.11.2 Results and Discussion 23

1.11.3 2DMTS Preparation and Device Fabrication Process 38

1.11.4 Pressure, Stress, and Strain Analysis of the microstamper and PDMS 43

1.11.5 Post-transfer cleaning processes 45

1.11.6 Conclusion 46

1.12 Wet etching monolayer 47

1.13 References – Chapter 3 49

Advancing High-Performance Photonics Devices Using Two-Dimensional Material Integration 53

1.14 Post-passive tuning of silicon photonic circuits 53

1.14.1 Introduction 53

1.14.2 Methods 54

1.14.3 Results and discussion 56

1.14.4 Conclusion 64

1.14.5 References 65

1.15 Strain effect in 2D material for bandgap tuning for Optical Detection 67

1.15.1 Introduction 67

1.15.2 Results and discussion 69

1.15.3 Method 83

Device Fabrication 83

1.15.4 Conclusions 86

1.15.5 References 87

1.16 Exciton Strain Engineering in Monolayer TMDCs using Strain Engineering 90

1.16.1 Introduction 90

1.16.2 Results and Discussion 91

1.16.3 Method 95

1.16.4 Conclusion 97

1.16.5 References 97

1.17 Strain effect on WSe_2 bandgap Stretched on Nanostructures 98

1.17.1 Fabrication and Spectroscopic Analysis 98

1.17.2 References 102

1.18 2D Material Characterization and Heterojunction Based Photonic Devices 104

1.18.1 Electrical Characterization of 2D Materials post-2DMTS Integration 104
1.18.2 Building 2D material Heterostructures 106
1.18.3 References 109
1.19 Self-Driven Indium Selenide Heterojunction based Photonic Devices 111
1.19.1 Introduction 111
1.19.2 Results and Discussion 114
1.19.3 Conclusion 123
1.19.4 Methods 124
1.19.5 References 129
TCO Integrated High-Speed Electro-Optical Modulator 136
1.20 Introduction 136
1.21 Loss-induced index mismatch for coupling-based modulation 138
1.22 Results and Discussion 140
1.23 Conclusion 146
1.24 Method 147
1.25 References 150
Hybrid Material Integration for Mid-Infrared Photonic Devices 151
1.26 Introduction 151
1.27 Results and Discussion 154
1.28 Method 157
1.29 Conclusion 158
1.30 References 159
Conclusion and Outlook 161

List of Figures

Figure 1.1. 3

Figure 1.2 6

Figure 3.1. 25

Figure 3.2 29

Figure 3.3 36

Figure 3.4 40

Figure 3.5. 42

Figure 3.6 44

Figure 3.7 46

Figure 3.8 48

Figure 4.1 58

Figure 4.2 60

Figure 4.3 63

Figure 4.4 71

Figure 4.5. 73

Figure 4.6. 74

Figure 4.7 76

Figure 4.8. 77

Figure 4.9. 78

Figure 4.10. 79

Figure 4.11 80

Figure 4.12. 81

Figure 4.13 83

Figure 4.14 85

Figure 4.15 92

Figure 4.16 93

Figure 4.17. 100

Figure 4.18. 105

Figure 4.19 108

Figure 4.20 115

Figure 4.21 117

Figure 4.22 119

Figure 4.23. 121

Figure 4.24. 122

Figure 4.2 ……..……...124

Figure 4.26 125

Figure 4.27 127

Figure 4.28 128

Figure 5.1 141

Figure 5.2 143

Figure 5.3 145

Figure 5.4 146

Figure 5.5 149

Figure 5.6 150

Figure 6.1 155

Figure 6.2 156

Figure 6.3 157

Figure 7.1 162

Figure 7.2 163

List of Tables

Table 4.6.1……123

Introduction

1.1 Background, Motivation & Problem Statements

Photonic integrated circuits (PICs) are revolutionizing the field of communication networks and information processing by enabling the integration of multiple optical components onto a single chip. However, the development of PICs faces several challenges. One major challenge is the efficient coupling of light between different components, such as lasers, modulators, and detectors, due to the inherent weak interaction of light and matter. This results in limitations in size, speed, and power efficiency. To address these challenges, researchers are exploring various solutions. These include the development of high-efficiency light sources, low-loss waveguides, and advanced materials with enhanced light-matter interaction. Additionally, innovative design strategies and fabrication techniques are being investigated to optimize the performance and integration density of PICs. By overcoming these challenges and implementing effective solutions, PICs have the potential to revolutionize communication systems and enable new applications in areas such as data centers, telecommunication networks, and quantum computing.

Designing innovative materials to improve the quality of life is exciting, but it is also difficult in practice. A general solution for integrating the best of diverse constituents into one ultimate substance remains unresolved. Composite materials and III-V heterostructures have transformed many parts of our existence, setting the groundwork for the process of designing material characteristics. However, it is still difficult to mix and match crystalline

materials with their distinct features to build heterostructures with the controlled tuning of attributes, functions, and qualities. The material choice complexity is higher in the field of photonics as compared to electronics. Photonics, being an emerging field, is forecasted to surpass electronic thresholds paving the way for rapid progress in technology and sciences as seen in the photonics Moore's Law projections in Fig. 1.1.1. Photonics is the study of the creation, manipulation, and detection of light. The natural interaction between a photon (or light) and an atom (matter) is exceedingly weak and needs further engineering to enhance it. As a result, an interface that provides a strong light-matter interaction must be designed [1]. These interactions affect the materials' linear and nonlinear optical characteristics [2]. It is critical to improve light-matter interaction to produce passive and active tunable devices that can broaden the possibilities of new applications and boost development in present photonic platforms.

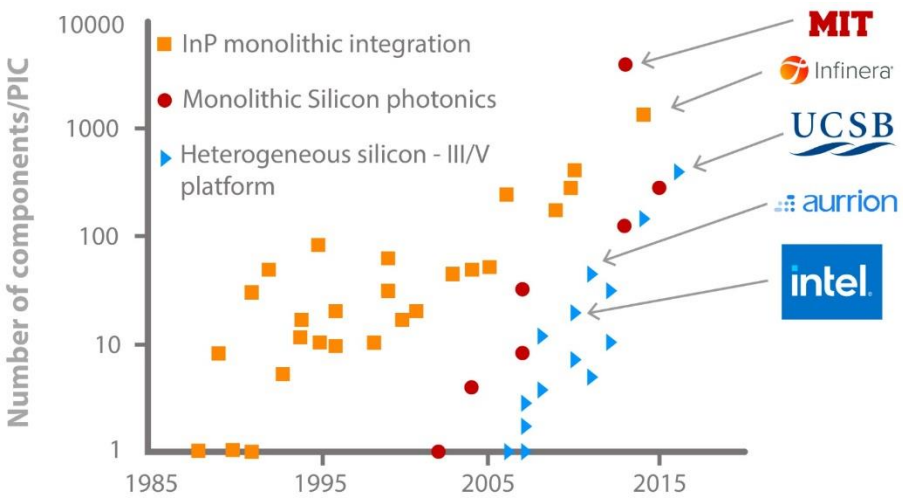

Figure 0.1 Photonic Moore's Law [3] shows the progress in the density of photonic integrated circuit (PIC) components on a chip over the period. The projection clearly shows that the future development of this field will surpass the limits of electronic circuits.

Photonic integrated circuits (PIC) have recently been investigated for neural network interconnection functions that require on-chip condensed solutions. As the demand for massive data processing, transmission, and storage grows, optimizing the energy usage of current systems is becoming increasingly difficult. Inter-chip and on-chip photonic interconnects, photonic analog-digital conversion, communications, and sensing all make use of integrated electro-optic (EO) modulators [4]. Modulators' general performance characteristics include high-speed, high-energy efficiency [5], high extinction ratio, low insertion loss, and a small footprint. Integrated plasmonic modulators enhance light-matter interaction, paving the way for high-bandwidth and small-footprint devices. The plasmonic mode has a high insertion loss, limiting signal propagation distance and operating energy

[6]. The low carrier-induced plasma dispersion and bandgap of silicon (Si) result in poor index tuning. On the other hand, a monolithically integrated EO component with inadequate Si EO sensitivity will have a large footprint. Among the transparent conductive oxides (TCO) that are most frequently used are indium tin oxide (ITO), tin oxide (SnO_2), zinc oxide (ZnO), and indium oxide (ITO) (In_2O_3). A greater comprehension of the conductivity processes is important for continued research, though, and new TCO materials that provide a significant improvement in conductivity and durability are still often needed. ITO's higher carrier concentration, which enables more precise control of the dispersion behavior, is what makes it preferable to Si for PIC modulation. The presence of the epsilon near zero (ENZ) region and the reduced permittivity of ITO makes it feasible for electrical bias to significantly affect effective index modulation. The Si photonic technology can be integrated at the foundry level thanks to ITO's CMOS compatibility.

Efficient light-matter interaction (LMI) is a fundamental requirement for achieving effective optical modulation in photonic integrated circuits (PICs). This interaction is crucial for achieving strong modulation, which in turn relies on the active materials exhibiting adequate interaction with light. There are two main types of electro-optic (EO) modulators: electro-optic modulators (EOMs) and electro-absorptive modulators (EAMs). EOMs operate by changing the real part (n) of the modal refractive index, resulting in phase-shifting-based interferometer-like devices. On the other hand, EAMs modulate the imaginary part (k) of the modal refractive index. In both cases, the complex index of

refraction is electrically altered within the active material, thereby modifying the propagation constant of the effective mode in the waveguide. The design and implementation of electrically driven modulators involve two main categories: current-driven modulators and voltage-driven modulators. Current-driven modulators achieve index changes by manipulating carriers in the active region, controlling optical transitions and oscillator strength. In contrast, voltage-driven EO modulators operate without current flow in or out of the active region, relying on energy level shifts and changes in oscillator strength induced by the electric field (e.g., Stark effect). Notable examples of voltage-driven EO modulators include lithium niobate ($LiNbO_3$) modulators based on the Pockels effect and III-V semiconductor-based quantum-confined Stark effect modulators. While the performance characteristics of both types are similar, voltage-driven modulators have limitations to prevent electrical breakdown in the active device region. Over the past years, there has been significant progress in miniaturized modulators, primarily focused on current-driven designs, which continue to be the subject of ongoing research and development efforts in the field of photonic integrated circuits.

After the first isolation of a very thin atomic layer of graphene, two-dimensional (2D) materials became heavily involved in research [7]. 2D materials such as graphene and other materials have a high potential for integration with various optoelectronic, quantum, and electrical devices. Exploring the characteristics and unique properties of these materials allows for the development of various applications based on electronics, strainoptronics,

valleytronics, catalysis, and biosensing. 2D materials can be used as single atomic layers, a few layers, or in bulk. Materials can be elemental, such as graphene and phosphorous, or mixed layered, such as transition metal dichalcogenides (TMDCs), van der Waals heterostructures, and Mxenes [5]. All these materials have distinct properties such as high carrier mobilities, superconductivity, mechanical flexibility, thermal conductivity, and, most importantly, high optical absorption, as well as changes in optical index and loss. This opens a wide range of applications for optoelectronic devices as seen in Fig. 1.1.2.

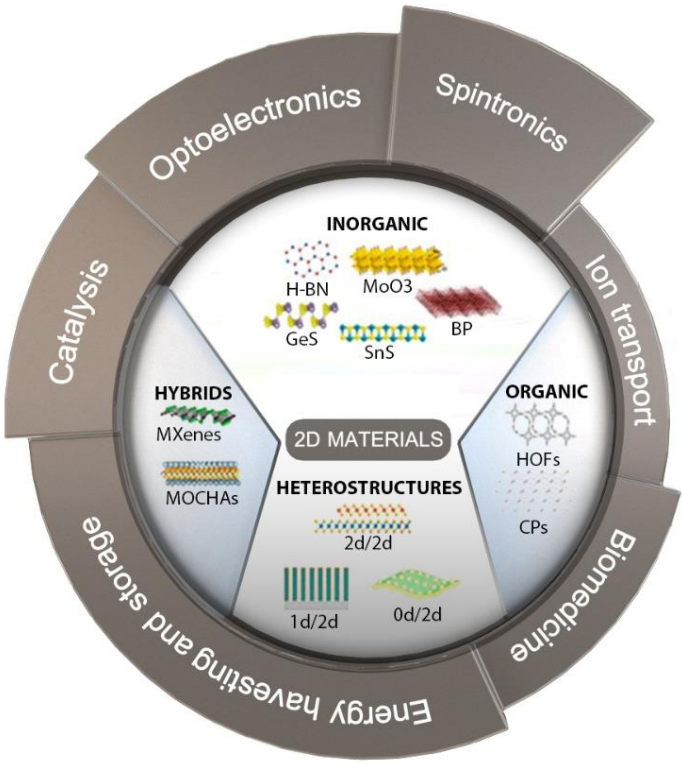

Figure 0.2 Diversity of selected 2D materials and their applications presented in this chart by [5]

In my dissertation, I propose to study and demonstrate the material characterization, hybrid material integration, and techniques to enhance light-matter interactions of 2D materials and ITO for photonic devices like photodetectors and modulators. Based on the

material selection, photonic platform, properties to be studied, and potential applications, I have developed the following ideas and have experimentally implemented them as chapters for my research progress:

1.2 Dissertation Outline

The dissertation is structured as follows:

Chapter 1. Introduction: Here I begin the discussion with a high-level overview of the background and objectives of this work which will be discussed throughout this dissertation.

Chapter 2. Material Properties for Photonics: Here I discuss active material, optical mode, and cavity dependence of on-chip electro-optic modulators with key parameters such as Kramers-Kronig relations, electrical tunability, scaling, confinement factors, etc. Different novel and emerging active materials have been chosen for this analytical and numerical study to aid crucial insights and understandings relevant to subsequent chapters.

Chapter 3. Novel Material Integration Metrology and Methodologies Development: Here, I demonstrate material integration procedures developed, modified, and customized for developing electro-optic, optoelectronics, and electrical applications. A novel automated two-dimensional material deterministic transfer system (2DMTS) developed shows its high accuracy, reliability, repeatability, and non-contaminating transfer features.

Chapter 4. Advancing High-Performance Photonics Devices Using Two-Dimensional Material Integration: A wide range of opportunities for investigating various features displayed by these materials emerge when many 2D crystals are stacked vertically. More combinations are possible with such heterostructures than with any other conventional material stacking growth procedure since they are kept together by vdW forces. I will present various devices for photodetection, sensing, and modulation applications using 2D material integrated with a photonic platform. Further, engineering material properties for high-speed applications, self-driven sensors, heterostructure designs, and strain engineering will be discussed in subsequent sub-chapters.

Chapter 5. TCO Integrated High-Speed Electro-Optical Modulator: Here, I demonstrate a high-speed electro-optical modulator using a silicon directional coupler and ITO as a hybrid dielectric medium. The device utilizes loss-induced transparency in a non-Hermitian coupler, where the increasing loss in one arm enhances transmission through the other arm, breaking the parity-time symmetry.

Chapter 6. Hybrid Material Integration for Mid-Infrared Photonic Devices: This project enables explorations of several scientific and engineering projects on both material, device, and submodule levels. For example, emerging MID-IR materials such as those belonging to the class of MXenes, once packaged into dedicated device-form-factor (e.g., contacts, waveguide overlap, etc), enable high-speed (10's GHz) Mid IR photodetectors and modulators. Another field that will be accelerated is non-mechanical beam steering in

MID-IR for LIDAR applications with relevance for UAVs. FSO communication in mid-IR wavelength (2-10μm) leverages some unique advantages as follows: a) specific wavelength range allows long-distance light transmission through the atmosphere with minimal loss; b) mid-infrared (mid-IR) experiences less Rayleigh scattering and less interference from ambient solar radiation compared to shorter wavelengths; c) mid-IR exhibits the peak of the blackbody radiation curve for room-temperature objects which is essential for thermal imaging systems; d) maintains low transmission loss in certain optical fibers. Indeed, MID-IR is a critical frequency for defense and national-security applications with a high-relevance for civil applications as well.

Chapter 7. Conclusion and Outlook: Finally, a summary of the works discussed in this dissertation and an outlook for possible future directions including different device scheme options and emerging applications is presented.

1.3 References - Chapter 1

[1] Y. Xiao *et al*, "Strongly enhanced light-matter interaction in a hybrid photonic-plasmonic resonator," *Physical Review. A, Atomic, Molecular, and Optical Physics*, vol. 85, *(3)*, 2012. Available: https://search.proquest.com/docview/2086389479. DOI: 10.1103/PhysRevA.85.031805.

[2] C. Lienau, M. A. Noginov and M. Lon ar, "Light-matter interactions at the nanoscale," *Jopt*, vol. 16, *(11)*, pp. 110201, 2014. Available:

https://iopscience.iop.org/article/10.1088/2040-8978/16/11/110201. DOI: 10.1088/2040-8978/16/11/110201.

[3] J. E. Bowers, "Evolution of photonic integrated circuits," in Jun 2017, pp. 1-2.

[4] A. K. Geim and K. S. Novoselov, "The rise of graphene," *Nature Materials*, vol. 6, *(3)*, pp. 183-191, 2007. Available: http://dx.doi.org/10.1038/nmat1849. DOI: 10.1038/nmat1849.

[5] H. R. Gutiérrez, "Two-Dimensional Layered Materials Offering Expanded Applications in Flatland," *ACS Applied Nano Materials*, vol. 3, *(7)*, pp. 6134-6139, 2020. Available: http://dx.doi.org/10.1021/acsanm.0c01763. DOI: 10.1021/acsanm.0c01763.

[6] M. H. Tahersima *et al*, "Coupling-enhanced dual ITO layer electro-absorption modulator in silicon photonics," *Nanophotonics*, vol. 8, *(9)*, pp. 1559-1566, 2019. Available: http://www.degruyter.com/doi/10.1515/nanoph-2019-0153. DOI: 10.1515/nanoph-2019-0153.

[7] V. J. Sorger *et al*, "Scaling vectors of attoJoule per bit modulators," *Jopt*, vol. 20, *(1)*, pp. 14012, 2018. Available: https://iopscience.iop.org/article/10.1088/2040-8986/aa9e11. DOI: 10.1088/2040-8986/aa9e11.

[8] J. B. Khurgin, "How to deal with the loss in plasmonics and metamaterials," *Nature Nanotechnology*, vol. 10, *(1)*, pp. 2-6, 2015. Available: https://www.ncbi.nlm.nih.gov/pubmed/25559961. DOI: 10.1038/nnano.2014.310.

Material Properties for Photonics

1.4 Introduction

In recent years, the field of two-dimensional (2D) materials has witnessed remarkable advancements, offering a vast array of possibilities for scientific exploration and technological breakthroughs. These materials, consisting of atomically thin layers, exhibit extraordinary properties that are distinct from their bulk counterparts, paving the way for novel applications in a wide range of disciplines. Among the various types of 2D materials, Transition Metal Dichalcogenides (TMDCs), MXenes, and Topological Insulators (TIs) have emerged as particularly intriguing materials with unique characteristics and immense potential for transformative advancements.

1.5 Transistion Di Metal Chalcogenides (TMDCs)

TMDCs, such as MoS_2, WS_2, $MoTe_2$, Graphene, and WSe_2, have garnered significant attention due to their fascinating electronic and optical properties. Unlike conventional semiconductors, TMDCs possess a direct bandgap in their monolayer form, enabling efficient light absorption and emission. This property makes them highly promising for optoelectronic devices such as photodetectors, light-emitting diodes (LEDs), and solar cells. Additionally, TMDCs exhibit strong spin-orbit coupling and valley-dependent properties, making them excellent candidates for valleytronics and strain-optronics a field focused on

manipulating information at the valley degree of freedom and bandgap engineering using mechanical strain on material respectively [1]-[5].

1.6 MXene

MXenes, another class of 2D materials, are derived from layered transition metal carbides, nitrides, or carbonitrides, known as MAX phases. By selectively etching the A-layer of MAX phases, MXenes with unique properties can be obtained. These materials possess excellent electrical conductivity, mechanical flexibility, and high surface area, making them highly desirable for energy storage applications such as batteries and supercapacitors. MXenes also show promise in catalysis, sensing, and electromagnetic interference shielding due to their tunable surface chemistry and superior conductivity. Such materials also form the future for extended applications in mid-infrared regimes [6]-[10].

1.7 Topological Insulator

Topological Insulators represent a fascinating class of materials that exhibit conducting surface states while maintaining an insulating bulk. These materials rely on the concept of topological protection, where electron states are protected from scattering by time-reversal symmetry. The presence of spin-polarized surface states in TIs offers significant potential for spintronics and quantum computing applications. Furthermore, the robustness of these surface states against impurities and disorder makes TIs attractive for low-power electronic

devices with reduced heat dissipation, presenting opportunities for the development of next-generation electronics [11]-[14].

The exploration and understanding of these 2D materials, including TMDCs, MXenes, and Topological Insulators, have sparked intense research efforts worldwide. Scientists are actively investigating their fundamental properties, fabricating devices, and exploring their potential applications in a diverse range of fields, including electronics, photonics, energy storage, and quantum technologies. With their unique properties, exceptional versatility, and ability to manipulate and engineer their properties, these 2D materials hold immense promise for revolutionizing the next generation of electronic and optoelectronic devices, offering unprecedented performance and functionality. As researchers delve deeper into the intricacies of these materials and harness their potential, new horizons for scientific discovery and technological innovation are expected to emerge, driving advancements that will shape the future of various industries.

1.8 Transparent Conductive Oxide (TCO)

Transparent Conductive Oxide (TCO) materials have revolutionized the fields of electronics and photonics by enabling the development of various optoelectronic devices and applications. These materials exhibit a unique combination of properties, including high optical transparency and electrical conductivity, making them ideal for applications that require the simultaneous transmission of light and conduction of electricity. Among

the wide range of TCO materials, Indium Tin Oxide (ITO) has emerged as one of the most extensively studied and widely used materials due to its exceptional transparency, conductivity, and compatibility with fabrication processes.

Indium Tin Oxide (ITO) is a ternary compound composed of indium, tin, and oxygen atoms. It possesses excellent electrical conductivity while maintaining high optical transparency in the visible range, making it a popular choice for applications such as transparent electrodes, touchscreens, organic light-emitting diodes (OLEDs), photovoltaics, smart windows, and other optoelectronic devices. The unique properties of ITO arise from its crystal structure, where the indium and tin atoms form a solid solution within an oxygen matrix. This composition allows for efficient charge transport while still allowing light to pass through the material.

The use of ITO in various electronic and photonic devices has significantly advanced the fields of display technology, solar energy conversion, and sensing applications. However, despite its widespread use, there are certain challenges associated with ITO. One of the primary concerns is the scarcity and high cost of indium, which has led to research efforts focused on finding alternative TCO materials with comparable or superior properties to ITO. Additionally, there are issues related to the brittleness and mechanical stability of ITO films, especially when deposited on flexible substrates.

In recent years, extensive research has been dedicated to the development of alternative TCO materials, including transparent conductive oxides based on zinc oxide,

aluminum-doped zinc oxide, and various other metal oxides. These materials aim to address the limitations of ITO and offer enhanced performance, cost-effectiveness, and mechanical flexibility.

In this context, this review will primarily focus on Indium Tin Oxide (ITO) as a representative TCO material, highlighting its unique properties, fabrication methods, device applications, and ongoing research efforts to overcome its limitations. Additionally, we will discuss emerging alternative TCO materials and their potential for replacing or supplementing ITO in future electronic and photonic devices [15]-[19].

1.9 References - Chapter 2

[1] Anonymous "Two-dimensional atomic crystals | PNAS," Available: https://www.pnas.org/doi/10.1073/pnas.0502848102.

[2] K. F. Mak *et al*, "Atomically Thin ${\mathrm{MoS}}_{2}$: A New Direct-Gap Semiconductor," *Phys. Rev. Lett.,* vol. 105, *(13),* pp. 136805, 2010. Available: https://link.aps.org/doi/10.1103/PhysRevLett.105.136805. DOI: 10.1103/PhysRevLett.105.136805.

[3] B. Radisavljevic *et al*, "Single-layer MoS2 transistors," *Nature Nanotech,* vol. 6, *(3),* pp. 147-150, 2011. Available: https://www.nature.com/articles/nnano.2010.279. DOI: 10.1038/nnano.2010.279.

[4] A. Splendiani *et al*, "Emerging Photoluminescence in Monolayer MoS2," *Nano Lett.*, vol. 10, *(4)*, pp. 1271-1275, 2010. Available: https://doi.org/10.1021/nl903868w. DOI: 10.1021/nl903868w.

[5] Q. H. Wang *et al*, "Electronics and optoelectronics of two-dimensional transition metal dichalcogenides," *Nature Nanotech*, vol. 7, *(11)*, pp. 699-712, 2012. Available: https://www.nature.com/articles/nnano.2012.193. DOI: 10.1038/nnano.2012.193.

[6] M. Naguib *et al*, "25th Anniversary Article: MXenes: A New Family of Two-Dimensional Materials," *Advanced Materials (Weinheim)*, vol. 26, *(7)*, pp. 992-1005, 2014. Available: https://api.istex.fr/ark:/67375/WNG-NB4WZ7WT-S/fulltext.pdf. DOI: 10.1002/adma.201304138.

[7] M. Ghidiu *et al*, "Conductive two-dimensional titanium carbide 'clay' with high volumetric capacitance," *Nature*, vol. 516, *(7529)*, pp. 78-81, 2014. Available: https://www.nature.com/articles/nature13970. DOI: 10.1038/nature13970.

[8] W. Chen, V. S. Kamenetsky and A. Simonetti, "Evidence for the alkaline nature of parental carbonatite melts at Oka complex in Canada," *Nat Commun*, vol. 4, *(1)*, pp. 1-6, 2013. Available: https://www.nature.com/articles/ncomms3687. DOI: 10.1038/ncomms3687.

[9] Anonymous "Flexible and conductive MXene films and nanocomposites with high capacitance | PNAS," Available: https://www.pnas.org/doi/10.1073/pnas.1414215111.

[10] Y. Gogotsi and Q. Huang, "MXenes: Two-Dimensional Building Blocks for Future Materials and Devices," *ACS Nano,* vol. 15, *(4),* pp. 5775-5780, 2021. Available: https://doi.org/10.1021/acsnano.1c03161. DOI: 10.1021/acsnano.1c03161.

[11] M. Z. Hasan and C. L. Kane, "Colloquium: Topological insulators," *Rev. Mod. Phys.,* vol. 82, *(4),* pp. 3045-3067, 2010. Available: https://link.aps.org/doi/10.1103/RevModPhys.82.3045. DOI: 10.1103/RevModPhys.82.3045.

[12] D. Hsieh *et al,* "A tunable topological insulator in the spin helical Dirac transport regime," *Nature,* vol. 460, *(7259),* pp. 1101-1105, 2009. Available: https://www.nature.com/articles/nature08234. DOI: 10.1038/nature08234.

[13] S. Xu *et al,* "Observation of Fermi arc surface states in a topological metal," *Science (American Association for the Advancement of Science),* vol. 347, *(6219),* pp. 294-298, 2015. Available: https://www.jstor.org/stable/24745884. DOI: 10.1126/science.1256742.

[14] Anonymous "Topological Insulator Materials | Journal of the Physical Society of Japan," Available: https://journals.jps.jp/doi/abs/10.7566/JPSJ.82.102001.

[15] K. Ellmer, "Past achievements and future challenges in the development of optically transparent electrodes," *Nature Photon,* vol. 6, *(12),* pp. 809-817, 2012. Available: https://www.nature.com/articles/nphoton.2012.282. DOI: 10.1038/nphoton.2012.282.

[16] C. G. Granqvist, "Transparent conductors as solar energy materials: A panoramic review," *Solar Energy Materials and Solar Cells,* vol. 91, *(17),* pp. 1529-1598, 2007.

Available: https://dx.doi.org/10.1016/j.solmat.2007.04.031. DOI: 10.1016/j.solmat.2007.04.031.

[17] E. Fortunato *et al*, "Transparent Conducting Oxides for Photovoltaics," *MRS Bulletin,* vol. 32, *(3),* pp. 242-247, 2007. Available: https://dx.doi.org/10.1557/mrs2007.29. DOI: 10.1557/mrs2007.29.

[18] Y. Liu, Y. Li and H. Zeng, "ZnO-Based Transparent Conductive Thin Films: Doping, Performance, and Processing," *Journal of Nanomaterials,* vol. 2013, pp. 1-9, 2013. Available: https://www.airitilibrary.com/Publication/alDetailedMesh?DocID=P20161118002-201312-201612070014-201612070014-512-520-067. DOI: 10.1155/2013/196521.

[19] C. Patil *et al*, "1fJ/bit coupling-based ITO monolithic modulator in integrated photonics," in 2021-09, DOI: 10.23919/MOC52031.2021.9598008.

Novel Material Integration Metrology and Methodologies Development

1.10 Chip Substrate Preparation

The integration of 2D materials and transparent conductive oxide (TCO) materials on chips requires careful substrate preparation to enable successful material integration and optimal device performance. Before integration, the substrate undergoes specific pre-preparation steps tailored for 2D material and TCO integration.

For 2D material integration, the substrate is typically cleaned to remove any contaminants that may hinder the adhesion or quality of the integrated materials. This

involves a thorough cleaning process using techniques such as solvent cleaning, plasma cleaning, or wet chemical treatments. The goal is to achieve a clean substrate surface free from dust, oils, or residual chemicals that could affect the adhesion and properties of the 2D materials. Additionally, surface functionalization techniques may be employed to modify the substrate surface and enhance the adhesion and compatibility with the 2D materials.

In the case of TCO material integration, the substrate preparation focuses on achieving a suitable surface for optimal TCO deposition. This may involve cleaning the substrate to remove contaminants and applying surface treatments to enhance the substrate-TCO adhesion. For example, the substrate surface may undergo plasma treatment or be functionalized with self-assembled monolayers to improve the TCO film quality and electrical conductivity. Additionally, the deposition of a thin interfacial layer, such as a buffer layer, may be considered to promote adhesion and compatibility between the TCO material and the substrate.

Post-preparation steps are also important in ensuring the long-term stability and performance of the integrated materials. This may include annealing or curing processes to enhance the material properties and eliminate any residual stresses or defects. Additionally, surface passivation techniques may be employed to protect the integrated materials from environmental degradation or enhance their electrical performance.

By carefully preparing the substrate for 2D material and TCO integration, it is possible to achieve a high-quality interface, promote strong adhesion, and optimize the electrical and optical properties of the integrated materials. These substrate preparation techniques are crucial for the successful integration of 2D materials and TCO materials on chips, enabling the development of advanced electronic and optoelectronic devices with improved performance and functionality.

1.11 Highly Accurate, Reliable, and Non-Contaminating Two-Dimensional Material Transfer System (2DMTS)

1.11.1 Introduction

The micromechanical exfoliation method played a crucial role in the success of graphene research, enabling the production of high-quality samples and fueling interest in studying other 2D materials like transition metal dichalcogenides (TMDCs), MXenes, and 2D layered insulators [1]-[5]. However, the exfoliation process yields non-uniformly distributed crystal flakes of varying sizes and thicknesses, resulting in a low yield of useful atomically thin flakes. Optical identification methods have been implemented to locate and identify desirable flakes based on contrast differences in their images, allowing for accurate and non-contact techniques [6]. While this method is effective for studying individual flakes, it is not suitable for fabricating complex systems such as integrating 2D materials

into prefabricated devices or building van der Waals heterostructures by stacking different 2D material flakes [7], [8].

To address these challenges and enable the fabrication of more complex systems with enhanced reliability and functionality, various experimental setups and techniques have been developed. These include pick-and-place approaches[9], wedging methods[10], polyvinyl alcohol (PVA) methods [11], patterned stamping methods [12], viscoelastic stamping [13], patterned monolayer transfer [14], metal-assisted transfer [15], and the Evalcite method [16]. While each of these techniques improves the efficiency of 2D material transfer, they have limitations in terms of achieving a high yield of quality flakes, preventing contamination of the substrate, ensuring repeatability in device performance, and avoiding undesired residues on the flakes.

The properties of 2D materials are highly sensitive to the transfer and handling methods employed, which may involve temperature-assisted transfer, sacrificial polymer layers, litho-assisted patterned stamps, or wet chemical processes for substrate etching. Reactive target substrate surface structures, capillary forces, and temperature changes can introduce challenges such as cracking, strain, and oxidation of the 2D materials. Dry transfer methods have been explored to overcome wet-chemistry-related challenges but have not fully addressed the critical issues of spatial cross-contamination and the low yield of high-quality flakes.

In my work, I introduce a novel automated 2D material transfer system (2DMTS) that overcomes these challenges. The 2DMTS utilizes a viscoelastic polymer and a metal micro-transfer stamper to achieve selective transfer, eliminating contamination on the 2D material flakes, devices, and target substrate. My method significantly increases the yield and quality of transferred material flakes while enabling rapid and accurate transfer without the need for wet chemical etching or thermal processes. I have experimentally validated the capabilities and performance limitations of 2DMTS, demonstrating its reliability, robustness, and **high spatial accuracy (0.7μm)** without cross-contamination. Moreover, I leverage the rapid prototyping capabilities of 2DMTS to showcase its potential in fabricating novel devices. I demonstrate the fabrication of optoelectronic devices with device novelty, covering fields such as photonics, arrayed structural deposition of materials, heterostructure lattices, and electronic devices, including strainoptronics-based photodetectors in the upcoming chapters using my developed automated 2DMTS.

1.11.2 Results and Discussion

The 2D transfer system platform (2DMTS) described in this study consists of essential components, including a metallurgical microscope, three linear axis stages for the movement of the Polydimethylsiloxane (PDMS) holder, a micro-transfer stamper, and a target chip for precise alignment (Fig. 3.2.1a). To ensure an unobstructed field of view for the microscope, a small screw lock-based clamp needle holder is mounted on an angled arm XYZ axis stage, which is positioned on top of the microscope (Fig. 3.2.1a). The micro-stamper can be carefully lowered along the Z-axis to establish contact with the substrate and transfer the selected flake after alignment (Fig. 3.2.1b). Equipped with a standard 8-bit CMOS camera, the microscope facilitates system alignment and measurement of flake size and area before the transfer, calibrated for the specific objective lens. This enables higher selectivity of 2D material flakes in terms of size and shape, tailored to the requirements of the application. The camera software utilizes a crosshair for aligning the position of the flake, micro-stamper, and target using the respective stages.

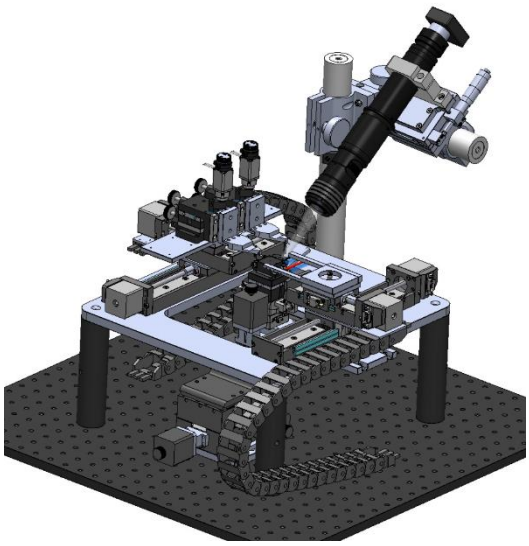

The use of soft PDMS aids in transferring the material onto different structures by wrapping around the profile, ensuring improved contact with the target without causing damage. Thin PDMS sheets (17mil) obtained from Gel Pak are cut into small strips (1.5cm x 3cm) and mounted on a PDMS cartridge, which is a microscope glass slide-based PDMS holder (referred to as the PDMS cartridge). The PDMS cartridge is held by clamp mount metal clips, suspending the PDMS in the air and mounted on an XYZ axis stage (Fig. 3.2.1c). The clamp mount clips facilitate easy loading and unloading of the PDMS cartridge, ensuring quick release without disturbing the alignment of other components when changing the 2D material source banks. This design allows for the realization of multiple PDMS strips with different 2D material source banks, eliminating the need to load and unload new PDMS films for different materials when building heterostructures.

After exfoliation from a crystal, the density of flakes on the Nitto tape is higher, leading to the formation of clusters of un-isolated flakes. When transferring these flakes onto a PDMS film, contacting the entire area of the PDMS with the tape results in the transfer of clusters of 2D material flakes onto the PDMS. The lower number of isolated flakes on the PDMS leads to fewer individual flake transfers from the 2D source bank cartridge. Therefore, it is crucial to transfer more isolated flakes onto the PDMS, which are loosely adhered to the tape, to facilitate ease of transfer and increase the yield. A detailed description of the modified exfoliation method of 2D material on PDMS film strips is provided in the method section below. The 2DMTS exfoliation graphical flowchart (Fig.

3.2.1d) illustrates how the modified method effectively avoids or significantly reduces the high density of flakes and overlapping clusters formed on the exfoliation tape. Before the transfer of 2D material, the chip or target substrate undergoes a cleaning process involving rinsing with acetone and isopropyl alcohol (IPA), followed by nitrogen drying. The cleaned substrate is then placed on an XY-θ stage, where rotation assists in loading and unloading the substrate for the transfer of 2D material.

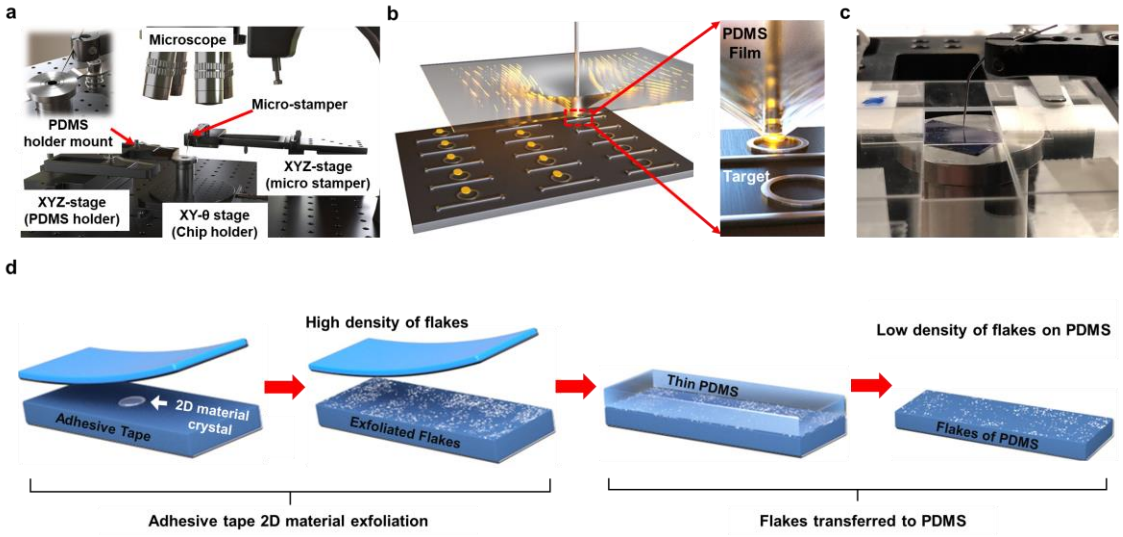

Figure 0.1 Robust, precise, and reliable 2DMTS. (a) The simplified 2D transfer system platform schematic includes the microscope, linear stages for alignment movement of the PDMS holder, micro-stamper, and target substrate, PDMS holder mount clips, and, a close view of the micro-stamper mounted on the setup. (b) Schematic of the PDMS, micro-stamper, and target chip position under alignment highlighting the close view of stretched PDMS when micro-stamper is approaching the targeted structure on the chip. Inset: showing the 2D material flake precisely positioned under the tip while the other flakes on the PDMS remain on the non-contact regions of

the PDMS on the holder. The magnified view shows the small area of PDMS (largest reported here, ~400 mm x 200mm) under the stamper with the flake underneath touching the target. (c) Side-angled image of the PDMS holder mounted on the stage with a PDMS strip mounted on it. The PDMS film is positioned over the target substrate and the micro-stamper is then adjusted on top of the selected flake as seen in the image. (d) The modified transfer process of 2D materials on PDMS using the adhesive tape exfoliation method helps to reduce the density of overlapping flakes and provides isolated flakes on PDMS for precisely locating flakes under the microscope. This allows selective transfer of the desired flake without cross-contamination on the chip.

The flake transfer yield is about 95.0% (Fig. 3.2.2), higher than any other state-of-the-art transfer system so far reported, as the entire surface area of the flake contacts with the target forms better adhesion to the target area. The failure in transferring the flake can be caused mainly because of the rough surface of the flake due to improper exfoliation, thus reducing the vdW adhesion strength with the target. A flake larger than the micro-stamper tip size reduces the transfer probability and is prone to break the flakes causing defects. But our different size micro-stamper range ensures flake-stamper size match. The contact area also defines the area of isolation (discussed in (Fig. 3.2.3)) required for each flake on PDMS to avoid multiple flakes being transferred, here solved by using a modified exfoliation process as seen in Fig. 3.2.1d to reduce the density of flakes on the PDMS film and discussed further.

The 2DMTS setup transfer accuracy and precision are determined by experimental statistical analysis of the system. This analysis is based on independent experimental transfers of 80 flakes from different 2D materials (graphene, MoS_2, hBN, and WSe_2) for each stamper size by two different users. Thus, the dependency on a user experience, as observed in other transfer methods, is reduced by analyzing data generated by these two users who helped in the independent transfer of materials for producing data. The flakes were transferred on a patterned grid of gold boxes for determining the position of the transferred flake in isolation. The distances of flakes transferred were measured from the center of the crosshair to the center of the flake using the calibrated camera software. The long working distance objective lenses can be switched to different magnifications for; 10x coarse (target search), 20x fine (flake search), and 40x finest (flake transfer) alignment based on the target size. The exfoliated flake sizes range between 1 μm – ~150 μm using Nitto tape. We have built different elliptical tip-sized micro-stampers herein termed stamper#1 (425μmx200μm), stamper#2 (300μmx145μm), and stamper#3 (185μmx130μm) for transferring exfoliated flakes.

The flake position distribution after transfer for the three stamper sizes can be seen in Fig. 3.2.2a-c where the inset shows the respective micro-stamper schematic for the elliptical stamping shape. A systematic offset error is observed in all three distributions leading to poor accuracy and precision. This offset is produced due to additional optics added between the microscope objective and camera for better imaging and illumination,

in addition to the refraction of the image due to the presence of PDMS in between the sample and microscope objective. The size of the micro-stamper also contributes to the offset due to variations in the stretching of PDMS while transfer. The histogram for the independent transfer attempts for each micro-stamper size shows the small systematic offset, indicated by the peak position involved in the transfer location for varying micro-stamper sizes Fig. 3.2.2d. Based on the iterative transfer test the systematic offset error for each micro-stamper was calculated to be approximately ~12.6 μm, ~8.4 μm, ~5.8 μm for stamper #1, #2, and #3 respectively. Since the offset values for each stamper size remain constant, a constant shift is introduced to the software crosshair to account for this offset, thereby improving the accuracy and precision of the tool. The associated standard deviation distribution (Fig. 3.2.2e) illustrates the distribution of the transfer locations for each stamper, normalized to the systematic offset error. The distribution reveals approximately 11.6%, 10.2%, and 7% transfer position variation from the offset crosshair for the respective stampers within $\pm 1\sigma$ of standard deviation.

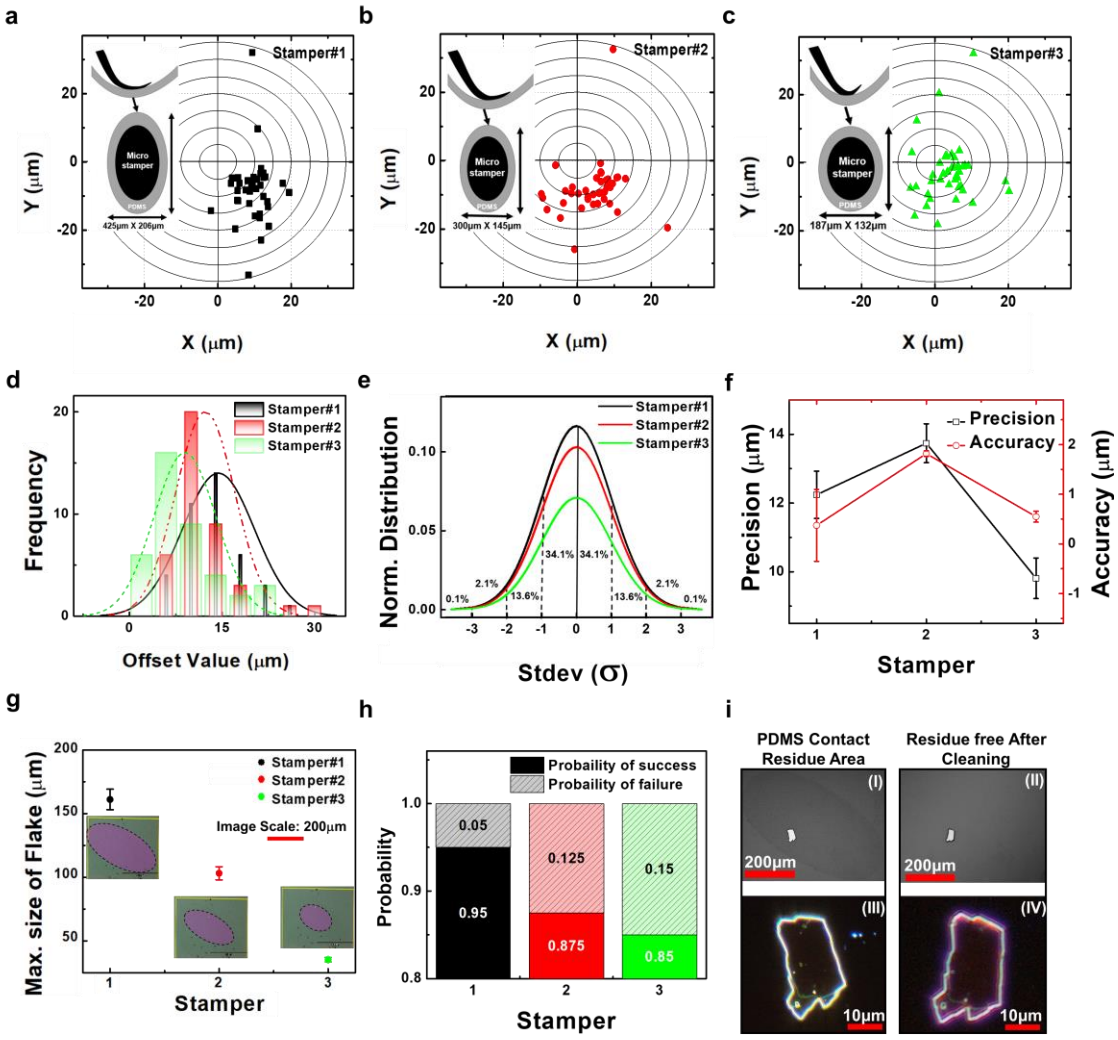

Figure 0.2 2D printer setup performance analysis for accuracy, precision, and reliability test. (a)-(c) Distribution of position of flakes transferred on SiO_2 substrate measured from the center of the target. The offset produced due to optics and the size of the micro stamper can be observed in the graph. The inset shows the schematic representation of the micro stamper size and shapes on top of the PDMS. (d) Histogram fitted with a Gaussian curve that illustrates the standard deviation of transferring process for each micro-stamper size. The graph also represents the offset in target location due to optics and stamper size (e) Standard deviation distribution of the flake transfer position on target measured considering the center of the flake to the software crosshair. Each band

has 1 standard deviation, and the labels indicate the approximate proportion of area (note: these add up to 99.8% of data, and not 100 percent of data because of rounding for presentation). (f) The accuracy and precision values with error bars are computed for each stamper showing high accuracy for small stamper sizes and reduced accuracy and precision for large stamper sizes. (g) Maximum size of flake that can be transferred with the three sizes of stamper. The inset microscope image represents the effective area of stamping for each stamper. The false-colored elliptical part highlights the stamping area where the scale bar is 200μm as the stamper shape is elongated in one direction as seen in Fig. 2 (a-c) inset (h) The probability distribution of transfer success and failure rate of the transfer system was calculated by gathering 40 data sets by transferring different flakes in a different location (i) Microscope image of transferred MoS_2 flake on oxide substrate with PDMS residue (I) and after cleaning process showing the residue-free area (II). The flake area after the transfer (III) and residue-free area after the cleaning process (IV) is confirmed by darkfield microscopy.

The accuracy of the tool is defined by the mean value of the position distribution from the offset crosshair/target center, while the precision is defined by the spatial distribution density around the mean value. The distributions in Fig. 3.2.2a-c demonstrate that the maximum spread of data is within the 10 μm range. Fig. 3.2.2f depicts the accuracy of each micro-stamper, with stamper#3 exhibiting the highest accuracy of 0.7 μm and precision within <10 μm. Such accuracy and precision are crucial for integrating 2D materials into

highly dense photonic or electronic devices on-chip and for nano-sensing applications. The smaller micro-stamper sizes offer higher accuracy and precision due to the smaller contact area and lower offset deviation from the target. Fig. 3.2.2g provides information on the maximum flake size that can be transferred and the effective contact area of the PDMS for the three micro-stamper sizes. This assists users in selecting the appropriate stamper size to achieve optimized transfer accuracy for desired flake sizes and targets. The inset images represent the effective contact area of the PDMS with the target substrate during each flake transfer, defining the area of flake isolation as well. The false color (purple) area enhances the image contrast of the PDMS stamping area under the microscope for better visualization.

To determine the yield of the transfer process achieved by the 2DMTS system, flakes of various sizes were randomly transferred to known locations on a SiO_2 substrate (Fig. 3.2.2h). This experiment aimed to test the reliability and repeatability of the system for multiple single-flake transfers in a single attempt. A successful transfer was defined as the transfer of a 2D material flake to the target on the substrate without cross-contamination of flakes or any deformation or cracking of the flake. A failure was noted if any of these conditions were not satisfied. The probability distribution of the success and failure rates of the transfer system was calculated using this dataset, as shown in Fig. 3.2.2h. The success rates were determined to be 95%, 87.5%, and 85% for each stamper, respectively. All 40 independent transfers were performed sequentially without any changes to the

PDMS film or setup alignment, except for searching different flakes on the PDMS and changing the target location. Therefore, the setup proved to be highly repeatable, reliable, precise, and accurate for a wide range of applications in science and technological advancements. The 2DMTS system exhibits a multitude of properties that have not been achieved by any other 2DMTS reported in the literature [9]-[12], [14], [17], [18].

After the transfer process, both the flake and the PDMS contact area are cleaned using acetone followed by isopropyl alcohol (IPA) rinsing to remove any PDMS residues (Fig. S3). It is important to handle samples where the material is transferred onto a structured profile with care during rinsing and drying, minimizing vibrations. Due to the thickness of the flakes, the vdW forces may not be strong on the sides of structures, as the flakes may not conformally cover the structures.

To ensure the successful transfer of flakes onto a substrate and improve their adhesion, certain critical measures need to be taken. One common challenge is the potential movement of transferred flakes due to mechanical vibrations. To address this, the sample is placed in a vacuum chamber for 20-30 minutes, which enhances the adhesion of the flakes to the substrate surface, preventing them from shifting. Additionally, various microscopy techniques can be employed to examine the results of the cleaning process and assess the quality of the transfer. Darkfield microscopy, optical filter-based microscopy, or secondary electron microscopy (SEM) are commonly used, depending on the desired

resolution for inspection. In Fig. 3.2.2i, for instance, a molybdenum disulfide (MoS_2) flake transferred onto a SiO_2 substrate is observed using a microscope. However, due to the small size of the particles, the contrast is limited. To address this, contrast correction techniques can be applied to enhance the observed contact area (Fig. 3.2.2i(I)). After a simple post-transfer cleaning process, any residues are completely removed, leaving a clean surface on the flake (Fig. 3.2.2i(II)). Verification of the cleanliness and preservation of the flake's quality can be done through darkfield microscope images, as shown before (Fig. 3.2.2i(III)) and after (Fig. 3.2.2i(IV)) the cleaning process. These steps ensure that the transferred flakes adhere well to the substrate, exhibit high quality, and minimize the risk of cross-contamination on the substrate's surface.

To ensure repeatability and reliability in the transfer process of multiple flakes onto a substrate, it is important to address potential challenges such as non-cross contamination, wrinkle formation, cracking of large flakes, and accidental transfer of nearby flakes. In Figure 3a-f, optical images demonstrate the transfer of different sizes and shapes of graphene flakes onto a SiO_2 substrate using a 2D printer. The images capture the flakes on the polydimethylsiloxane (PDMS) stamp, the flakes transferred onto the substrate, and the PDMS at the same location after the transfer process. The isolation of nearby flakes from the target flake during the transfer process can be observed, where the side flake remains on the PDMS after the transfer of the target flake (Fig. 3a, f). However, it is challenging to

avoid the transfer of small flakes within the range of a few microns due to the difficulty in isolating such small distances and preventing cross-contamination, as statistically verified in Figure 2g relative to the stamper size. The images also demonstrate that the wrinkling or folding of the material caused by the viscoelastic nature of PDMS does not reflect after transfer onto the substrate, likely due to slight stretching of the PDMS during stamping. This suggests that the 2D material flakes are not strongly adhered to the PDMS, thanks to the modified flake transfer technique discussed in Figure 1d, making it easier to transfer them onto structures. Lastly, if small wrinkles are present after the transfer, the sample can be placed in a high vacuum chamber to remove them. These observations and precautions contribute to maintaining the integrity of the transferred flakes and ensuring successful and reliable transfer processes.

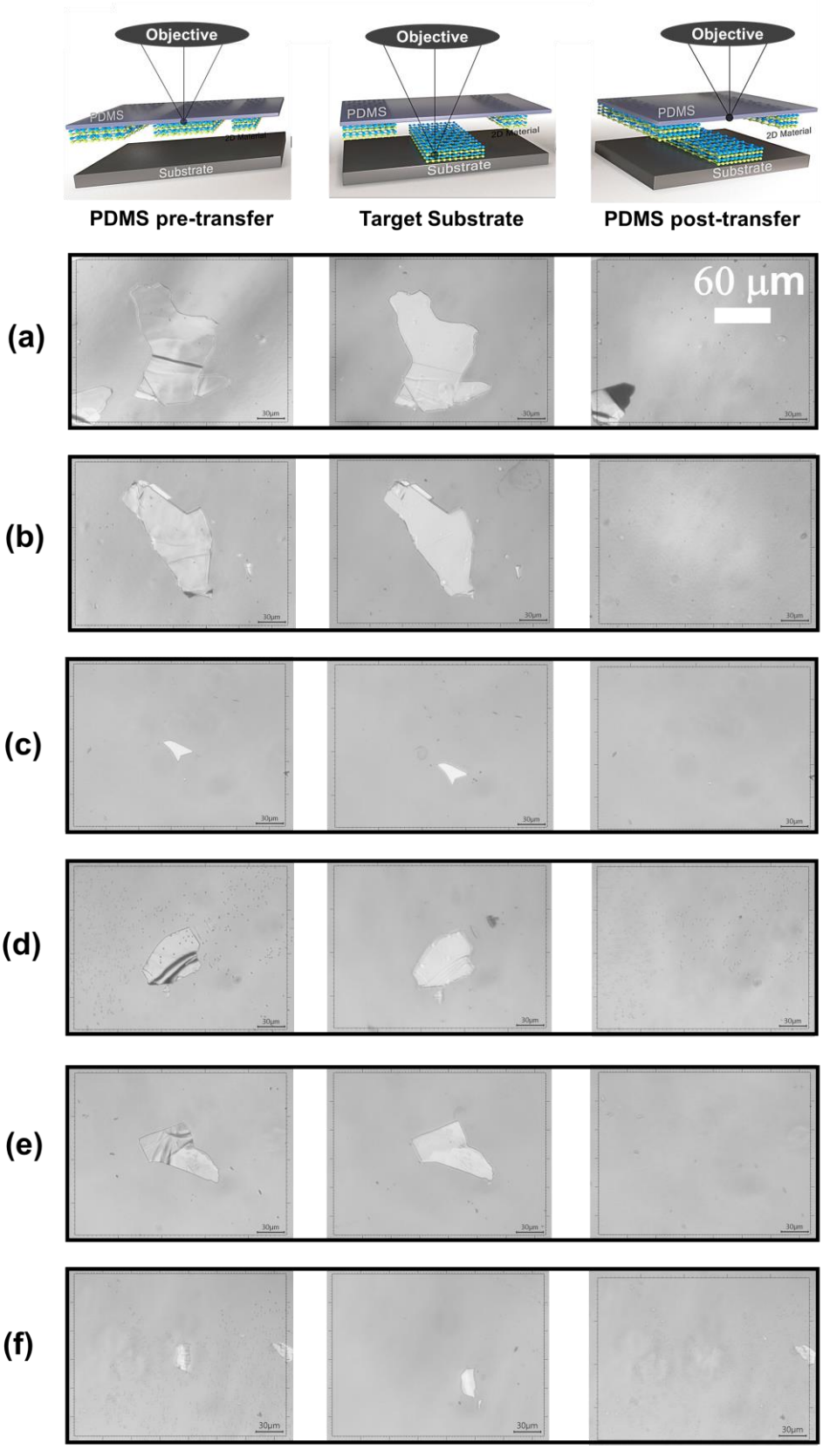
Objective
PDMS
2D Material
Substrate
PDMS pre-transfer
Target Substrate
PDMS post-transfer
60 μm
(a)
(b)
(c)
(d)
(e)
(f)

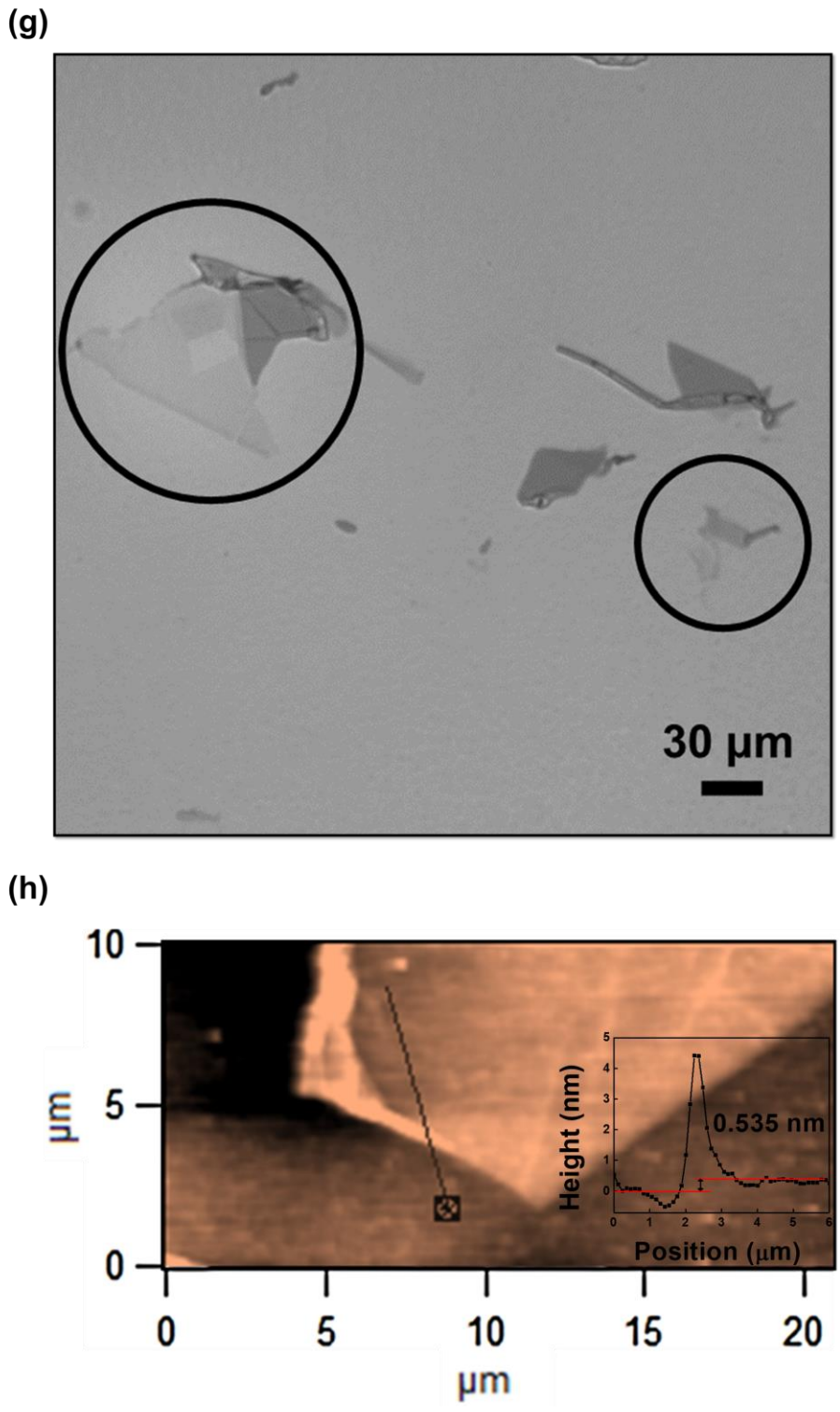

Figure 0.3 Transfer results from the 2D material transfer system. (a)-(f) Optical microscope images for 2D graphene flake on PDMS (before transfer), a substrate with flake after the transfer, and of

PDMS (after transfer) captured while using the 2D printer setup. The images verify no cracking, wrinkles, or folding of the flake after transfer on the substrate. (g) Optical microscope image of the exfoliated monolayer to a few layers of graphene flakes on PDMS. (h) Atomic force microscopy (AFM) mapping of monolayer graphene flake after transfer on SiO_2/Si substrate using 2DMTS and cleaning as shown in Fig. S3. The mapping clearly shows no residues of PDMS on the surface and the thickness of the material in the inset graph.

In order to establish the repeatability and reliability of the transfer process, it is important to understand and address potential issues such as cross-contamination, wrinkling or bubbling of the flake, cracking of large flakes, and accidental transfer of nearby flakes. Fig. 3.2.3a-f illustrates the transfer of graphene flakes of different sizes and shapes onto a SiO2 substrate using the 2DMTS system. The optical images captured during the process include the flake on the PDMS, the transferred flake on the substrate, and the PDMS at the same location after transfer. These images demonstrate the successful isolation of nearby flakes from the target flake during the transfer process. Flakes located on the side do not come into contact with the substrate and remain on the PDMS after the target flake is transferred. However, it is challenging to prevent the transfer of very small flakes within the range of a few microns, as statistically verified in Fig. 3.2.2g based on the stamper size. Additionally, the images reveal that wrinkling or folding of the material, caused by the viscoelastic nature of PDMS, is not apparent after transfer onto the substrate.

This can be attributed to slight stretching of the PDMS during stamping, indicating that the 2D material flakes are not strongly adhered to the PDMS surface. This modified flake transfer technique, as discussed in as seen in Fig. 3.2.1d, facilitates easy transfer onto structures. In cases where small wrinkles occur after the transfer, the sample can be placed in a high vacuum chamber to remove them. This step helps in achieving a smooth and uniform surface. Understanding and addressing these factors contribute to the reliability and repeatability of the transfer process, ensuring the successful transfer of flakes without cross-contamination and preserving the integrity of the transferred flakes on the substrate.

1.11.3 2DMTS Preparation and Device Fabrication Process

Micro-Stamper Fabrication:

The micro-stamper is created by modifying tungsten electrical probe needles. First, the needle is positioned at a 45-degree angle on a holder. Then, it is lowered perpendicularly and pressed against a metal plate, causing the tip of the needle to bend. The amount of force applied determines the size of the bent tip. The resulting curved tip provides a smooth characteristic to the micro-stamper, preventing it from piercing the PDMS sheet during the transfer process. The size of the stamping area is determined by measuring the PDMS contact area after the transfer.

Reusable PDMS Holder Preparation:

The PDMS holder is designed to accommodate multiple PDMS strips, allowing for different or identical materials to be placed on each strip. To prepare the PDMS holder, six thin glass slides (~1.2mm thick), Gel-Pak thin PDMS film (17 mils thick), and double-sided and single-sided adhesive tapes are required. The preparation process is illustrated in Fig. 3.2.4, steps 1-5.

Exfoliation Process:

The exfoliation process involves the use of a weak adhesive Nitto tape, as described in [1]. The process begins by placing a small piece of crystal from a bulk 2D material at one end of a Nitto tape strip, which should have a width equivalent to that of a PDMS strip. The tape is then repeatedly peeled back and forth, causing the flakes to spread on the tape. Subsequently, the tape, with the adhered flakes, is brought into contact with the target substrate to transfer the flakes. However, this traditional transfer technique often leads to decreased yield and cross-contamination due to residues and clustered flakes. To address this, the tape is gently pressed against the suspended PDMS cartridge, allowing loosely bonded flakes to naturally adhere to the PDMS through capillary force. This reduces clumping and promotes the transfer of isolated flakes while minimizing glue contamination. The entire exfoliation process is performed at room temperature. The detailed procedure can be seen in Fig. 3.2.4.

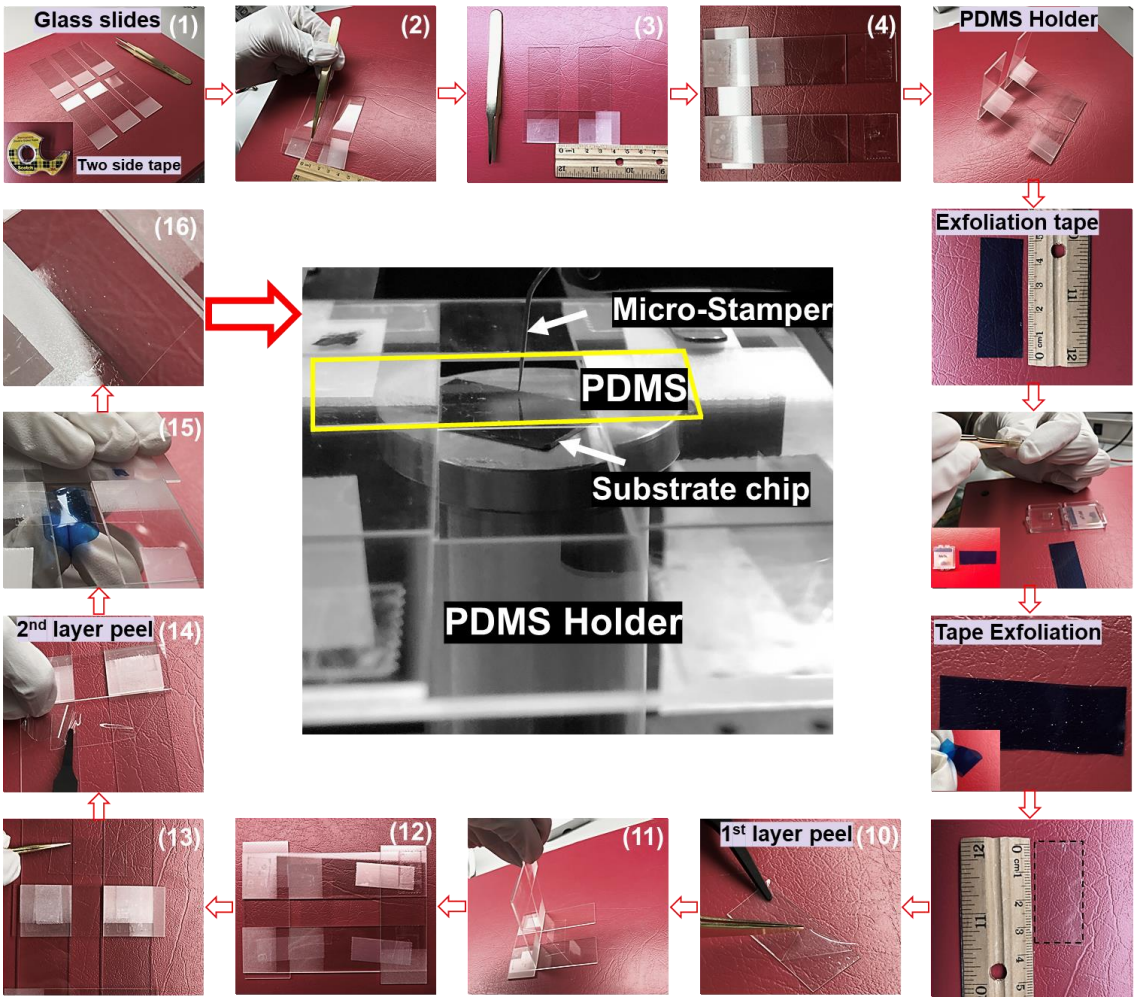

Figure 0.4 Step-by-step pictorial flowchart for PDMS holder preparation and modified exfoliation technique. The holder can be reused once prepared by replacing the PDMS film clamped in between the glass slide frame. The preparation of the holder requires thin glass slides (~1.2mm), Gel-Pak thin PDMS film (17 mils), double-sided and single-sided adhesive tapes, pair of tweezers, weak adhesion exfoliation tape, a ruler, and 2D material crystal. The figure in the center shows the placement of the holder on the stage for finding and positioning the 2D material flakes [13]

Transfer Process:

The transfer process using the 2DMTS (2D Material Transfer System) is straightforward and highly efficient (Fig. 3.2.5). The system is designed to be user-friendly, requiring minimal user experience and training. The transfer process can be summarized in three simple steps: (i) finding the flakes, (ii) positioning the flake and target area, and (iii) transferring the material. To find the desired flake, the PDMS can be moved in the XY direction, and the camera software's measurement feature can be utilized to select the desired size and shape. The microscope's focal adjustment allows for precise focusing on the micro-stamper, PDMS, and through the PDMS onto the target substrate after loading the PDMS holder onto the stage.

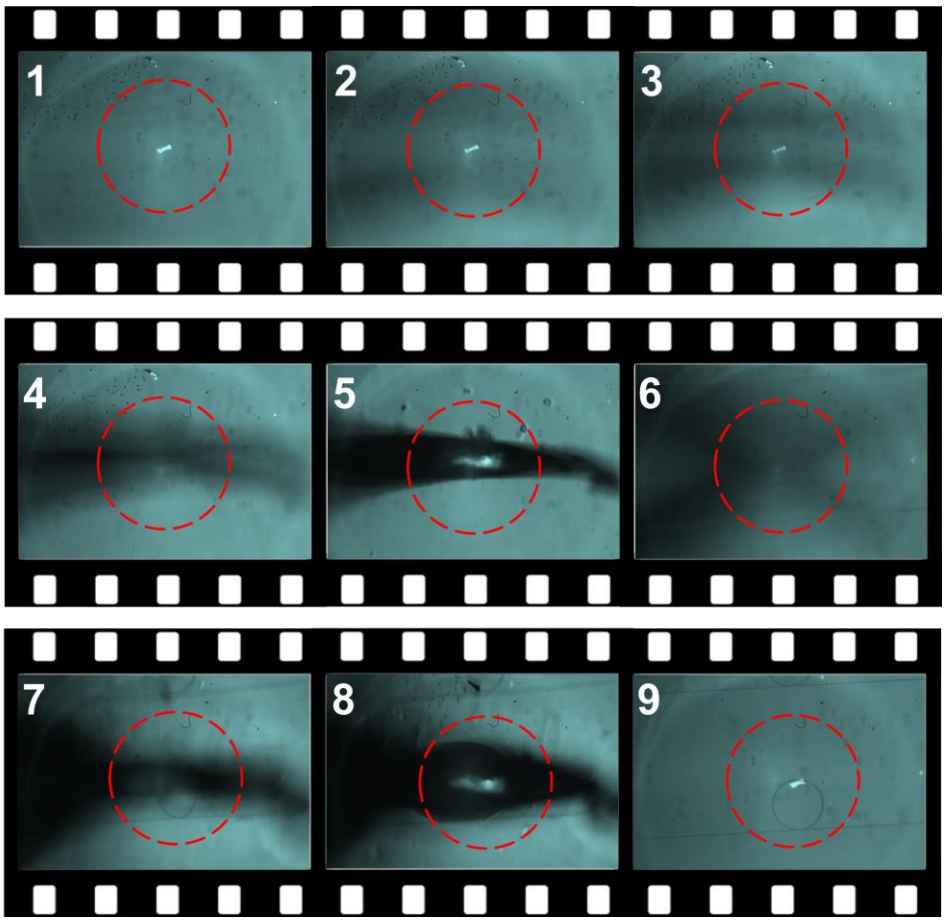

Figure 0.5 The real-time video frames were acquired during the transfer of WSe_2 flakes onto a silicon microring resonator (MRR) structure. The numbers on each frame denote the order in which the frames were captured during the transfer. Frames #1 - #4 show the micro stamper approaching the PDMS. The growing shadow on top of PDMS helps determine the closeness of the microstamper to the PDMS film. Frame #5 shows the micro stamper tip contacting the PDMS which indicatively can be observed by the sharpness of the shadow projected on PDMS. The focus of the microscope is shifted to the target at this point, where the stamper shadow is blurred (frame #6). As the stamper approaches the target for transfer the shadow tends to be sharper (frame #7). The PDMS contact with the target can be seen in frame #8 where the motion of the stamper is

stopped. Frame #9 shows the stamper reverting to its original location with the flake being transferred on the MRR.

Using the micro-manipulating stages, a software crosshair assists in aligning the 2D material flake, target area, and needle to achieve precise overlapping. Once aligned to the center of the crosshair (homing position), the XY position of the target and PDMS can be adjusted as necessary to locate the flake and fine-tune the target's position. When the micro-stamper is brought in contact with the PDMS, the live video provides clear indicators, allowing the operator to avoid excessive pressure on the material during transfer. After the PDMS contacts the substrate, the micro-stamper is carefully retracted to the homing position and the process can be repeated for other flakes on the PDMS and target locations on the substrate.

1.11.4 Pressure, Stress, and Strain Analysis of the microstamper and PDMS

During the transfer, the micro-stamper applies a stress of approximately 450kPa on the PDMS film, as simulated using ANSYS static structural analysis. The pressure exerted on the flake and substrate is experimentally measured to be around 13kPa, which falls within the elastic limit of the 2D material and PDMS materials. The safety aspect of the 2DMTS micro stamping technique in terms of applied pressure on the material during the stamping process is experimentally demonstrated and verified using Ansys static structural

simulation. A pressure sensor is placed under the substrate to measure the pressure exerted by the micro stamper on the substrate while transferring the 2D material flakes.

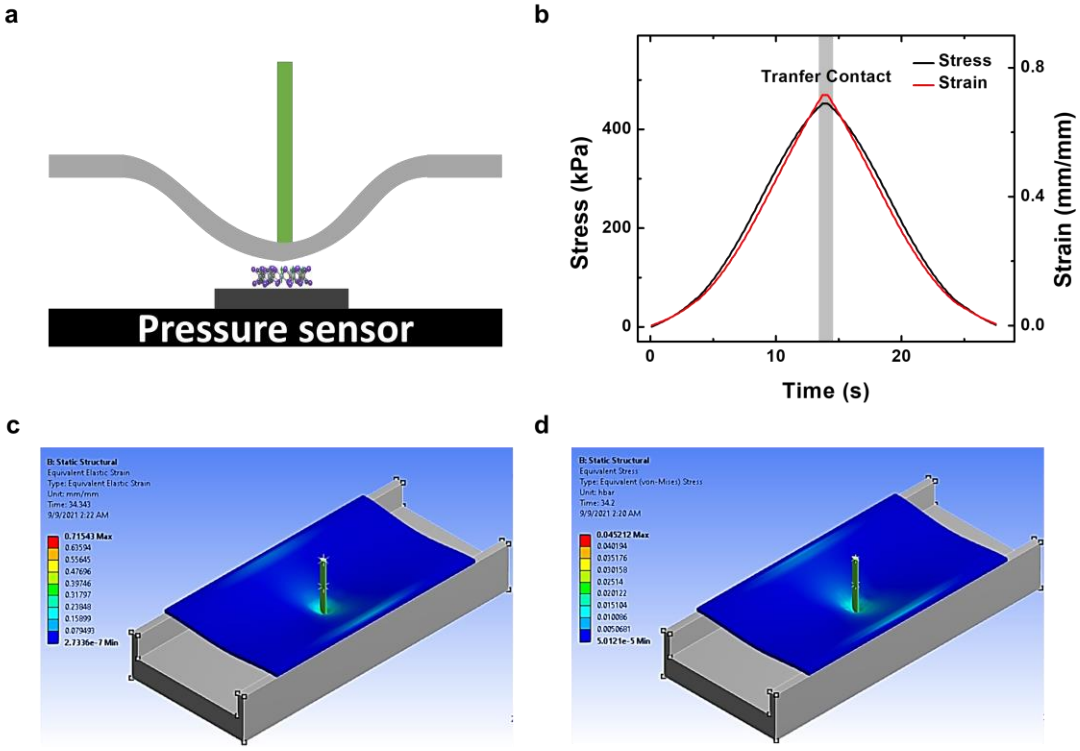

Figure 0.6 Robust, precise, and reliable 2DMTS. (a) Schematic view of pressure measurement exerted by the micro stamper on the substrate and material during the transfer process. (b) Stress and Strain induced in PDMS and on the substrate at contact. Ansys static structural 3D simulation results for (c) strain induced in PDMS and (d) stress gradient.

This value is further normalized to the area of contact to compute the closest value of pressure exerted on the 2D material. The transfer motion is precisely controlled by a piezo-electric motorized micromanipulator providing substantial control over the amount of

pressure required for a successful transfer. The experimental test result for the pressure exerted is about 13kPa (Fig. 3.2.5a). Further to understand the elastic deformation of PDMS we simulate the motion of the micro stamper along with PDMS stretching for confirming that the PDMS sheet is not damaged during the transfer process due to permanent dents or piercing as shown in Fig. 3.2.5b. The 3D simulation result for stress and strain are represented by Fig. 3.2.5c and Fig. 3.2.5d respectively. The scale for the minimum to maximum change for strain **(**Fig. 3.2.5c**)** is from 2.733E-7 mm/mm to 0.715 mm/mm and stress **(**Fig. 3.2.5d**)** is 501.2 hbar to 0.0452 hbar. These results show that the amount of stress and strain generated in PDMS are minimal and within the elastic limits of PDMS (MPa). Also, the pressure exerted on 2D material and substrate (~13kPa) is orders of magnitude less than the elastic limit of 2D materials (GPa). We also observe a smooth gradient of stress points around the edge of the micro stamper due to the thickness and elastic effect of the soft PDMS and rounding of the tip of the metal micro stamper [13].

1.11.5 Post-transfer cleaning processes

The samples after transfer should be kept in a vacuum environment as it helps the material to adhere to the substrate properly. The sample can be kept in acetone for 2-3 minutes and then in isopropyl alcohol for 2 mins to get rid of any organic and/or PDMS residues loosely scattered over flakes and substrate. It is important to carefully dry the

sample using nitrogen gas to avoid the strong force of the gas flow damaging the flakes. Fig. 3.2.7 shows the graphical representation of the simple cleaning process [13].

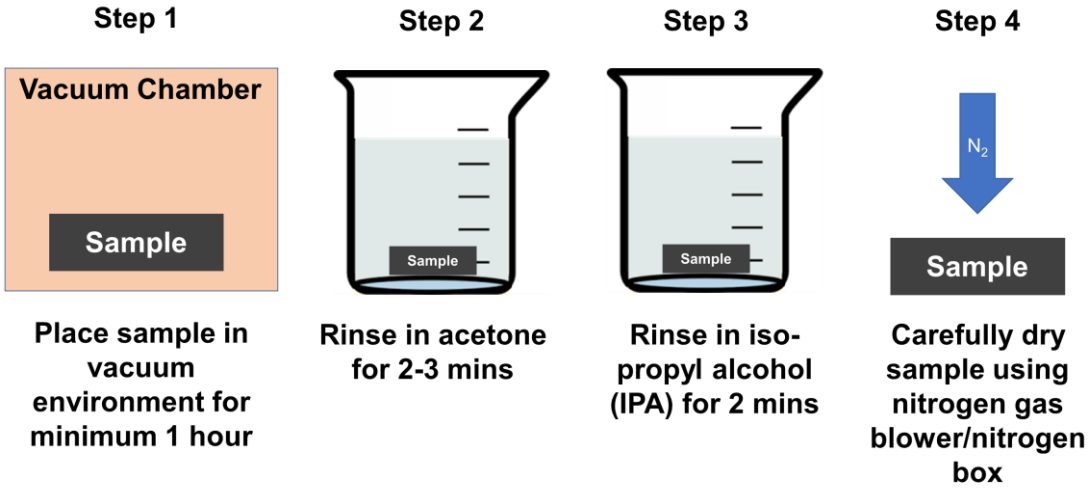

Figure 0.7 Post-transfer cleaning steps for the sample to remove any minute PDMS residues.

1.11.6 Conclusion

In this study, I have made significant advancements in the development of a robust transfer system for 2D materials, enabling their seamless integration into on-chip devices and the construction of heterostructures for various applications, particularly in the field of optoelectronics. The novel approach incorporates a cutting-edge micro-stamper and a thin bendable film, revolutionizing the transfer process by ensuring high reliability, and repeatability, and eliminating cross-contamination issues commonly encountered with other transfer methods. This breakthrough achievement brings chip-industry level repeatability to the integration of 2D materials, a crucial aspect for achieving reliable device performance. Furthermore, I have successfully demonstrated the versatility of the

transfer system through a range of applications involving active photonic, optoelectronic, and electrical devices. Notably, I have achieved a remarkable transfer precision of less than 10 μm in the current implementation. The integration of 2D materials using our transfer system provides a standardized platform that accelerates research efforts and facilitates large-scale commercial integration of these materials for various applications.

1.12 Wet etching monolayer

Wet etching of substrates to obtain monolayer 2D material flakes is a common technique in the field of 2D material research. One popular method involves the use of a potassium hydroxide (KOH) solution combined with deionized (DI) water. This process allows for the selective removal of the substrate material while leaving behind the desired monolayer 2D material flakes [19]. The wet etching process begins by preparing a solution of KOH and DI water with a specific concentration of 20g KOH in 100 ml DI water. The concentration and temperature of the solution can be adjusted to control the etching rate. The substrate containing the desired monolayer 2D material is then immersed in the solution for a certain duration.

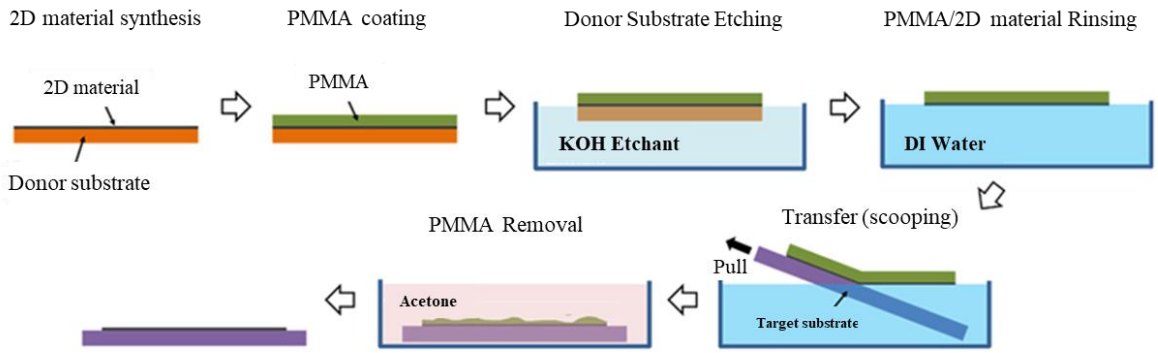

Figure 0.8 Schematic of the conventional wet transfer process of two-dimensional material using Poly (methyl methacrylate) as a transfer film [19].

During the etching process, the KOH solution reacts with the substrate material, dissolving it selectively. The etching rate depends on factors such as the concentration of KOH, temperature, and exposure time. It is essential to carefully monitor and control these parameters to achieve the desired thickness and quality of the monolayer 2D material flakes. Once the etching process is complete, the substrate is thoroughly rinsed with DI water to remove any residual etchant and by-products. The remaining monolayer 2D material flakes are left on the substrate, ready for further characterization or transfer onto another substrate for device fabrication.

Wet etching in a KOH solution offers several advantages for obtaining monolayer 2D material flakes. It is a relatively simple and cost-effective method that can be performed in a laboratory setting. The process is highly scalable, allowing for the batch production of large quantities of monolayer flakes. Additionally, the selectivity of KOH towards the

substrate material ensures minimal damage to the monolayer 2D material during the etching process.

However, wet etching in KOH solution also has some limitations. It may be challenging to achieve uniform etching across large substrate areas, leading to variations in the thickness and quality of the obtained flakes. The choice of substrate material is critical as it should be compatible with the KOH etchant. Furthermore, the etching process may introduce defects or contaminants in the monolayer 2D material, requiring additional post-etching treatments.

In summary, wet etching in a KOH solution combined with DI water is a widely used method to obtain monolayer 2D material flakes. It offers simplicity, scalability, and selectivity, making it an essential technique in the fabrication and research of various 2D material-based devices and systems. Researchers continue to refine and optimize the wet etching process to improve the yield, uniformity, and quality of the obtained monolayer 2D material flakes.

1.13 References – Chapter 3

[1] R. Maiti *et al*, "Loss and coupling tuning via heterogeneous integration of MoS2 layers in silicon photonics [Invited]," *Optical Materials Express*, vol. 9, *(2)*, pp. 751, 2019. Available: https://search.proquest.com/docview/2186772368. DOI: 10.1364/OME.9.000751.

[2] K. S. Novoselov *et al*, "Room-Temperature Quantum Hall Effect in Graphene," *Science,* vol. 315, *(5817),* pp. 1379, 2007. Available: https://agris.fao.org/agris-search/search.do?recordID=US201300755172. DOI: 10.1126/science.1137201.

[3] C. Patil, R. Maiti and V. J. Sorger, "WS2 monolayer integrated photodetector," in May 2020, pp. 1-2.

[4] R. Maiti *et al*, "Strain-engineered high-responsivity MoTe2 photodetector for silicon photonic integrated circuits," *Nature Photonics,* vol. 14, *(9),* pp. 578-584, 2020. Available: https://search.proquest.com/docview/2436973892. DOI: 10.1038/s41566-020-0647-4.

[5] H. Agarwal *et al*, "2D-3D integration of hexagonal boron nitride and a high-κ dielectric for ultrafast graphene-based electro-absorption modulators," *Nature Communications,* vol. 12, *(1),* pp. 1070, 2021. Available: https://www.ncbi.nlm.nih.gov/pubmed/33594048. DOI: 10.1038/s41467-021-20926-w.

[6] A. Castellanos-Gomez, N. Agraït and G. Rubio-Bollinger, "Optical identification of atomically thin dichalcogenide crystals," *Applied Physics Letters,* vol. 96, *(21),* pp. 213116-3, 2010. Available: http://dx.doi.org/10.1063/1.3442495. DOI: 10.1063/1.3442495.

[7] Y. S. Ang, H. Y. Yang and L. K. Ang, "Universal Scaling Laws in Schottky Heterostructures Based on Two-Dimensional Materials," *Physical Review Letters,* vol.

121, *(5),* pp. 056802, 2018. Available: https://www.ncbi.nlm.nih.gov/pubmed/30118283. DOI: 10.1103/PhysRevLett.121.056802.

[8] Y. Gong *et al*, "Vertical and in-plane heterostructures from WS2/MoS2 monolayers," *Nature Materials,* vol. 13, *(12),* pp. 1135-1142, 2014. Available: https://www.ncbi.nlm.nih.gov/pubmed/25262094. DOI: 10.1038/nmat4091.

[9] S. Masubuchi *et al*, "Autonomous robotic searching and assembly of two-dimensional crystals to build van der Waals superlattices," *Nature Communications,* vol. 9, *(1),* pp. 1413-12, 2018. Available: https://www.ncbi.nlm.nih.gov/pubmed/29650955. DOI: 10.1038/s41467-018-03723-w.

[10] G. F. Schneider *et al*, "Wedging Transfer of Nanostructures," *Nano Letters,* vol. 10, *(5),* pp. 1912-1916, 2010. Available: http://dx.doi.org/10.1021/nl1008037. DOI: 10.1021/nl1008037.

[11] C. Lee *et al*, "Boron nitride substrates for high-quality graphene electronics," *Nature Nanotechnology,* vol. 5, *(10),* pp. 722-726, 2010. Available: http://dx.doi.org/10.1038/nnano.2010.172. DOI: 10.1038/nnano.2010.172.

[12] J. Lim *et al*, "Pattern Pick and Place Method for Twisted Bi- and Multi-Layer Graphene," *Materials,* vol. 12, *(22),* pp. 3740, 2019. Available: https://www.ncbi.nlm.nih.gov/pubmed/31766213. DOI: 10.3390/ma12223740.

[13] C. Patil *et al*, "Highly accurate, reliable, and non-contaminating two-dimensional material transfer system," *Applied Physics Reviews,* vol. 9, *(1),* pp. 11419, 2022. Available: http://dx.doi.org/10.1063/5.0071799. DOI: 10.1063/5.0071799.

[14] H. M. Gramling *et al*, "Spatially Precise Transfer of Patterned Monolayer WS2 and MoS2 with Features Larger than 104 μm2 Directly from Multilayer Sources," 2019. Available: https://escholarship.org/uc/item/2s44h6sn.

[15] V. Nguyen *et al*, "Deterministic Assembly of Arrays of Lithographically Defined WS2 and MoS2 Monolayer Features Directly From Multilayer Sources Into Van Der Waals Heterostructures," *J. Micro Nano-Manuf,* vol. 7, *(4),* 2019. Available: http://dx.doi.org/10.1115/1.4045259. DOI: 10.1115/1.4045259.

[16] P. J. Zomer *et al*, "A transfer technique for high mobility graphene devices on commercially available hexagonal boron nitride," *Applied Physics Letters,* vol. 99, *(23),* pp. 232104-3, 2011. Available: https://www.narcis.nl/publication/RecordID/oai:pure.rug.nl:publications%2Fb633b36a-0d2d-437c-a467-6ea723198d3a. DOI: 10.1063/1.3665405.

[17] R. A. Hemnani *et al*, "2D material printer: a deterministic cross contamination-free transfer method for atomically layered materials," *Tdm,* vol. 6, *(1),* pp. 15006, 2019. Available: https://iopscience.iop.org/article/10.1088/2053-1583/aae62a. DOI: 10.1088/2053-1583/aae62a.

[18] Q. Zhao *et al*, "An inexpensive system for the deterministic transfer of 2D materials," *Jpmater,* vol. 3, *(1),* pp. 16001, 2020. Available: https://iopscience.iop.org/article/10.1088/2515-7639/ab6a72. DOI: 10.1088/2515-7639/ab6a72.

[19] Chan Kim *et al*, "A Review on Transfer Process of Two-dimensional Materials," *Tribology and Lubricants,* vol. 36, *(1),* pp. 1-10, 2020. Available: https://www.dbpia.co.kr/journal/articleDetail?nodeId=NODE09313319. DOI: 10.9725/kts.2020.36.1.1.

Advancing High-Performance Photonics Devices Using Two-Dimensional Material Integration

1.14 Post-passive tuning of silicon photonic circuits

1.14.1 Introduction

In this study, I focus on the monolithic integration of MoS_2 with silicon photonics to explore its impact on optical absorption and index shift when added to a silicon photonic waveguide and micro ring resonator (MRR). This integration platform opens new possibilities for nano-optics and photonics applications, as the spectral distance of each TMDC's exciton relative to the probing wavelength of the waveguide introduces different effects on the photonic structures. Silicon photonics has gained significant interest as an integration platform for optical datacom and telecom applications. However, its weak

electro-optic properties and indirect bandgap limit the functionality of optoelectronic devices. Hybrid or heterogeneous photonic integration, coupled with the integration of 2D materials, offers a promising solution. By leveraging the strong van der Waals forces in 2D materials, they can be seamlessly integrated with photonic chips, providing a wide range of electronic and optical properties for light generation, modulation, and detection. Despite the potential benefits, state-of-the-art transfer techniques for TMDCs pose challenges in terms of cross-contamination. To address this, I have developed a novel 2DMTS discussed in Chapter 3, enabling precise transfers of atomic layers onto integrated photonic chips. In this work, I demonstrate a heterogeneous platform for studying the physical properties of TMDCs on silicon photonics, specifically focusing on MoS_2. By varying the coverage length and thickness of MoS_2, we investigate its impact on optical loss and refractive index change in silicon waveguides and MRRs. The results show that the integration of monolayer MoS_2 induces negligible loss but offers significant index-tuning potential, paving the way for future developments in active optoelectronic device technology.

1.14.2 Methods

The study is conducted on taped-out silicon (Si) photonic chips provided by Applied Nanotools, inc. To isolate the influence solely from the atomically layered materials, it is crucial to maintain consistent physical parameters before and after the transfer of the 2D materials. To achieve this, first, a uniform layer is coated with polymethyl methacrylate

(PMMA) with a thickness of approximately 300 nm -350 nm as a cladding layer to improve the coupling efficiencies of the grating couplers (GC). Additionally, a material transfer opening is created by electron beam lithography preserving the coupling conditions on the chip. The 2D materials are then transferred onto the targeted areas of the devices.

Few-layer MoS2 flakes are obtained using the scotch tape exfoliation technique, while monolayers are triangular flakes grown on Si/SiO2 substrates via a chemical vapor deposition (CVD) process. The flakes are transferred using the 2DMTS tool (Fig. 4.1.1a-c). After the transfer, the devices are tested for optical transmission and spectral shift to evaluate the impact of the TMDCs layer in terms of coverage length and thickness on the waveguide and microring resonator (MRR), respectively.

For measuring the hybrid TMDC-Si devices, the experimental setup consists of a tunable laser source (Agilent 8164B) and a broadband source (AEDFA-PA-30-B-FA) for injecting light into the grating coupler optimized for TM mode propagation in the waveguide. The light output from the MRR is coupled to an output fiber through a similar grating coupler and detected using a detector or an optical spectral analyzer (OSA202). The fundamental modes of the waveguide incorporating the different thicknesses of the MoS_2 layer are determined through finite element method (FEM) simulations using the mode analysis tool in COMSOL Multiphysics.

1.14.3 Results and discussion

The optical properties of TMDCs, such as MoS_2, are largely influenced by excitons, which are bound electron-hole pairs with strong binding energy resulting from quantum confinement and weak screening of the Coulomb interaction [1]. For active integrated device structures, it is necessary to systematically characterize the individual material system, including losses and effective index changes within the targeted operational wavelength range. The focus of the study is on analyzing the loss and coupling behavior as a function of monolayer coverage and thickness of MoS_2. Our investigation concentrates on the Si waveguide, located away from the excitonic transitions of MoS_2 (A exciton ~1.88 eV and B exciton ~2.06 eV) [2]. A minimal loss impact is anticipated but expects a significant index change upon heterogeneous integration. Therefore, I studied the change in waveguide bus-to-ring coupling by manipulating the phase of the MRR through the introduction of MoS_2. To evaluate the coupling change, I measured the corresponding transmission spectra, which exhibit variations compared to the bare ring, indicating MRR mode index tuning (Fig 4.1.1e). The improvement in coupling can be attributed to shifting the MRR from the over-coupled regime towards the critically coupled regime by introducing losses. These losses are evident as the quality factor decreases with increasing flake thickness, suggesting a gradual increase in loss primarily due to scattering effects

caused by the small impedance mismatch between the bare and MoS_2-covered sections of the ring (Fig 4.1.1f).

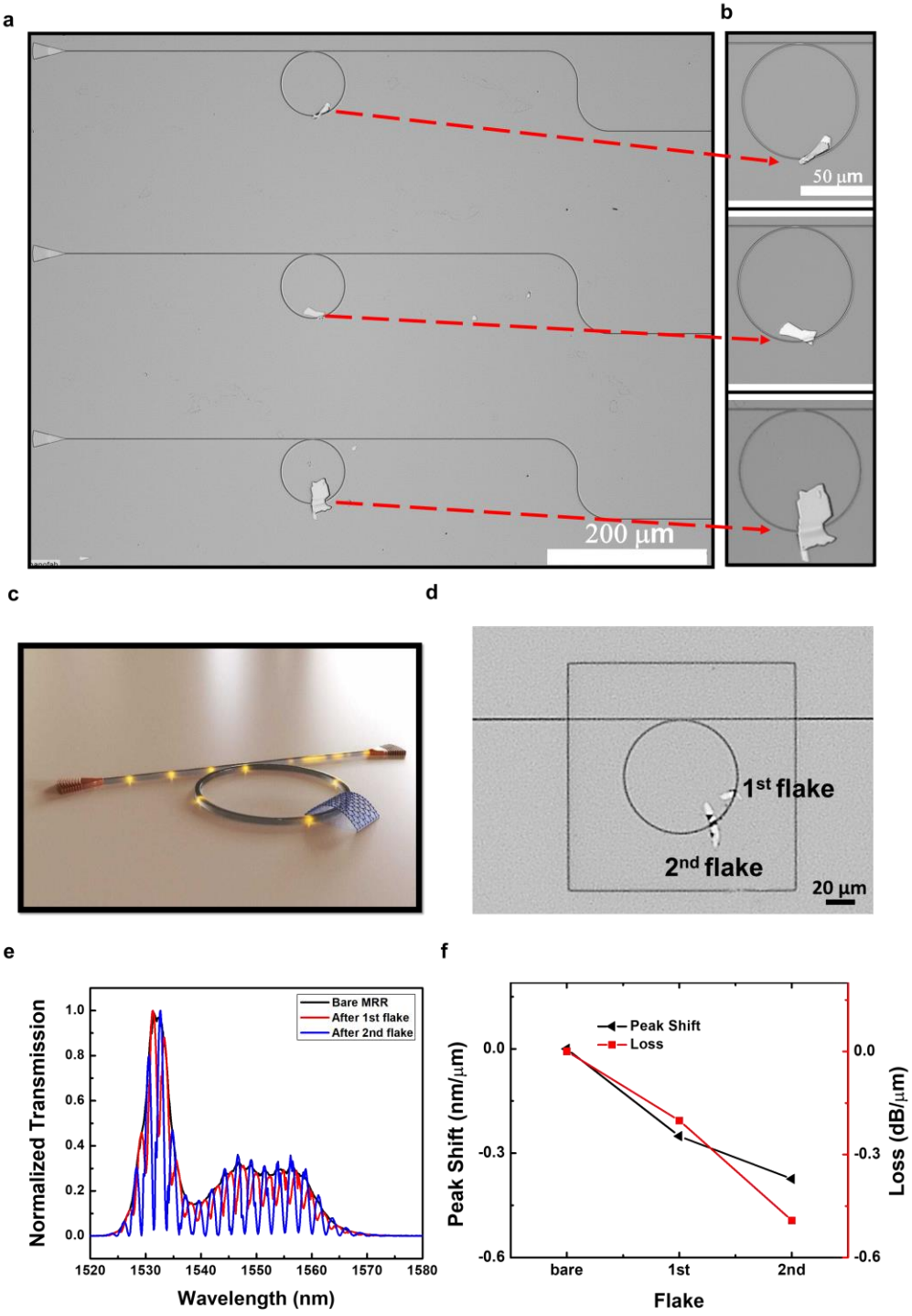

Figure 0.1 2DMTS performance test for repeatability and robustness on assembling 2D structures atop photonic integrated circuit waveguides. (a) Optical microscope images at 20x magnification of MoS_2 flakes transferred on Si-MRR devices in an array on-chip separated by 200nm distance from each other. (b) Zoomed in at 50x magnification to show the flake position on devices. Silicon micro-ring resonator post-coupling enhancement using MoS_2 thin flakes. (c) Schematic (d) optical microscope image of an MRR (D = 80 μm & W = 500 nm) covered by two MoS_2 flakes precisely transferred using our developed 2DMTS tool. (e) Spectral transmission output before and after the transfer of MoS_2 shows an improvement in coupling efficiency. The improved resonance fringes can be observed in the graph. (f) Resonance peak shift and optical loss after transfer of each flake can be observed showing linear absorption loss and variation in peak shift of resonance [3].

To understand the coupling effect in the microring resonator (MRR), the round-trip transmission coefficients (α) as a function of coverage are studied. These coefficients quantify the power transfer between the waveguide and the MRR, allowing us to optimize the fringe visibility toward critical coupling. Analyzing the coupling coefficients helps to assess the impact of coverage length and flake thickness on the MRR's resonance shifts and coupling efficiency. The transmission T for all-pass MRR is given by,

$$T_n = \frac{a^2 + r^2 - 2ar * cos\varphi}{1 + a^2 r^2 - 2ar * cos\varphi} \qquad \text{_____1}$$

where φ is the round-trip phase shift, r corresponds to the self-coupling coefficient and a represents the round-trip transmission coefficient. The a is given by,

$$a^2 = \exp\left(-\propto_{Si} (2\pi R - l)\right) * \exp\left(-\propto_{TMD-Si} * l\right) \quad \text{_____2}$$

where l defines the coverage length, R is the radius of the MRR, $\propto_{Si}$ and $\propto_{TMD-Si}$ represents the linear propagation losses of the Si waveguide and MoS_2 coverage region on the Si MRR respectively. To quantitatively determine the propagation loss I used the cutback method by integrating mono to a few layers of MoS_2 on linear waveguides of different lengths and measuring the relative transmission (Fig. 4.1.2a,b,c). By fitting the data linearly, we obtain propagation losses of 0.0009 dB/μm, 0.012 dB/μm, and 0.037 dB/μm for bare Si, monolayer, and multi-layer flakes, respectively (Fig. 4.1.2.d). To isolate the additional loss induced by MoS_2, the loss of the bare Si device was subtracted from the loss observed in the hybrid structure, resulting in 0.011 dB/μm and 0.036 dB/μm for monolayer and multilayer flakes, respectively.

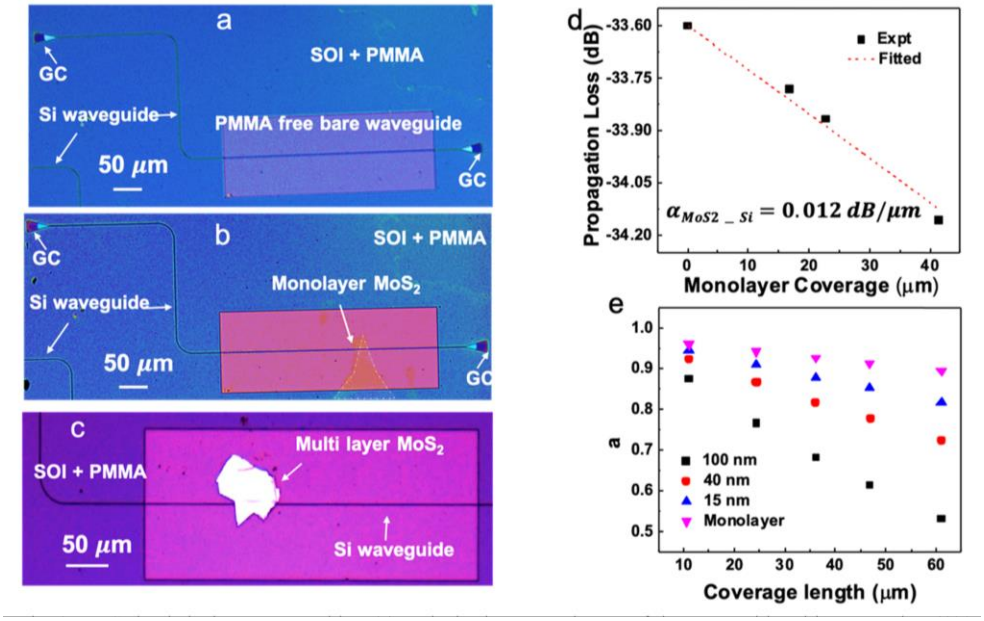

Figure 0.2 MoS2 loaded Linear waveguides. (a) optical microscope image of the waveguide with an opening (400 μm x 100 μm) for TMDC transfer to keep all physical parameters unchanged during the optical measurement. (b) & (c) optical microscope image of waveguide covered by a monolayer CVD grown and a multilayer exfoliated flake with coverage length 10 μm and 50 μm, respectively. (d) Optical loss output as a function of monolayer coverage length originates mainly due to the edge scattering effect. The propagation loss (αTMDC-Si) for a TMDC-covered portion of the ring is found to be 0.012 dB/μm using cutback measurement. (e) The tunability of round-trip transmission coefficients explains the coupling improvement as a function of coverage length for four different thickness values [4].

These results provide valuable insights into the impact of MoS_2 on the overall propagation loss in integrated photonic devices. The observed loss in the waveguides can be attributed to a combination of absorption and edge-scattering effects caused by the

flakes. However, since the wavelength of propagation through the waveguide is well below the bandgap of MoS_2 (1.2-1.8 eV), the losses due to absorption are negligible. To gain further insights, we plot the round-trip transmission loss for four different thickness values, incorporating the propagation loss in Eq. (2) (Fig. 4.1.2e). The plot shows that the round trip transmission coefficient (a) decreases from 0.88 to 0.52 for multilayer flakes (~100 nm) and from 0.96 to 0.90 for monolayer flakes as a function of coverage length. This result explains the improvement in fringe visibility, as the system transitions from an over-coupled regime towards a critically-coupled regime (a = 1 represents the zero-loss condition of the ring). Thus, the loss of tunability in MRRs can be controlled by adjusting the coverage length and thickness. We conclude that, for a given device, the coverage length and thickness can be determined to configure the device at a critically coupled condition for optimized light-matter interaction [5].

Furthermore, Fig. 4.1.2e demonstrates that the loss increases as the thickness of the flakes increases, primarily due to an increase in surface roughness. The root-mean-square (RMS) roughness of the Si waveguide is measured to be 1.3 ± 0.6 nm. Consequently, the monolayer MoS2 flake on the waveguide (RMS roughness: 0.8 ± 0.2 nm) exhibits a significantly rougher surface compared to when it is on SiO2 (RMS roughness: 0.20 ± 0.07 nm). In the case of multilayer flakes, the surface roughness of the underlying substrate does

not play a significant role, as the RMS roughness for a 40 nm MoS_2 flake is measured to be 3.5 ± 0.9 nm and 3.7 ± 1.3 nm on both SiO2 and Si waveguide, respectively.

Si-based MRRs are highly advantageous for the sensitive detection of unknown analytes in various applications [6], [7]. The detection mechanism relies on changes in the refractive index of the top cladding of the MRR. These changes can be detected by the evanescent tail of the optical mode, which is governed by the effective mode index (n_{eff}), and can be translated into a resonance shift (Δλ). In our experiments, we observe a monotonic redshift of 1.5 nm in the resonance upon increasing the monolayer coverage length from 10 to 60 μm (Fig. 4.1.3c).

The resonant wavelength (λres) of an MRR is proportional to the effective refractive index of the propagating mode in the circular waveguide [7]. Therefore, the change in effective mode index (Δneff) resulting from the transfer of MoS2 flakes compared to the bare ring is related to the change in resonance shift (Δλ) according to equation (3).

$$\Delta n_{eff} = \frac{\Delta\lambda}{\lambda_{res}} * n_{eff,bare} \qquad \text{_____3}$$

where $n_{eff,bare}$ is the effective mode index for bare Si waveguide. The effective index for the bare waveguide was calculated from FEM Eigenmode analysis choosing the TM mode in correspondence with the ANT taped-out chip TM-grating designs used in measurements.

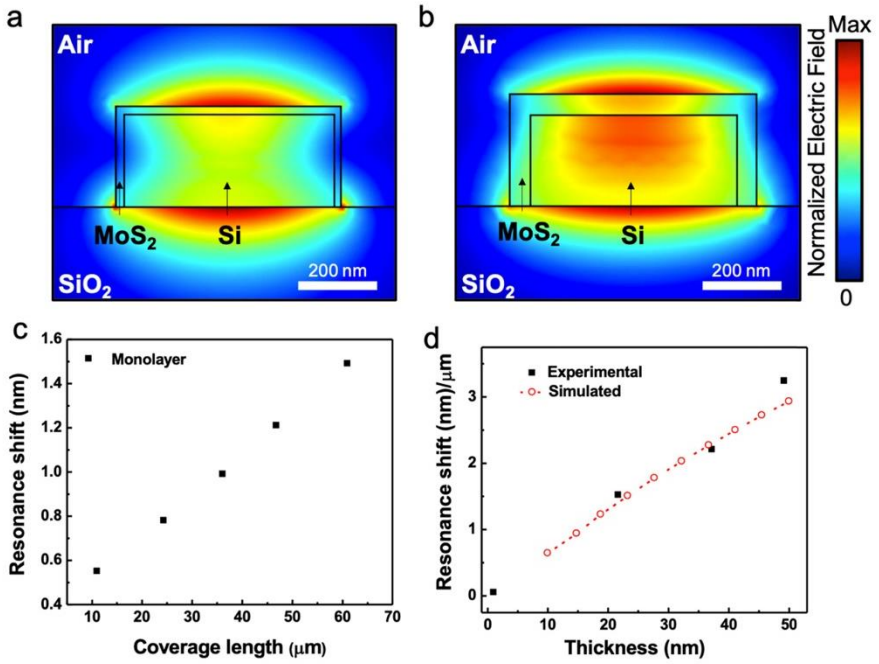

Figure 0.3 Mode profile (electric |E|-field), obtained through Eigenmode analysis, for the portion of the ring with MoS2 transferred flakes (a) 20 nm and (b) 50 nm thick (Scale bar 200 nm). Variation of Resonance shift ($\Delta\lambda$) and effective index change ($\Delta neff$) extracted from (c) as a function of MoS2 coverage length and (d) thickness, which is fully corroborated by a numerical simulation study [4].

Since MRR is partially covered by MoS_2 flakes the effective refractive index of the ring can be formulated as an effective length-fraction index via [5],

$$\Delta n_{eff,MRR} = \frac{(2\pi R - l) * n_{eff,bare} + l * n_{eff}}{2\pi R} \qquad _____ 4$$

The effective index for the monolayer-covered waveguide is determined to be 1.723 for the TM mode. To obtain the effective index (n_{eff}) for flakes with different thicknesses, we utilize Finite Element Method (FEM) Eigenmode analysis. The refractive index values for MoS2 are obtained from [8], while the refractive index for silicon is obtained from [9].

Figs. 4.1.3a,b display the normalized in-plane (|Ex|) electric field distribution for the TM mode along the device, integrating MoS_2 layers with thicknesses of 20 nm and 50 nm, respectively. The electric field intensity is higher within the MoS_2 layer, indicating reduced leakages into the air and substrate. This observation suggests higher confinement for the multilayer MoS_2 (50 nm). This measurement is specifically designed for the TM mode, where the electric field component parallel to the side walls (y-direction) is negligible. Consequently, there is no significant interaction or coupling between the evanescent wave and the flake positioned on the lateral side of the photonic waveguide.

Using Eq. (4), we can calculate $\Delta neff$ and, thus, the resonance shift ($\Delta\lambda$). The calculated resonance shift shows a clear correlation with our experimental data (Fig. 4.1.3d). We map out the resonance shift as a function of MoS_2 flake thickness (Fig. 4.1.3d, i) up to 50 nm and observe a resonance shift per coverage length of 0.064 nm/μm, exceeding the resolution limit of our spectrometer (~0.03 nm). These results suggest that integrating mono-multilayer MoS_2 on a Si photonic platform could be a promising approach for future active modulator devices operating at telecommunication wavelengths.

1.14.4 Conclusion

In conclusion, our study successfully demonstrates the interaction between mono to multi-layers of MoS2 and Silicon photonic waveguides and micro ring cavities. By varying the coverage length and thickness of MoS2, we were able to tune the coupling regime of the

ring from over-coupled to under-coupled. Through the extraction of different coupling and loss coefficients, we provided insights into the physical mechanism behind this tunable coupling. Furthermore, we determined the critical coverage for a given ring resonator, which is crucial for achieving the maximum extinction ratio in active modulators. By mapping out the resonance shift as a function of monolayer coverage and thickness of MoS2 flakes, we observed a resonance shift of 0.064 nm/μm, which aligned well with our simulated results. These findings on passive Silicon photonic platforms offer valuable insights and tools for future developments in heterogeneous integrated photonic and optoelectronic devices. They contribute to the advancement of active modulators and pave the way for further studies and applications in this field.

1.14.5 References

[1] M. M. Ugeda *et al,* "Giant bandgap renormalization and excitonic effects in a monolayer transition metal dichalcogenide semiconductor," *Nature Materials,* vol. 13, *(12),* pp. 1091-1095, 2014. Available: https://www.ncbi.nlm.nih.gov/pubmed/25173579. DOI: 10.1038/nmat4061.

[2] A. Splendiani *et al,* "Emerging Photoluminescence in Monolayer MoS2," *Nano Letters,* vol. 10, *(4),* pp. 1271-1275, 2010. Available: http://dx.doi.org/10.1021/nl903868w. DOI: 10.1021/nl903868w.

[3] C. Patil *et al*, "Highly accurate, reliable, and non-contaminating two-dimensional material transfer system," *Applied Physics Reviews,* vol. 9, *(1),* pp. 11419, 2022. Available: http://dx.doi.org/10.1063/5.0071799. DOI: 10.1063/5.0071799.

[4] R. Maiti *et al*, "Loss and coupling tuning via heterogeneous integration of MoS2 layers in silicon photonics [Invited]," *Optical Materials Express,* vol. 9, *(2),* pp. 751, 2019. Available: https://search.proquest.com/docview/2186772368. DOI: 10.1364/OME.9.000751.

[5] R. Maiti *et al*, "Microring Resonators Coupling Tunability by Heterogeneous 2D Material Integration," 2018. Available: https://arxiv.org/abs/1807.03945. DOI: 10.48550/arxiv.1807.03945.

[6] I. M. White and X. Fan, "On the performance quantification of resonant refractive index sensors," *Optics Express,* vol. 16, *(2),* pp. 1020-1028, 2008. Available: https://www.ncbi.nlm.nih.gov/pubmed/18542175. DOI: 10.1364/OE.16.001020.

[7] G. N. Tsigaridas, "A Study on Refractive Index Sensors Based on Optical Micro-Ring Resonators," *Photonic Sens,* vol. 7, *(3),* pp. 217-225, 2017. Available: http://lib.cqvip.com/qk/71176X/201703/672494483.html. DOI: 10.1007/s13320-017-0418-0.

[8] N. McEvoy, "Investigation of the optical properties of MoS2 thin films using spectroscopic ellipsometry," *Applied Physics Letters,* vol. 104, *(10),* 2014. Available: https://search.proquest.com/docview/2127685849. DOI: 10.1063/1.4868108.

[9] D. T. Pierce and W. E. Spicer, "Electronic Structure of Amorphous Si from Photoemission and Optical Studies," *Physical Review. B, Solid State,* vol. 5, *(8)*, pp. 3017-3029, 1972. . DOI: 10.1103/PhysRevB.5.3017.

1.15 Strain effect in 2D material for bandgap tuning for Optical Detection

1.15.1 Introduction

Strain engineering has proven to be an effective technique for enhancing the performance of electronic and photonic devices by modifying the band structure of traditional semiconductors such as Si/Ge and III-V materials [1], [2]. By applying strain, either through epitaxial growth techniques or mechanical deformation, the bandgap of these materials can be adjusted, resulting in improved mobility and other desirable properties [3]. In the case of 2D nanocrystals, such as MoS2 and MoTe2, the ability to sustain higher amounts of strain compared to bulk crystals makes them particularly promising for strain engineering applications [4], [5]. Even small amounts of strain (<2%) can significantly affect the bandgap, leading to changes in optical and electronic properties. For example, compressive strain increases the bandgap, while tensile strain decreases it, and in some cases, strain can even induce a transition from a semiconductor to a metal [6]. Despite the potential of strain-induced bandgap engineering in 2D materials, there is a lack of experimental evidence for its application in optoelectronic devices operating at telecommunication wavelengths. This wavelength range is crucial for applications such as

sensing, data communication, and signal processing. Currently, near-infrared photodetectors rely on materials like InGaAs, InP, and germanium, which have high absorption at telecommunication wavelengths but suffer from compatibility issues with silicon complementary metal-oxide-semiconductor (CMOS) technology [7].

The heterogeneous integration of 2D materials with photonic platforms offers several advantages for the development of optoelectronic devices. These materials exhibit strong exciton binding energy, tunable index of refraction, and compatibility with CMOS technology. Graphene-based photodetectors face challenges due to their gapless band structure, while black phosphorus shows promise but has limitations in terms of stability under ambient conditions. To address these challenges and explore the potential of strain engineering in 2D materials, this work focuses on the development of strain-engineered photodetectors integrated with silicon microring resonators (MRRs). By intentionally inducing strain in a multilayer $MoTe_2$ crystal flake placed on top of the MRR, a spatially varying strain profile is created, leading to a graded bandgap in the 2D material. This strain distribution is achieved by wrapping the $MoTe_2$ nanocrystal around a non-planarized waveguide, aligning the strain region with the optical mode of the waveguide.

Experimental results demonstrate the successful implementation of the strain-engineered photodetector, operating at the relevant wavelength of 1550 nm. The device exhibits a photoresponsivity of 10 mA/W^{-1} (for a 40 nm thick flake) and 0.5 A/W^{-1} (for a 60 nm thick flake) at a voltage of -2 V. It also demonstrates a low dark current of only 13

nA, a noise equivalent power (NEP) of 90 pW/√Hz and can operate at frequencies up to approximately 35 MHz. This showcases the potential of strain-engineered photodetectors using 2D materials integrated with established photonic platforms, opening new possibilities for optoelectronic components in integrated photonics [8].

1.15.2 Results and discussion

The manipulation of mechanical deformation, such as strain, provides a means to continuously tune the properties of 2D materials, impacting both their electronic and photonic characteristics [9]. In this study, our objective is to leverage local uniaxial strain to decrease the optical bandgap of multilayer $MoTe_2$ nanocrystals integrated with silicon photonic waveguide-based structures. Specifically, we demonstrate the feasibility of strain-engineered photodetection at the technologically relevant wavelength of 1550 nm as shown in Fig. 4.2.1. Bulk $MoTe_2$ is an indirect bandgap semiconductor with a bandgap of 1.04 eV. In its unstrained form, multilayer $MoTe_2$ exhibits low absorption below the bandgap energy, resulting in low photoresponsivity at 1550 nm [10] as demonstrated in Fig. 4.2.2.

To overcome this limitation, we intentionally wrap the 2D film around a non-planarized waveguide with a height of approximately 220 nm, inducing localized tensile strain near the waveguide (as depicted in Fig. 4.2.1c). The performance of photonic devices based on 2D materials is fundamentally determined by the interaction between the optical waveguide

mode and the 2D nanocrystal. Conventionally, a common approach is to place the 2D film on a planar waveguide and couple it evanescently to the optical mode, allowing the interaction length to be determined by both the thickness and longitudinal length of the 2D film [11]. However, this brute-force engineering technique leads to larger device footprints, negatively impacting the performance of the electrical device in terms of energy-per-bit efficiency and resistor-capacitor response time, due to increased electrical capacitance.

To address these challenges and enhance device performance, we integrate 2D nanocrystals with microring resonators (MRRs). This integration enables a more efficient weak light-matter interaction, reducing the device footprint and improving electrical performance (as illustrated in Figure 4.2.1). By exploiting strain-induced modifications in the optical properties of MoTe2, we achieve continuous tuning of the bandgap and enable efficient photodetection at 1,550 nm. This approach holds promise for developing compact and high-performance photonic devices based on 2D materials integrated with MRRs.

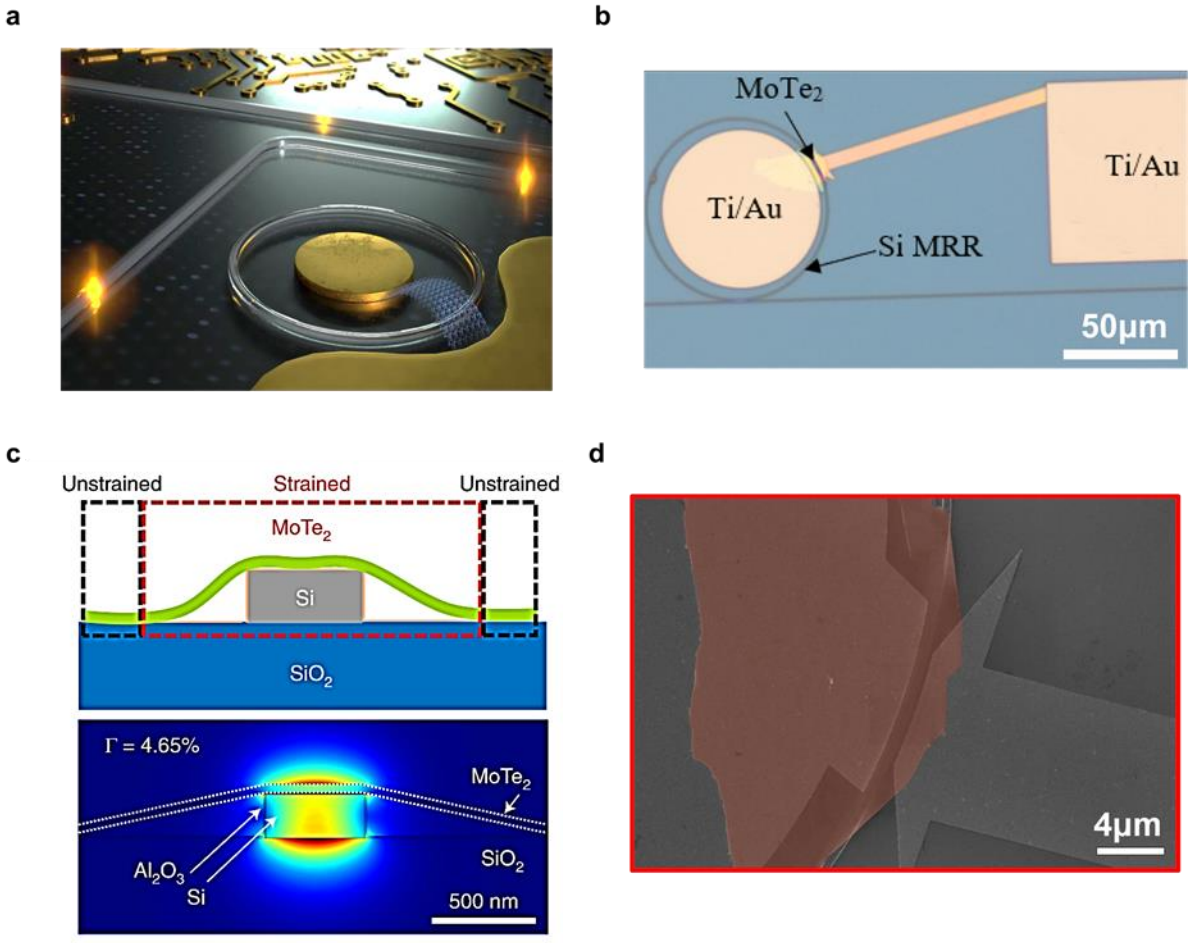

Figure 0.4 A Si-MRR integrated strain-engineered $MoTe_2$ photodetector. a) Schematic representation of $MoTe_2$-based integrated photodetector for strainoptronics application built using the 2DMTS b) The structure of Si-MRR (radius (r)=40μm, height (h)=220nm, width (w)=500nm), and electrical contacts are represented in the optical microscope image. c) A schematic of a bent 2D nanocrystal (MoTe2) atop a non-planarized waveguide, which introduces strong localized strain on top of, and in close vicinity to, the waveguide (red dashed box), whereas the flakes away from the waveguide are unstrained (black dashed boxes). A simulated mode profile for a MoTe2-integrated waveguide for a transverse magnetic mode is shown below, in which the cross-sectional

structure is extracted from an AFM micrograph [8]. d) SEM image shows the coverage of the flake on one of the Si-MRR device showing the coverage of the flake on devices.

We measured the photocurrent from a monolayer $MoTe_2$-based photodetector on top of a planarized waveguide by using my developed 2DMTS tool followed by an EBL process for the electrical contacts. The schematic cross-section of 2D MoTe2 flakes represents the unstrained device as compared to its strained counterpart (Fig. 4.2.2a, b). The 3D AFM results show a small variation of the height of 10 nm across the waveguide (w=500 nm) (Fig. 4.2.2d, e). Typical I-V curve showing small enhancement of photocurrent for different input optical power at 1550 nm, showing a photoresponsivity of ~1 mA/W which is less than ~6 times and supports our DFT study of strain-induced band gap lowering, thus enabling higher photo response at 1550 nm (Fig. 4.2.2f).

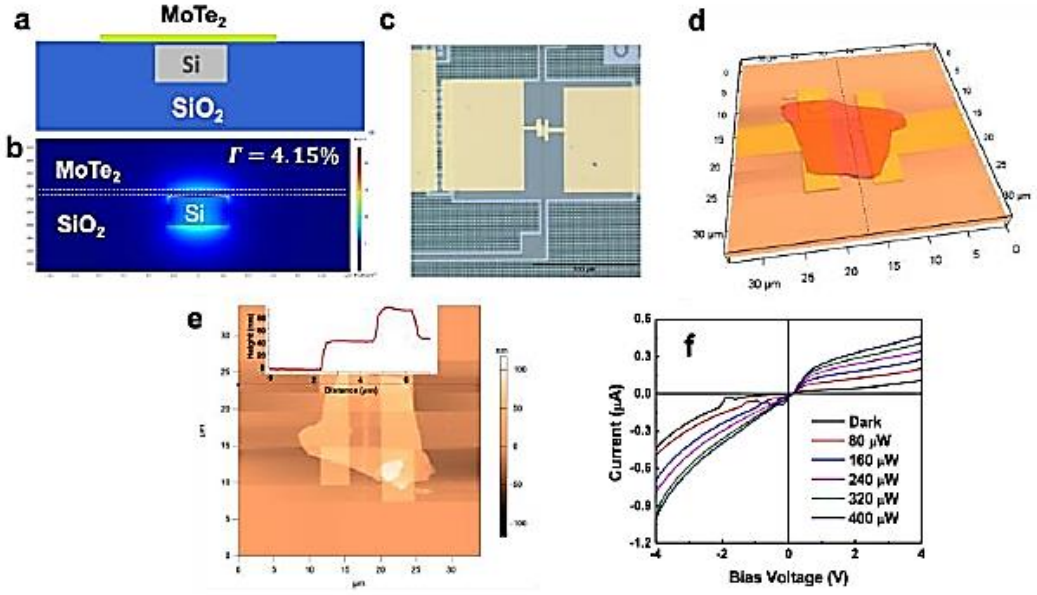

Figure 0.5 Photo response of a MoTe2 photodetector on planarized waveguide a) Schematic cross-sectional diagram of relaxed ML MoTe2 flake wrapped on top of a planarized waveguide. b) Simulated mode profile for MoTe2 integrated planarized waveguide for TM mode where the mode overlap factor (Γ) is found to be 4.15%. c) Optical micrograph of the device (top view) where a few layers of MoTe2 flakes are integrated on a planarized Si waveguide. d) 3D AFM topography showing the flat ML MoTe2 flakes of thickness ~50 nm on top of a planarized waveguide (h=220 nm and w=500 nm). e) AFM micrograph (top view) showing height profile (along the red line). f) Typical I-V characteristics of M-S-M diode showing asymmetrical nature under different optical power.

The precise placement of exfoliated MoTe2 flakes onto a thin Al_2O_3 layer is achieved using our in-house-developed 2D material printer technique (Fig. 4.2.1b, d, Chapter 3.2, Fig. 4.2.3). The 10 nm thin Al_2O_3 layer acts as an electrical isolation layer between the silicon-on-insulator photonic chip and the $MoTe_2$ nanocrystal. The optical mode at 1550 nm (Fig. 4.2.1c) couples with the MoTe2 layer through the evanescent field, leading to optical absorption and the generation of photogenerated carriers. These carriers are collected by two metal electrodes made of titanium (5 nm thickness) and gold (45 nm thickness), which are contacted on opposite sides of the microring resonator (MRR) (Fig. 4.2.1b). The MoTe2 two-terminal photodetector has a channel length of approximately 800 nm (with a waveguide width of about 500 nm), and one of the electrical contacts is positioned around 100 nm away from the edge of the ring resonator to create a lateral metal-

semiconductor-metal (M-S-M) junction that overlaps with the waveguide mode (Fig. 4.2.1c). Two exemplary devices with different dimensions of the 2D material (device 1 with a coverage length and thickness of transferred flakes of 15 μm and 31 nm, respectively, and device 2 with a coverage length and thickness of 40 μm and 60 nm, respectively) on top of the ring resonator are discussed (Fig. 4.2.1d).

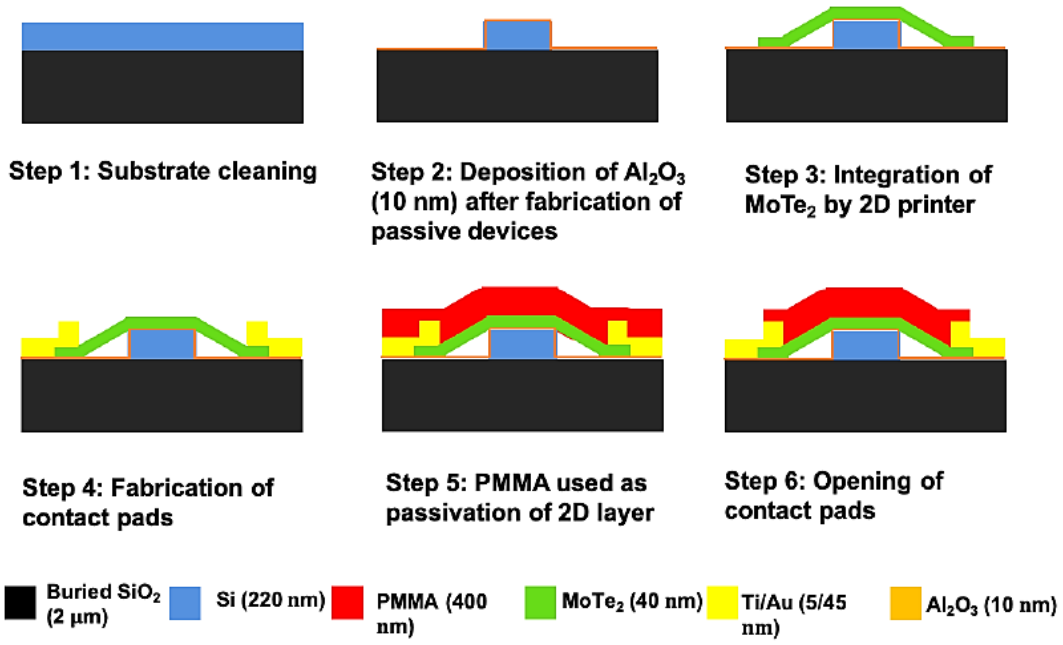

Figure 0.6 Fabrication process of Si MRR integrated MoTe2 photodetector a) pre-cleaning of SOI substrate, b) Silicon photonic platform, which includes micro ring resonator, was fabricated using SOI substrate with a thin 220nm Si layer with 2 μm buried oxide. The devices were patterned using electron-beam lithography using a negative resist ARN 7520. The patterned features were further etched using an Inductively Coupled Plasma (ICP) etching tool. The photoresist mask was removed using acetone wash and short oxygen plasma cleaning. c) 10 nm of Al2O3 is deposited by atomic layer deposition (ALD) on a taped-out Si photonic chip to isolate the MoTe2 flakes from Si; the

sample is prebaked at 180 0C for 2 minutes to remove the surface moisture. Afterward, the exfoliated MoTe2 flake is deterministically transferred on top of Si MRR by using 2DMTS. d) Ti (5 nm)/Au (45 nm) is deposited by an electron beam evaporator followed by a lift-off process. e) A uniform PMMA layer is used as a cladding layer to improve the light coupling efficiency, followed by f) opening of electrical contact pads for the electrical measurement by using one EBL step.

A representative current-voltage (I-V) curve demonstrates efficient photodetection with a photocurrent to dark current at a bias of 2 V (Fig. 4.2.4a). The device exhibits a low dark current of around 13 nA at -1 V bias, which is two to three orders of magnitude lower than graphene and approximately two times lower than graphene-contacted transition metal dichalcogenide photodetectors, respectively [12], [13]. The symmetric nature of the I-V curve indicates the formation of two consecutive (Ti/MoTe2) Schottky junctions. The working principle of this detector involves the generation of photocarriers across the bandgap. The applied voltage bias across the two-terminal contacts enables the separation of charge carriers.

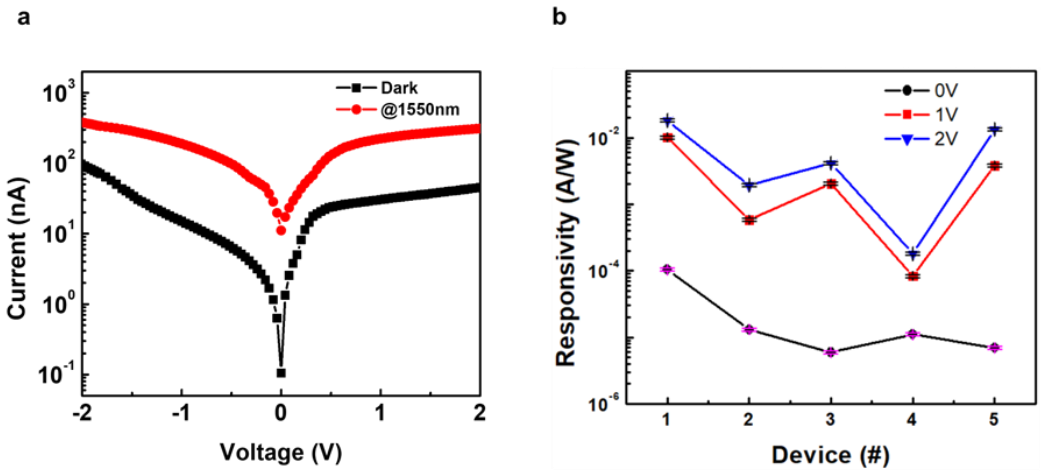

Figure 0.7 Photoresponse of the Au/MoTe2/Au integrated on MRR a) The I-V characteristics show the enhancement in current under the illumination of light coupled through Si-MRR at 1550nm wavelength. b) Performance of five different photodetector devices represented by responsivity measured at zero bias (0V), 1V, and 2V showing enhancement in magnitude due to improvement in photogenerated carrier collection under the influence of bias.

After compensating for coupling losses, we find an external responsivity (I_{photo}/P_{input}) of 10 mA/W and 468 mA/W at -2 V for devices 1 and 2, respectively. This responsivity is 1.75 times higher than that of a waveguide-integrated $MoTe_2$ detector tested at 1310 nm. The high responsivity of these $MoTe_2$ detectors operating at 1550 nm can be attributed to enhanced absorption resulting from strain engineering the decrease in bandgap and the photon lifetime enhancement of the MRR proportional to the cavity finesse (Fig. 4.2.5). The responsivity varies linearly with bias voltage, indicating a back-to-back (M-S-M) junction, and the device does not exhibit saturable absorption at the tested power levels (Fig. 4.2.4a). The external quantum efficiency (EQE) is determined by $EQE = R \times hc/q\lambda$,

where R, h, c, q, and λ represent the responsivity, Planck's constant, speed of light in vacuum, elementary electron charge, and operating wavelength, respectively. The EQEs are 1% and 37% at -2 V for devices 1 and 2, respectively [8].

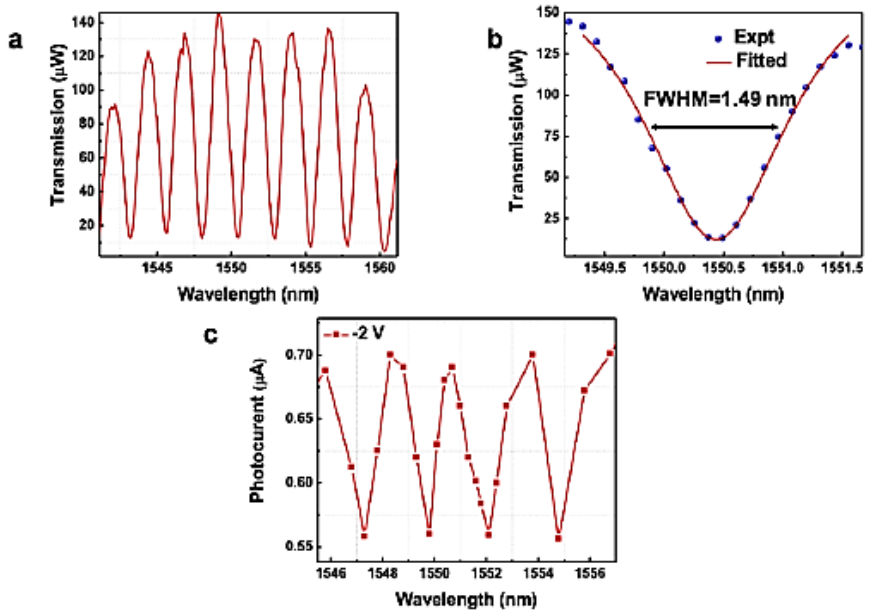

Figure 0.8 a) Transmission spectrum of a ring resonator after the transfer of ML MoTe2 flake showing the improvement of coupling efficiency. The free spectral range is found to be ~2.4 nm. b) Lorentzian Fitted plot of the resonance curve showing resonance at ~1550.5 nm with an FWHM of ~1.49 nm, which corresponds to a quality factor and finesse value of 1040 and 1.6, respectively. c) Spectral response of the photodetector over a broadband range showing maximum current at on resonance (~1550.5 nm) where the enhancement is limited by the low finesse value of the ring resonator.

The impact of the MRR on the detector's performance is considered. When operated at a fixed power of 120 μW and different bias voltages, the device exhibits approximately 50% enhanced photocurrent on the resonance compared to off-resonance, matching the finesse of the MRR (Fig. 4.2.6).

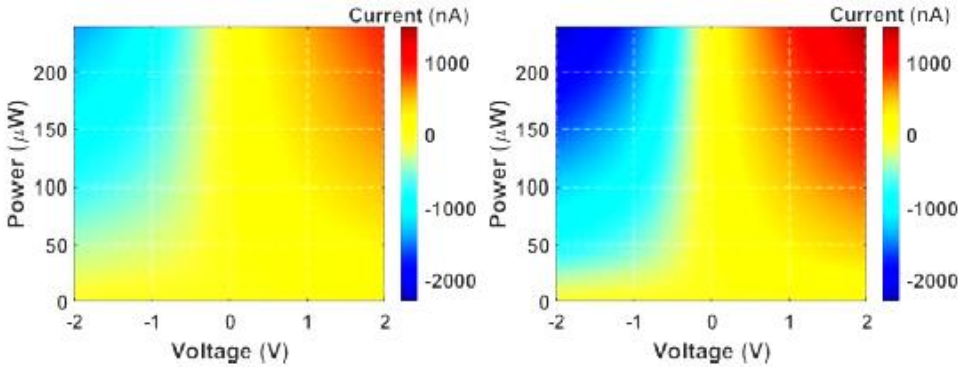

Figure 0.9 Measured photocurrent for a) off-resonance (1549.65 nm) and b) on-resonance (1550.75 nm), as a function of incident optical power and electrical bias voltages at room temperature. The photocurrent at resonance shows ~50% photocurrent enhancement as compared to the off-resonant condition. The cavity enhancement factor is governed by the finesse of the cavity resonator, which is ~1.6 in our case.

However, the MRR-integrated MoTe2 photodetector shows about a 1.2-fold enhancement of the photocurrent at 1550 nm (on-resonance) compared to the straight waveguide photodetector without planarization (Fig. 4.2.7).

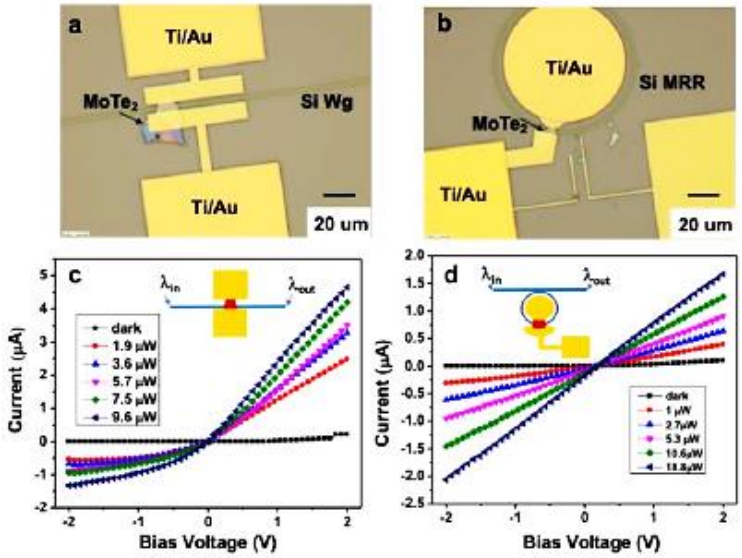

Figure 0.10 Optical microscope image of the device fabricated with MoTe2 on top of a) Si Waveguide, b) Si MRR. A few layers of $MoTe_2$ are transferred by using our developed 2D printer technique. Two metal electrodes (5/45 nm) contact the MoTe2 layer and conduct the generated photocurrent. Typical I-V characteristics of M-S-M diode showing asymmetry nature under dark and light conditions for c) straight waveguide and d) MRR. MRR-integrated PD shows enhanced responsivity resulting from the compact device.

Research findings from the community have observed strain-induced modulation of the electronic bandgap in 2D semiconductors wrapped around patterned substrates [20]. In our experiment, the enhanced photocurrent in the wrapped-around detector compared to the planarized control sample may have also benefited from induced strains (Fig. 4.2.8).

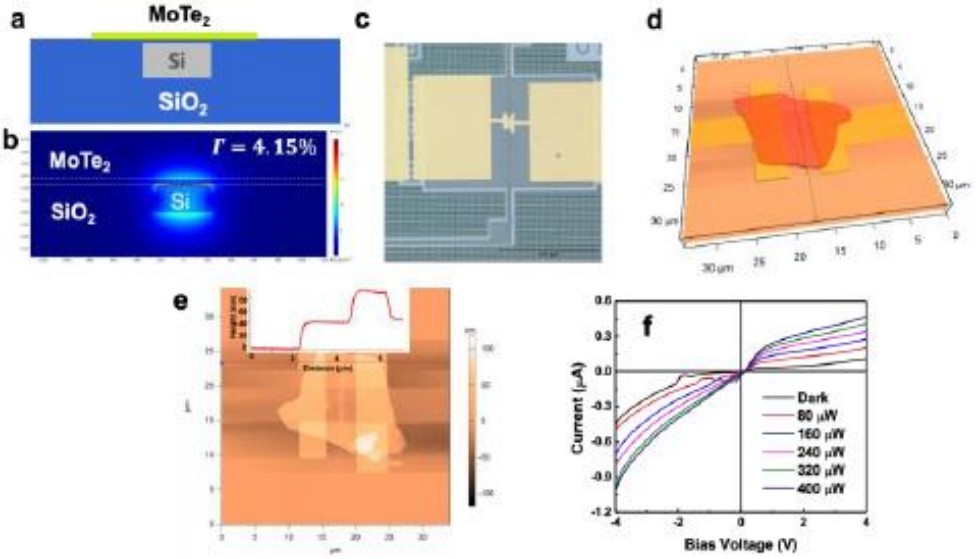

Figure 0.11 Photo response of a $MoTe_2$ photodetector on planarized waveguide a) Schematic cross-sectional diagram of relaxed ML $MoTe_2$ flake wrapped on top of a planarized waveguide. b) Simulated mode profile for $MoTe_2$ integrated planarized waveguide for TM mode where the mode overlap factor (Γ) is found to be 4.15%. c) Optical micrograph of the device (top view) where a few layers of $MoTe_2$ flakes are integrated on a planarized Si waveguide. d) 3D AFM topography showing the flat ML $MoTe_2$ flakes of thickness ~50 nm on top of a planarized waveguide (h=220 nm and w=500 nm). e) AFM micrograph (top view) showing height profile (along the red line). f) Typical I-V characteristics of M-S-M diode showing asymmetrical nature under different optical power.

Using first-principles density functional theory (DFT) calculations for monolayer $MoTe_2$, we found that the electronic gap experienced a red-shift with tensile strains, potentially aligning the electronic gap with the telecommunication wavelength (Fig. 4.2.9).

Higher tensile strains resulted in valence bands shifting towards higher energies (at Γ), while the conduction bands at the K- and H-points shifted towards lower energies and converged at the conduction band minimum with equal energies (Fig. 4.2.9c). As a result, the bandgap decreased from approximately 1.04 eV for the pristine material to about 0.8 eV for strained $MoTe_2$ (4%), while still maintaining an indirect bandgap semiconductor. In our case, the strain varies spatially, creating a graded bandgap rather than a uniform bandgap across the entire structure, resulting in a bandgap of 0.8 eV. Therefore, the bandgap (Eg) does not abruptly end at 0.8 eV. These findings suggest that tensile strain can enable inter-band optical transitions at the telecommunication frequency that are otherwise forbidden in the unstrained case.

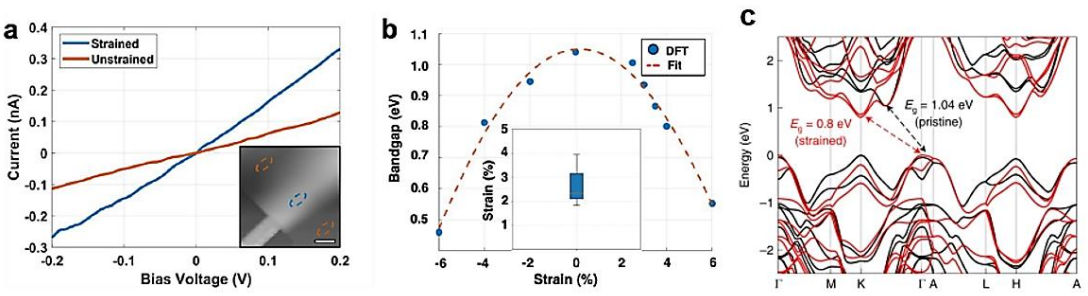

Figure 0.12 Strain-induced modulation of electrical conductivity. a) Local current-voltage (I-V) characteristics probed by CAFM. I-V curves for the two unstrained regions (away from the waveguide) are represented by the orange line, whereas the strained region (on top of the waveguide) is represented by the blue line (the inset shows the measurement locations), scale bar 1 um. The enhancement in the conductivity at a subthreshold regime suggests the presence of higher strain on top of the waveguide and its vicinity. b) DFT calculations of a few layers of 2H MoTe2

as a function of applied strain. The fit to the data (reduced chi-square) was used to extract the strain dispersive term $\partial Eg/\partial\varepsilon$ with a sum of sine functions (in this case, two). The amount of local strain on top of the waveguide can thence be estimated to be ~3±1% (inset). c) Bulk band-structure calculations obtained by DFT calculations of pristine (black) and 4% strained (red) MoTe2, showing a reduced bandgap. The valence band maximum is set to zero.

In devices operating in a photoconductive mode, shot noise typically dominates Johnson noise at high signal speeds. The NEP was found to be approximately 90 pW Hz^(-0.5), which is the lowest among the devices. The NEP gradually decreases with higher bias voltages, enabling low-light-level sensing, which can be further improved by forming a p-n junction (Fig. 4.2.10a).

To assess the dynamic response of the photodetector, we used a modulated laser input and measured the electrical output using a radio frequency microwave probe. The normalized frequency response was analyzed using the S_{21} parameter of a network analyzer (Fig. 4.2.10b). The photodetector device exhibited a 3 dB bandwidth of 35.6 MHz at 2 V. The response time of a cavity-integrated photodetector is primarily determined by three factors: the carrier transit time (τ_{tr}), the charge/discharge time of the junction capacitance (τ_{RC}), and the photon lifetime (τ_{cav}). The temporal response of the detector can be expressed as $\tau_R = \text{sqrt}\ (\tau_{tr}^2 + \tau_{RC}^2 + \tau_{cav}^2)$.

The transit time, τ_{tr} can be calculated using the equation $\tau_{tr} = l^2/2\mu V_{bias}$, where l is the channel length of the $MoTe_2$ detector and μ is the carrier mobility. In the top-gated

configuration with the 2D nanocrystal positioned atop the waveguide, the field-effect mobility was determined to be 1.2 cm^2/Vs. With a channel length of 0.8 μm, the transit time is estimated to be 3.2 ns, corresponding to a 3 dB bandwidth of approximately 49.7 MHz. This transit time is the main limiting factor in the temporal response of the device [8].

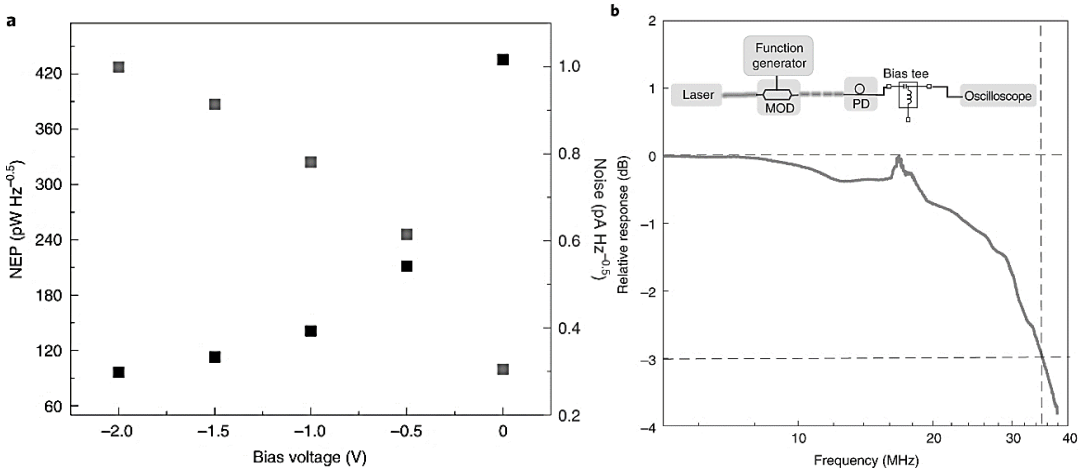

Figure 0.13 Dynamic performance a The device is operating in the photoconductive mode, showing a low dark current that leads to a low NEP value of 90 pW/$Hz^{-0.5}$ at 2 V. b, The alternating current photoresponse as a function of the modulated frequency of light signal showing a 3 dB cutoff frequency of 35 MHz, which is mainly limited by low transit time. The inset shows the dynamic response measurement setup. MOD and PD refer to the modulator and photodetector, respectively [8].

1.15.3 Method

Device Fabrication

The photonic integrated circuits, including the micro ring resonators (MRRs), were fabricated using silicon photonics. We utilized silicon on insulator (SOI) with an epitaxial Si layer of 220 nm and a buried oxide layer of 2 μm. Electron-beam lithography with a negative resist (ARN 7520) was employed for patterning the devices. Inductively coupled plasma etching was performed to transfer the patterns to the substrate. After etching, the photoresist mask was removed using acetone and short oxygen plasma cleaning. The samples were cleaned with acetone and isopropanol and dried using nitrogen gas. Heating on a hot plate at 180 °C for 2-3 minutes was applied to improve the adhesion of the $MoTe_2$ flakes. The few-layered MoTe2 flakes were then transferred onto the MRR using a 2D printer. A thin layer of polymethyl methacrylate (PMMA) with a thickness of approximately 300 nm was spin-coated on the sample and post-baked at 180 °C for 2 minutes. For electrical characterization, metal contact pads (80 × 80 μm^2) were patterned using electron-beam lithography. The samples were developed, and an oxygen plasma treatment was performed to clean the residues. Titanium (5 nm) and gold (45 nm) were deposited using electron beam evaporation, followed by lift-off in acetone. Fig. 4.2.11 provide further details of the fabrication process.

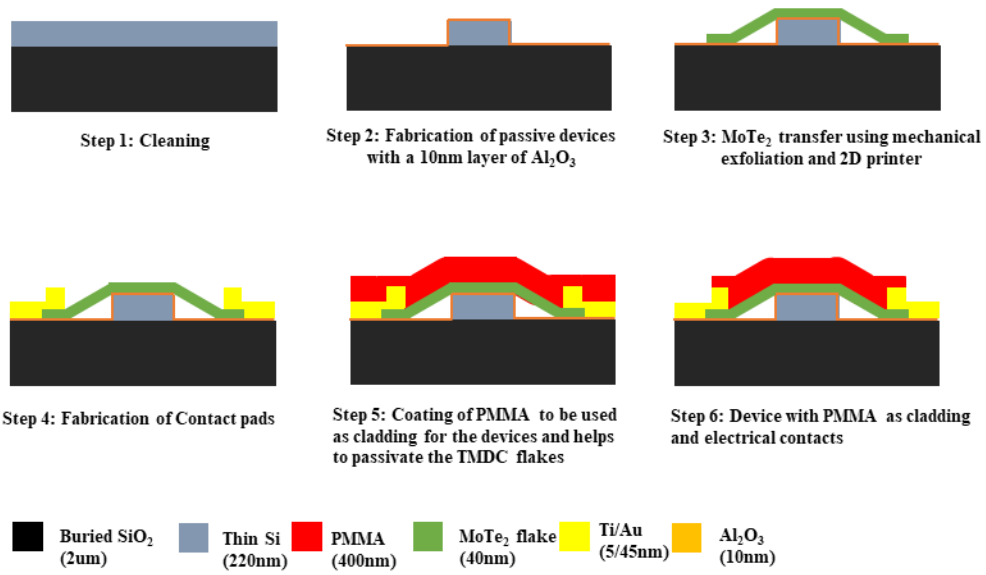

Figure 0.14 Fabrication process of Si MRR integrated $MoTe_2$ photodetector a) pre-cleaning of SOI substrate, b) Silicon photonic platform, which includes micro ring resonator, was fabricated using SOI substrate with a thin 220nm Si layer with 2 μm buried oxide. The devices were patterned using electron-beam lithography using a negative resist ARN 7520. The patterned features were further etched using an Inductively Coupled Plasma (ICP) etching tool. The photoresist mask was removed using acetone wash and short oxygen plasma cleaning. C) 10 nm of Al_2O_3 is deposited by atomic layer deposition (ALD) on a taped-out Si photonic chip to isolate the $MoTe_2$ flakes from Si; the sample is prebaked at 180^{o}C for 2 minutes to remove the surface moisture. Afterward, the exfoliated $MoTe_2$ flake is deterministically transferred on top of Si MRR by using 2DMTS. d) Ti (5 nm)/Au (45 nm) is deposited by an electron beam evaporator followed by a lift-off process. e) A uniform PMMA layer is used as a cladding layer to improve the light coupling efficiency, followed by f) opening of electrical contact pads for the electrical measurement by using one EBL step.

1.15.4 Conclusions

In summary, the researchers have successfully demonstrated a strain-induced absorption-enhanced 2D nanocrystal (MoTe2) based silicon photonic micro ring-integrated photodetector. The device exhibits high responsivity, with device 1 achieving 0.01 A/W and device 2 achieving approximately 0.5 A/W at a wavelength of 1550 nm. The detector also demonstrates a low noise-equivalent power (NEP) of 90 $pW/Hz^{0.5}$. By subjecting the MoTe2 nanocrystal to mechanical strain when wrapped around a non-planarized silicon waveguide, the researchers observe a shift in the bandgap towards 0.80 eV for the strained MoTe2. The strain is estimated to be around 3 ± 1% based on local changes in the work function mapped using Kelvin probe force microscopy (KPFM) and confirmed by density functional theory (DFT) calculations [8]. Furthermore, by utilizing a high-quality-factor (Q) cavity resonator, the responsivity of the device can be further improved. The photodetector demonstrates a 3 dB bandwidth of 35 MHz, with the response time primarily limited by the transit time of carriers. This strain-engineered bandgap allows for optical absorption at the telecom wavelength of 1550 nm, making this integrated photonic detector a promising component for future on-chip photonic circuits.

1.15.5 References

[1] R. S. Jacobsen *et al*, "Strained silicon as a new electro-optic material," *Nature*, vol. 441, *(7090)*, pp. 199-202, 2006. Available: http://dx.doi.org/10.1038/nature04706. DOI: 10.1038/nature04706.

[2] T. -. Cheng *et al*, "Strain-enhanced photoluminescence from Ge direct transition," *Applied Physics Letters*, vol. 96, *(21)*, pp. 211108-3, 2010. Available: http://dx.doi.org/10.1063/1.3429085. DOI: 10.1063/1.3429085.

[3] Anonymous "Thickness and strain effects on electronic structures of transition metal dichalcogenides: 2H-MX 2 semiconductors (M = Mo, W; X = S, Se, Te)," . DOI: 10.1103/physrevb.85.033305.

[4] M. Ghorbani-Asl *et al*, "Strain-dependent modulation of conductivity in single-layer transition-metal dichalcogenides," *Physical Review B*, vol. 87, *(23)*, 2013. Available: https://search.proquest.com/docview/2084272628. DOI: 10.1103/PhysRevB.87.235434.

[5] Apr 9,. 2013.

[6] A. Castellanos-Gomez *et al*, "Local Strain Engineering in Atomically Thin MoS2," *Nano Letters*, vol. 13, *(11)*, pp. 5361-5366, 2013. Available: http://dx.doi.org/10.1021/nl402875m. DOI: 10.1021/nl402875m.

[7] O. B. Aslan *et al*, "Probing the Optical Properties and Strain-Tuning of Ultrathin Mo1–xWxTe2," *Nano Letters*, vol. 18, *(4)*, pp. 2485-2491, 2018. Available: https://www.osti.gov/servlets/purl/1457055. DOI: 10.1021/acs.nanolett.8b00049.

[8] R. Maiti *et al*, "Strain-engineered high-responsivity MoTe2 photodetector for silicon photonic integrated circuits," *Nature Photonics*, vol. 14, *(9)*, pp. 578-584, 2020. Available: https://search.proquest.com/docview/2436973892. DOI: 10.1038/s41566-020-0647-4.

[9] P. Johari and V. B. Shenoy, "Tuning the Electronic Properties of Semiconducting Transition Metal Dichalcogenides by Applying Mechanical Strains," *ACS Nano*, vol. 6, *(6)*, pp. 5449-5456, 2012. Available: http://dx.doi.org/10.1021/nn301320r. DOI: 10.1021/nn301320r.

[10] D. H. Keum *et al*, "Bandgap opening in few-layered monoclinic MoTe2," *Nature Physics*, vol. 11, *(6)*, pp. 482-486, 2015. Available: https://search.proquest.com/docview/1684991750. DOI: 10.1038/nphys3314.

[11] R. Shiue *et al*, "High-Responsivity Graphene–Boron Nitride Photodetector and Autocorrelator in a Silicon Photonic Integrated Circuit," *Nano Letters*, vol. 15, *(11)*, pp. 7288-7293, 2015. Available: http://dx.doi.org/10.1021/acs.nanolett.5b02368. DOI: 10.1021/acs.nanolett.5b02368.

[12] X. Gan *et al*, "Chip-integrated ultrafast graphene photodetector with high responsivity," *Nature Photonics,* vol. 7, *(11),* pp. 883-887, 2013. Available: https://search.proquest.com/docview/2789112164. DOI: 10.1038/nphoton.2013.253.

[13] S. Schuler *et al*, "Controlled Generation of a p–n Junction in a Waveguide Integrated Graphene Photodetector," *Nano Letters,* vol. 16, *(11),* pp. 7107-7112, 2016. Available: http://dx.doi.org/10.1021/acs.nanolett.6b03374. DOI: 10.1021/acs.nanolett.6b03374.

[14] D. Kim *et al*, "Two-dimensional phase-engineered 1T′– and 2H–MoTe2-based near-infrared photodetectors with ultra-fast response," *Journal of Alloys and Compounds,* vol. 789, pp. 960-965, 2019. Available: https://dx.doi.org/10.1016/j.jallcom.2019.03.121. DOI: 10.1016/j.jallcom.2019.03.121.

[15] Y. Bie *et al*, "A MoTe 2 -based light-emitting diode and photodetector for silicon photonic integrated circuits," *Nature Nanotechnology,* vol. 12, *(12),* pp. 1124, 2017. Available: https://www.ncbi.nlm.nih.gov/pubmed/29209014.

[16] P. Ma *et al*, "Fast MoTe2 Waveguide Photodetector with High Sensitivity at Telecommunication Wavelengths," *ACS Photonics,* vol. 5, *(5),* pp. 1846-1852, 2018. Available: http://dx.doi.org/10.1021/acsphotonics.8b00068. DOI: 10.1021/acsphotonics.8b00068.

[17] H. Huang *et al*, "Ferroelectric polymer tuned two dimensional layered MoTe2 photodetector," *RSC Advances,* vol. 6, *(90),* pp. 87416-87421, 2016. Available: https://search.proquest.com/docview/1845802293. DOI: 10.1039/c6ra18238k.

[18] T. J. Octon *et al*, "Fast High-Responsivity Few-Layer MoTe2 Photodetectors," *Advanced Optical Materials,* vol. 4, *(11),* pp. 1750-1754, 2016. Available: https://api.istex.fr/ark:/67375/WNG-3238P5CX-8/fulltext.pdf. DOI: 10.1002/adom.201600290.

[19] H. Huang *et al*, "Highly sensitive visible to infrared MoTe2 photodetectors enhanced by the photogating effect," *Nano,* vol. 27, *(44),* pp. 445201, 2016. Available: https://iopscience.iop.org/article/10.1088/0957-4484/27/44/445201. DOI: 10.1088/0957-4484/27/44/445201.

[20] H. Li *et al*, "Optoelectronic crystal of artificial atoms in strain-textured molybdenum disulphide," *Nature Communications,* vol. 6, pp. 8080, 2015. Available: https://search.proquest.com/docview/1701901020. DOI: 10.1038/ncomms9080.

1.16 Exciton Strain Engineering in Monolayer TMDCs using Strain Engineering

1.16.1 Introduction

Two-dimensional transition metal dichalcogenides exhibit unique electrical, optical, mechanical, and quantum properties paving new ways toward building optoelectronic applications. The semiconducting nature of transition metal dichalcogenides (TMDCs) allows us to exploit the presence of bandgap for strong optical absorption using thin layers of these materials towards ultra-thin integrated devices. The exciton wavelengths of

TMDCs are spread from visible to near-infrared spectrum when mono to few layers' materials is used. The strong excitonic absorption in these ultra-thin materials can be harvested for designing sensors. When focusing on performance in the visible spectrum, the silicon nitride photonic platform is a great advantage concerning silicon photonic platform due to the opacity of the latter one (1.1 eV bandgap) [1]. Here I performed an extensive study on nonintegrated WS_2 photodetectors and integrated WS_2 photodetectors [2], [3]. Also, it has been demonstrated that the exciton bandgap in TMDCs can be shifted and tuned as an effect of strain. It has been experimentally demonstrated that strain is induced in TMDCs integration on photonic circuits due to the structural profile owing to bandgap tuning [4], [5]. Here, we demonstrate the study on the effect of strain introduced in tungsten disulfide (WS_2) due to heterogeneous integration on silicon nitride waveguide leading to shifting in exciton absorption (1.95 - 1.98 eV) using a photodetector device.

1.16.2 Results and Discussion

Here, I have fabricated a monolayer WS_2 integrated photodetector on silicon nitride waveguides. The photonic waveguides and focused beam grating coupler were designed, optimized, and fabricated for a broad range (580 nm - 640 nm) of operation around the exciton wavelength of WS_2. The height profile of the box waveguides was ~215 nm where focused beam grating couplers were used for optical coupling through it as can be seen in the schematic in Fig. 4.3.1a. The chemical vapor deposition (CVD) technique was used to

grow WS_2 on SiO_2/Si substrate. The monolayer flakes (WS_2) after growth on the substrate were spin coating with a photoresist and transferred on the waveguides using the wet etch technique as mentioned in Chapter 3.1. Two probe terminal designs were used for optoelectrical measurements of the device.

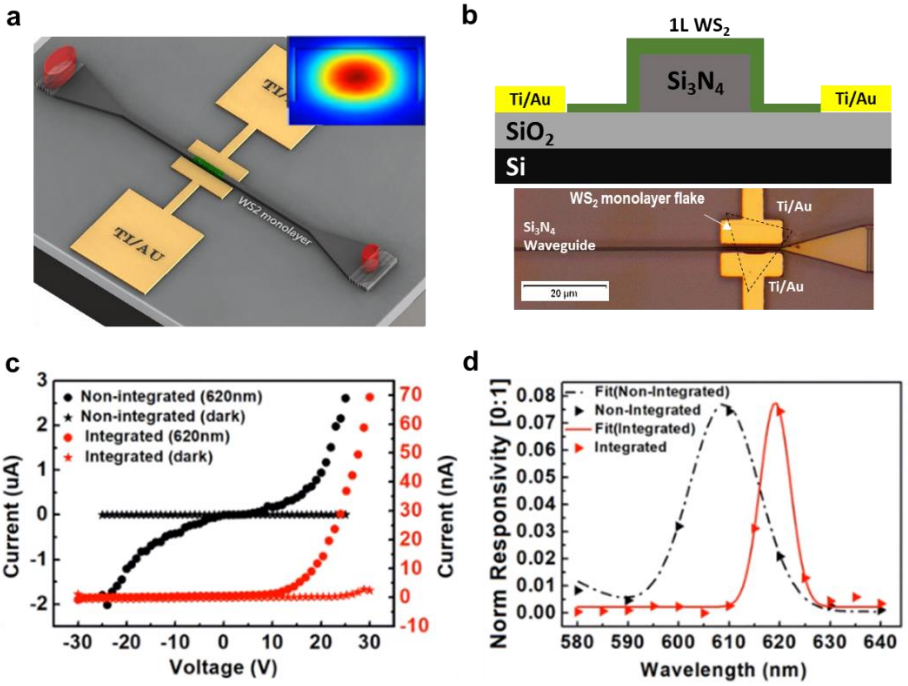

Figure 0.15 (a) Schematic illustration of integrated photodetector on SiN waveguide (410*215 nm). Eigenmode analysis of the waveguide after depositing WS_2 monolayer in the inset. (b) Cross-section schematic and microscope image of the device with electrical contact. (c) I-V characteristics under dark and illumination conditions of the non-integrated and integrated device, later represented in Fig. 4.3.1a. (d) Normalized responsivity spectral response of both non-integrated and integrated photodetector showing a peak shift of ~10nm resembling PL emission of monolayer WS2 as in Fig. 4.3.2a.

A free space Gaussian beam was shinned on the gratings as input and output transmission was detected using a CCD camera. To understand device functionality under unstrained conditions, we also fabricated non-integrated (free space) photodetectors on SiO_2 substrate and tested using vertical/top illumination of light for photocurrent behavior.

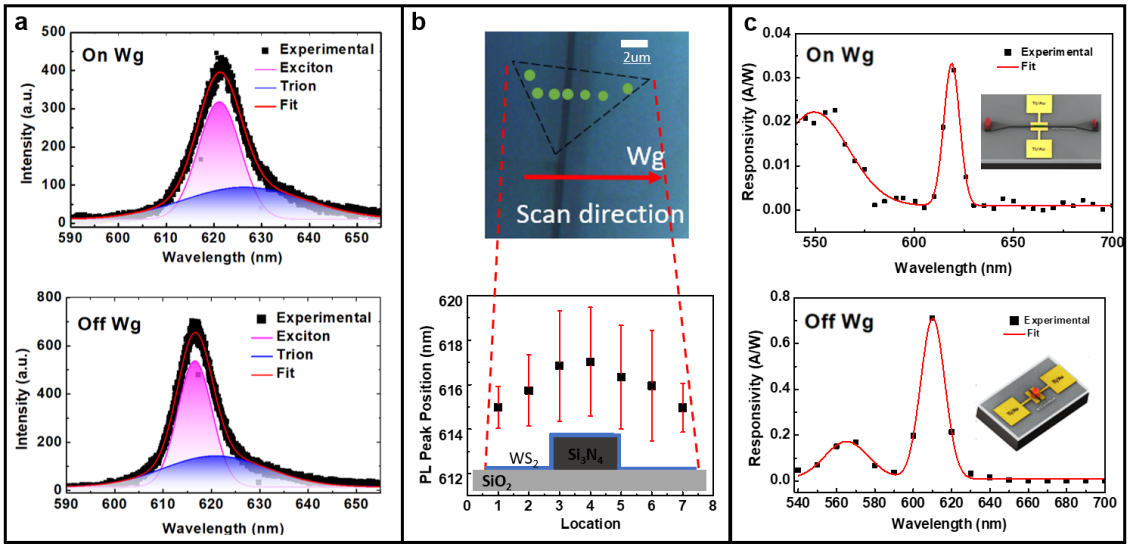

Figure 0.16 (a) Photoluminescence spectra showing redshift in both excitons and trions peak due to strain induced in WS_2 flake after integrating on top of a SiN waveguide. The peak position of exciton and trion was calculated after fitting the experimental photoluminescence spectra acquired with 532 nm excitation laser (b) Localized strain mapping using photoluminescence showing the gradual change in the exciton peak position over the SiN waveguide. The vertical bars in the graph represent the range of variation in peak position at each spot as shown in the microscope image above for multiple devices (c) Spectral response of strained (integrated on waveguide) and non-integrated (unstrained free space) photodetector device showing the shift in the maximum

absorption peak due to shift in exciton wavelength. The inset in both graphs shows the device structure schematic.

The integrated and non-integrated photodetectors were tested with a sweep of electrical bias at room temperature (~300K). Due to the high Schottky barrier between the metal-semiconductor junctions on both contacts, we observed considerable contact resistance leading to high bias voltage for the collection of photo-generated carriers. For both the integrated and nonintegrated devices the current-voltage characteristics were observed for the photo-current measurement as shown in Fig. 4.3.1c. The responsivity (R) was computed using the formula $R(\lambda)=I_{ph}/P_{in}$, where I_{ph} is the measured photocurrent after applying bias and P_{in} is the input power coupled inside the waveguide after normalizing grating coupler losses and laser spectral response. The variation in spectral responsivities can be seen in Fig. 4.3.1d for both the nonintegrated and the integrated photodetectors. High responsivities are achieved at the exciton wavelength region (as seen in Fig. 4.3.2c due to strong photon absorption in both cases. Raman spectroscopy was performed to observe the change in a spectral shift at active E12g mode indicating the in-plane lattice vibration. A shift of 1.52cm-1 was observed at peak-to-peak positions which indicated a change in the in-plane lattice vibration indicating strain induced in the material while wrapping around the waveguide. The result shows a similar trend as discussed in [5], [6] as an effect of the strain. The exciton peak position was mapped using photoluminescence (PL) spectroscopy. As seen in Fig. 4.3.1a, the exciton peak position is represented with the

exciton and trion peak fitting analysis. An exciton peak shift of 2.67 nm and trion shift of 2.59 nm was observed as an effect of strain in both cases, also studied by [10]-[12]. The shift in PL and Raman spectroscopy observed is an average effect of the area under illumination as the device is smaller than the beam spot size and is diffraction-limited in the case of an integrated device.

1.16.3 Method

Photonic devices were fabricated using silicon nitride wafers with SiN/SiO2 (220 nm/2 μm) layers grown by plasma-enhanced chemical vapor deposition (PECVD). The thick SiO_2 helps to isolate the device from the Si substrate. After spin coating, ~400nm thick negative photoresist the device design structure was patterned on the wafer using electron beam lithography, followed by dry etching with CHF_3/O_2 after developing the sample. The polymer was then removed using acetone. To remove any photoresist residues the sample was cleaned using O_2 plasma for 3 mins. The photonic devices were designed for broadband transmission to study the effect of wavelength from 520 nm to 700 nm. The dimensions of the photonic platform were observed under scanning electron microscopy (SEM) and atomic force microscopy (AFM) while the cross-section of the waveguides was observed under a focused ion beam (FIB) as shown in Figure (1) in SOM. The width of the waveguide was for single mode transmission of light using COMSOL Multi-Physics mode analysis for the spatial distribution of the electric field as shown in figure (2) in SOM. The

monolayer WS_2 flakes were transferred on the device using the wet etching technique as discussed in Chapter 3.1. The thickness of the mono-layer flakes was measured and confirmed using atomic force microscopy (AFM) and photoluminescence (PL) measurements. After the transfer of monolayer WS_2 flakes, the sample was kept under a vacuum (10^{-7}) for 12 hours to enhance the adhesion of the flakes with the devices. The sample was further coated with a positive photoresist (PMMA A4) and patterned using an electron beam lithography process to create contacts. A 5nm of Ti and 45 nm of Au were deposited on the patterned sample using an electron beam evaporation technique followed by a lift-off process using acetone.

Opto-electronic Measurements Setup

The electrical biasing and photo-current measurements were performed using Keithley 2400 source meter. The SuperK COMPACT super-continuum laser source was used as a broadband laser source. The light is guided to the sample using mirrors passing through a beam splitter BS1 and focused on the sample through a 50X objective. The sample is mounted on a 3-axis stage for positioning the device under the spot and adjusting the sample at the focal length of the beam. The measurement setup block diagram is shown in Fig. 4.3.3. The light output from the sample and reflection from the surface of the substrate is captured back through the objective and passed through another beam splitter BS2 guiding the light towards the CCD camera. All the measurements are performed under room temperature and atmospheric pressure conditions.

1.16.4 Conclusion

The work experimentally demonstrated that high spectral responsivities at the exciton wavelength of WS2 can be achieved in heterogeneously integrated photodetectors towards building ultra-thin optoelectronic devices. As a result of heterogeneous integration, the effect of the introduced strain on the shift in exciton absorption wavelength was observed at ~10nm as compared to the non-integrated devices. This work is showing a pathway for future on-chip photonic heterogeneous integrated devices at a visible wavelength for applications in the field of strainoptronics.

1.16.5 References

[1] R. Baets *et al*, "Silicon photonics: Silicon nitride versus silicon-on-insulator," in Mar 2016, pp. 1-3.

[2] F. Peyskens *et al*, "Integration of single photon emitters in 2D layered materials with a silicon nitride photonic chip," *Nature Communications*, vol. 10, *(1)*, pp. 4435-7, 2019. Available: https://www.ncbi.nlm.nih.gov/pubmed/31570712. DOI: 10.1038/s41467-019-12421-0.

[3] C. Zhang *et al*, "High-performance photodetectors for visible and near-infrared lights based on individual WS2 nanotubes," *Applied Physics Letters*, 2012. Available: https://explore.openaire.eu/search/publication?articleId=dedup_wf_001::b83eb063d716f80e1eb0e67d9da5c3df. DOI: 10.1063/1.4729144.

[4] R. Maiti *et al*, "Strain-engineered high-responsivity MoTe2 photodetector for silicon photonic integrated circuits," *Nature Photonics*, vol. 14, *(9)*, pp. 578-584, 2020. Available: https://search.proquest.com/docview/2436973892. DOI: 10.1038/s41566-020-0647-4.

[5] Y. Wang *et al*, "Strain-induced direct-indirect bandgap transition and phonon modulation in monolayer WS sub(2)," *Nano Research*, vol. 8, *(8)*, pp. 2562-2572, 2015. Available: https://search.proquest.com/docview/1744704571. DOI: 10.1007/s12274-015-0762-6.

1.17 Strain effect on WSe_2 bandgap Stretched on Nanostructures

1.17.1 Fabrication and Spectroscopic Analysis

Atomically stacked 2D materials, held together by van der Waals (vDW) forces, exhibit unique properties and can be modulated using mechanical forces. WSe_2, for instance, demonstrates tunability in photoluminescence (PL) enhancement, bandgap, quantum emission, and optical absorption through the application of strain [1]-[3]. In this study, I investigate the strain effects on WSe_2 multilayers using triangular geometric pillars. These pillars are etched from a SiN substrate, with a height of 220 nm, and are equally spaced to allow parts of the flake to slack in between the pillars, as well as remain suspended in certain areas (Fig. 4.1.1a). Fig. 4.1.1b(I) and 4.1.1b(II) show microscope images of the

nanopillars after the etching process and after transferring a large WSe_2 flake onto the same area using the proposed transfer system, respectively.

By suspending the flake like a membrane on multiple nanopillars, a high strain gradient is generated along the pillar area. The triangular shape of the nanopillars further enhances the strain in the membrane. To investigate the induced strain, we performed spatial mapping of photoluminescence and Raman spectroscopy. The Raman active modes of WSe_2 are depicted in Fig. 4.1.1c. The PL spectra were analyzed by fitting the data to identify significant peak positions, as shown in Fig. 4.1.1d. These peak positions were used to perform PL map analysis and investigate the strain effects. Overall, this experimental setup enables the study of strain-induced effects on WSe_2 multilayers, providing insights into their optical properties, such as photoluminescence enhancement and Raman spectroscopy responses.

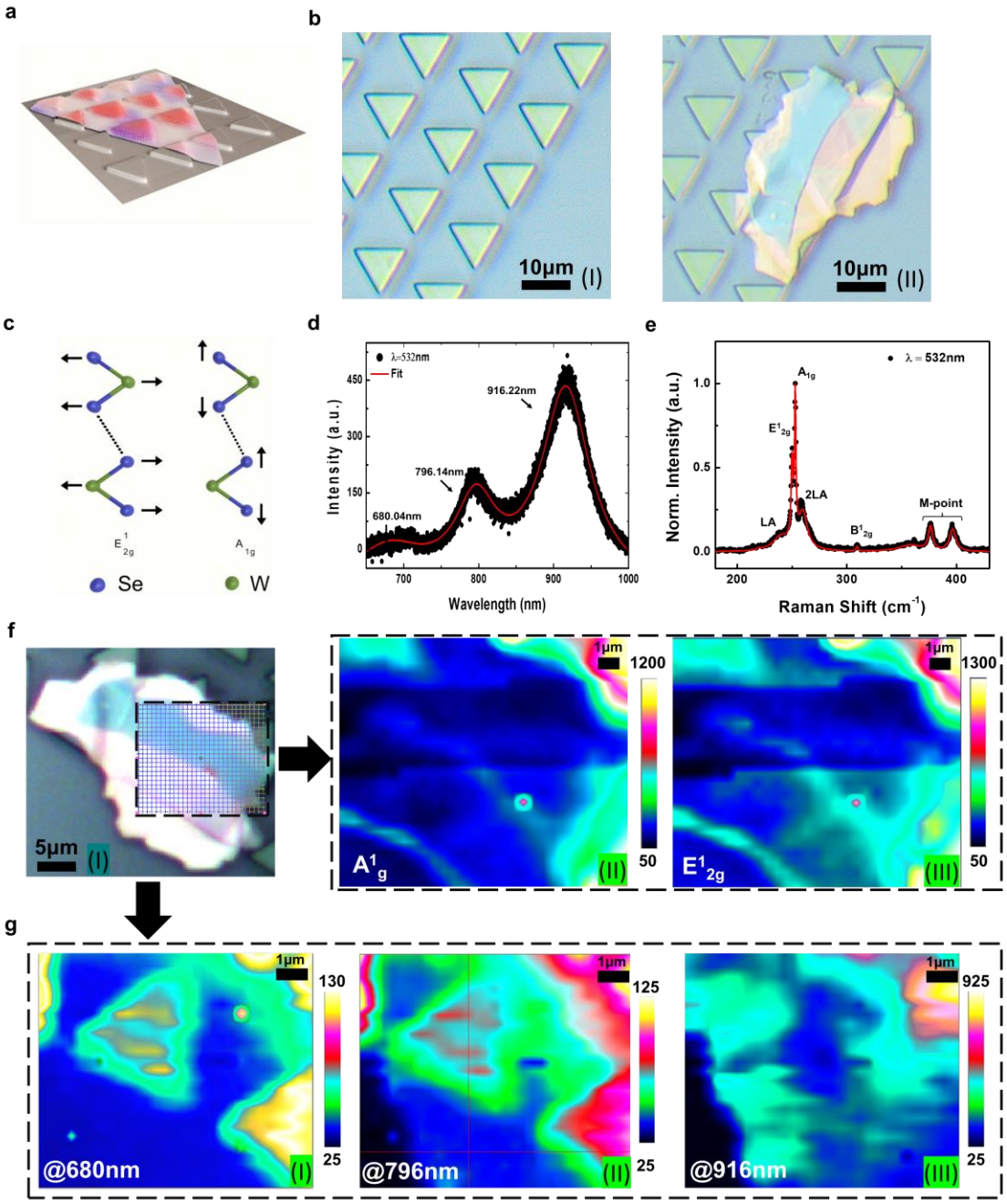

Figure 0.17 Strain-induced in multilayer WSe_2 using triangular nanopillars. (a) Schematic representation of strained multilayer WSe_2 membrane on triangular nanopillars. (b) Optical microscope images for (I) SiN triangular nanopillar structures (II) WSe_2 membrane (after transfer) using the 2D printer setup on the nanopillars. (c) Schematic representation of $E^{12}{}_g$ and $A^1{}_g$ Raman

active modes of WSe_2. (d) PL spectra of WSe_2 membrane showing the fitted curve highlighting the significant active peaks. (e) Raman spectra showing the active modes ($\lambda_{excitation}$= 532 nm). (f) Optical image of mapping area highlighted with the grid selection for Raman and PL mapping points (I), Raman intensity map for the strained area of the WSe_2 membrane at A^1_g mode (II), and E^{12}_g mode (III). (g) PL mapping was realized at significant PL peaks for WSe_2 at 680 nm, 796 nm, and 916 nm showing intensity enhancement for 680 nm and 796 nm peak positions while a reduction in intensity at the 916 nm peak position.

Bulk WSe_2 exhibits crystal lattice vibrations with Raman active modes, including A1g, E^1_g, and E^2_g [4] (Fig. 4.1.1e). In Raman tensor analysis, circularly polarized helicity configurations are employed to study the E-modes and A-modes [5]. In the LR configuration (left circular polarization incident and right circular polarization signal collected), a consistent peak at 247.4 cm^{-1} is observed, corresponding to the E^{12}_g mode. In the LL configuration (left circular polarization incident and left circular polarization signal collected), a peak at 249.5 cm^{-1} is observed, corresponding to the A^1_g mode (Fig. 4.1.1e).

To investigate the effect of strain on the crystal lattice, Raman mapping was performed. Fig. 4.1.1f(I) shows a selected area on top of a few pillars with a grid representing the mapping density used during the measurements. The strain induces variations in the physical atomic arrangement, leading to changes in the vibrational modes of the material [1], [3]. Fig. 4.1.1f depicts the Raman mapping profile of the WSe_2 membrane strained on the pillars, showing an intensity change of almost three times compared to the unstrained

region for both the A^1_g mode (II) and E^{12}_g mode (III). The intensity variation also reveals the curved surface profile of the membrane on the pillars and the impact of strain on the peak intensity.

To explore the optical response of the strained material, photoluminescence spectroscopy was conducted. The intensity enhancement at the significant peaks observed in Fig. 4.1.1d was examined. Photoluminescence spectra mapping was performed at 680 nm, 796 nm, and 916 nm for WSe_2 to understand the effect of strain on each peak. Fig. 4.1.1g displays the intensity map of photoluminescence for the strained region on one of the pillars at each significant peak. An enhancement of approximately 4.5x and 3x was observed at the 680 nm (I) and 796 nm (II) peak positions, respectively. However, a reduction in the intensity of about 2.7x was observed at the 916 nm peak (III). The selective tuning of WSe_2's photoluminescence response can be harnessed for the design of optical filters or spectral selective absorbers integrated into photonic circuits [6], [7]. These studies contribute to a better understanding of material properties, facilitating the design and fabrication of devices for various applications in diverse fields.

1.17.2 References

[1] L. N. Tripathi *et al*, "Spontaneous Emission Enhancement in Strain-Induced WSe2 Monolayer-Based Quantum Light Sources on Metallic Surfaces," *ACS Photonics*, vol. 5,

(5), pp. 1919-1926, 2018. Available: http://dx.doi.org/10.1021/acsphotonics.7b01053. DOI: 10.1021/acsphotonics.7b01053.

[2] S. B. Desai *et al*, "Strain-Induced Indirect to Direct Bandgap Transition in Multilayer WSe2," *Nano Letters,* vol. 14, *(8),* pp. 4592-4597, 2014. Available: http://dx.doi.org/10.1021/nl501638a. DOI: 10.1021/nl501638a.

[3] B. Amin, T. P. Kaloni and U. Schwingenschlögl, "Strain engineering of WS 2 , WSe 2 , and WTe 2," *RSC Advances,* vol. 4, *(65),* pp. 34561, 2014. . DOI: 10.1039/C4RA06378C.

[4] X. Zhang *et al*, "Phonon and Raman scattering of two-dimensional transition metal dichalcogenides from monolayer, multilayer to bulk material," *Chemical Society Reviews,* vol. 44, *(9),* pp. 2757-2785, 2015. Available: https://www.ncbi.nlm.nih.gov/pubmed/25679474. DOI: 10.1039/c4cs00282b.

[5] S. Chen *et al*, "Helicity-Resolved Raman Scattering of MoS2, MoSe2, WS2, and WSe2 Atomic Layers," *Nano Letters,* vol. 15, *(4),* pp. 2526-2532, 2015. Available: http://dx.doi.org/10.1021/acs.nanolett.5b00092. DOI: 10.1021/acs.nanolett.5b00092.

[6] D. Zambrano *et al*, "Spin and Valley Filter Based on Two-Dimensional W Se 2 Heterostructures," *Physical Review Applied,* vol. 15, *(3),* 2021. . DOI: 10.1103/PhysRevApplied.15.034069.

[7] K. Lin *et al*, "Twist-angle engineering of excitonic quantum interference and optical nonlinearities in stacked 2D semiconductors," *Nature Communications,* vol. 12, *(1),* pp.

1553, 2021. Available: https://www.ncbi.nlm.nih.gov/pubmed/33692339. DOI: 10.1038/s41467-021-21547-z.

1.18 2D Material Characterization and Heterojunction Based Photonic Devices

1.18.1 Electrical Characterization of 2D Materials post-2DMTS Integration

Extensive studies have been conducted on the electrical properties of 2D materials, highlighting the impact of impurities, trapped contaminants, and defects that may arise during the material transfer or post-processing stages [1]-[3]. It is crucial to investigate the electrical properties of the material after contact formation to optimize device performance, as demonstrated in previous studies [4]-[6]. However, achieving consistent and reliable results for such devices using other transfer methods discussed earlier can be challenging. To demonstrate the consistent quality of flakes transferred using the proposed system, I performed transmission line measurements to determine the sheet resistance. The obtained results were normalized by the flaking area to mitigate the influence of flake shape and size on resistance measurements. For accurate measurements, only flakes with uniform thickness surfaces were selected, which were confirmed by Raman spectroscopy before forming the contact pads.

In Fig. 4.5.1a (inset microscope image), MoS_2 flakes were transferred onto a SiO_2 substrate, and contacts were created with varying gage lengths ranging from 0.5 μm to 3.5 μm, with a step size of 0.5 μm. This type of electrical characterization aids in the design of next-

generation devices to enhance optoelectronic performance [7], [8]. Fig. 4.5.1a illustrates the variation in sheet resistance with different gage lengths on the same flake, representing the sheet resistance behavior. To assess repeatability and consistency in achieving similar electrical properties, multiple flakes were transferred onto SiO_2 substrates, resulting in the fabrication of 18 devices. As shown in Fig. 4.5.1b, these devices exhibited consistent contact resistance ($R_C \sim <50$ kΩ) and sheet resistance ($R_S \sim <10$ kΩ/sq) for the MoS_2 flake. This demonstrates the reproducibility of electrical characterizations, which is crucial for developing electro-optic devices, magnetostatic devices, and stretchable electronic devices [8]-[10].

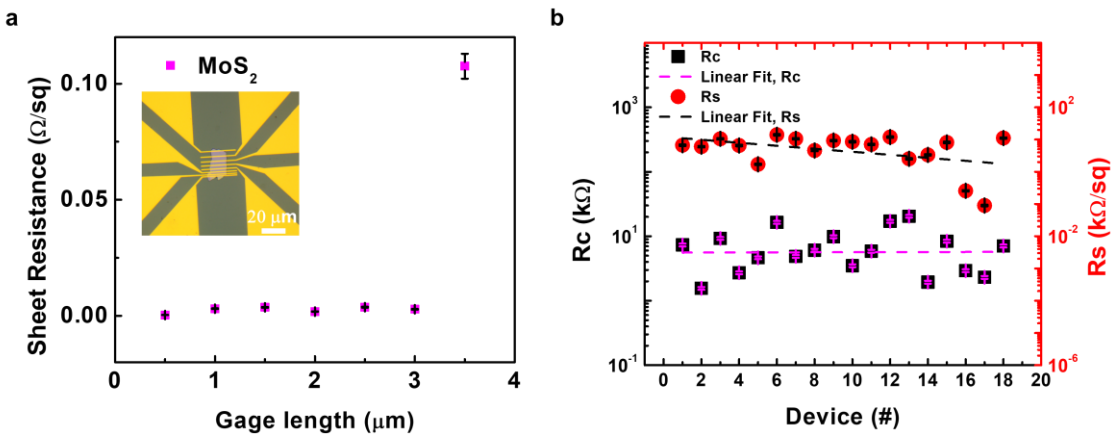

Figure 0.18 Electronic resistivity test of 2D flakes transferred with 2DMTS. (a) 2-terminal resistance measurement of individual MoS_2 flakes represented in the microscope image was performed to determine the gage length-based sheet resistance of the material for electrical characterization. A microscope image of the device in the inset of MoS_2 flake transferred on SiO_2 substrate after designing the contacts for various gage lengths. (b) Comparative study for achieving

repeatable electrical properties can be observed in the form of contact resistance (R_C ~ <50kΩ) and sheet resistance (R_S ~ <10kΩ/sq) for 18 devices.

1.18.2 Building 2D material Heterostructures

The assembly of multiple 2D crystals into vertical stacks provides a vast range of possibilities for exploring the diverse properties exhibited by these materials. These heterostructures, held together by vdW forces, offer a greater variety of combinations compared to traditional material stacking processes. As the family of 2D crystals continues to expand, the complexity of heterostructures that can be constructed with atomic precision also increases [11]-[13]. These 2D heterostructures hold great potential for electronic or electro-optic devices, superlattices, and quantum applications.

In this demonstration, we showcase the construction of a MoS_2/WSe_2 heterojunction using the proposed 2D transfer system. This small example highlights the combination of the unique properties of MoS_2 and WSe_2 by forming a junction through a heterostructure. Both MoS_2 and WSe_2 flakes are transferred onto a SiO_2 substrate to form the heterojunction, as depicted in Figure 10a. The inset in Figure 4.5.2a shows a dark field microscope image of the heterostructure, confirming the clean surface of the flakes and substrate. By experimentally analyzing the distinctive material signatures exhibited through Raman spectroscopy, we observe the combined effect of both materials in the heterostructure. Figure 4.5.2b displays the Raman spectra of individual MoS_2 and WSe_2 flakes, each

showing their respective active mode peaks. The Raman spectra of the MoS_2/WSe_2 heterojunction exhibit the combined Raman active modes of both materials. The location for detecting the Raman signal is marked on the optical image in Fig. 4.5.2a. The data were corrected for background signals and baseline noise to remove unwanted interference in the signal. This example demonstrates the capability of the setup to realize heterostructure formation for various applications. While not discussed here, the setup also allows for controlling the twist angle between layered stacks, enabling applications in twistronics and superlattices.

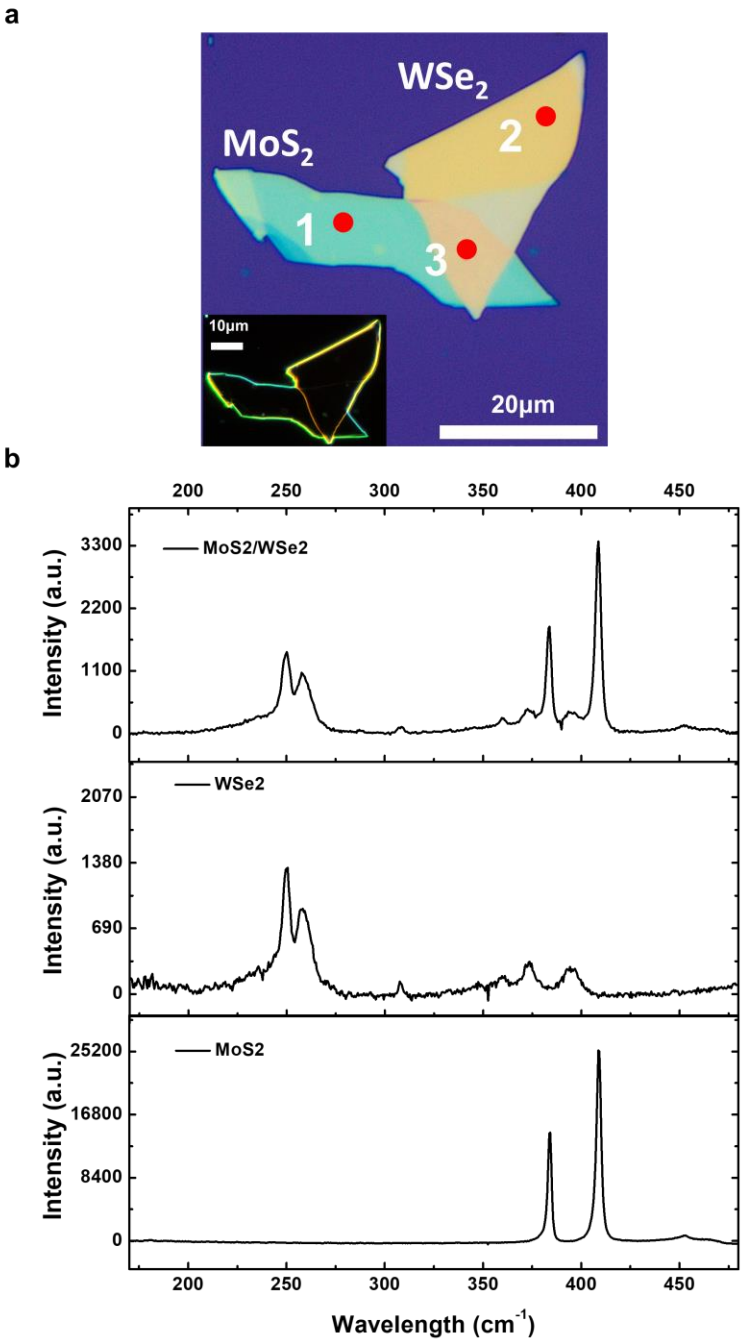

Figure 0.19 MoS_2 and WSe_2 multilayer heterostructure. (a) Optical microscope image of MoS_2/WSe_2 heterostructure built on SiO_2 substrate. The inset shows the dark field microscopy image of the heterostructure indicating no residues on the surface of the materials and substrate. (b)

Raman spectra for MoS_2, WSe_2, and MoS_2/WSe_2 heterostructure show the combined Raman signature of MoS_2 and WSe_2 at the junction formed by them.

1.18.3 References

[1] R. Addou, L. Colombo and R. M. Wallace, "Surface Defects on Natural MoS2," *ACS Applied Materials & Interfaces*, vol. 7, *(22)*, pp. 11921-11929, 2015. Available: http://dx.doi.org/10.1021/acsami.5b01778. DOI: 10.1021/acsami.5b01778.

[2] J. Sun *et al*, "Impact of Impurities on the Electrical Conduction of Anisotropic Two-Dimensional Materials," *Physical Review Applied*, vol. 13, *(4)*, 2020. . DOI: 10.1103/PhysRevApplied.13.044063.

[3] S. Kang *et al*, "2D semiconducting materials for electronic and optoelectronic applications: potential and challenge," *2d Materials*, vol. 7, *(2)*, pp. 22003, 2020. . DOI: 10.1088/2053-1583/ab6267.

[4] Y. Mao *et al*, "Observation of trap-related phenomena in electrical performance of back-gated MoS2 field-effect transistors," *Sst*, vol. 35, *(9)*, 2020. Available: https://iopscience.iop.org/article/10.1088/1361-6641/ab9d34. DOI: 10.1088/1361-6641/ab9d34.

[5] C. Hsiao-Yu, Zhu Weinan and Akinwande Deji, "On the mobility and contact resistance evaluation for transistors based on MoS2 or two-dimensional semiconducting

atomic crystals," *Applied Physics Letters,* vol. 104, *(11),* 2014. Available: https://search.proquest.com/docview/2127689545. DOI: 10.1063/1.4868536.

[6] H. Liu *et al,* "Fundamentals in MoS 2 Transistors: Dielectric, Scaling and Metal Contacts," *Meeting Abstracts (Electrochemical Society),* vol. MA2013-02, *(31),* pp. 2163, 2013. . DOI: 10.1149/MA2013-02/31/2163.

[7] A. Pacheco-Sanchez and D. Jimenez, "A contact resistance extraction method of 2D-FET technologies without test structures," in Jun 9, 2021, pp. 19-22.

[8] I. P. Handayani *et al,* "Optical and electrical characterization of WS2 multilayer on flexible PET substrate," *Mrx,* vol. 8, *(2),* 2021. Available: https://iopscience.iop.org/article/10.1088/2053-1591/abe54f. DOI: 10.1088/2053-1591/abe54f.

[9] T. Dong, J. Simões and Z. Yang, "Flexible Photodetector Based on 2D Materials: Processing, Architectures, and Applications," *Advanced Materials Interfaces,* vol. 7, *(4),* pp. 1901657-n/a, 2020. Available: https://onlinelibrary.wiley.com/doi/abs/10.1002/admi.201901657. DOI: 10.1002/admi.201901657.

[10] M. Long *et al,* "Progress, Challenges, and Opportunities for 2D Material Based Photodetectors," *Advanced Functional Materials,* vol. 29, *(19),* pp. 1803807-n/a, 2019. Available: https://onlinelibrary.wiley.com/doi/abs/10.1002/adfm.201803807. DOI: 10.1002/adfm.201803807.

[11] Y. Cho, J. Huang and C. W. Wong, "Collective excitations in 2D atomic layers: Recent perspectives," *Applied Physics Letters,* vol. 116, *(2),* pp. 20501, 2020. Available: http://dx.doi.org/10.1063/1.5135301. DOI: 10.1063/1.5135301.

[12] Y. Liu *et al*, "Van der Waals heterostructures and devices," *Nature Reviews. Materials,* vol. 1, *(9),* 2016. . DOI: 10.1038/natrevmats.2016.42.

[13] L. Britnell *et al*, "Field-Effect Tunneling Transistor Based on Vertical Graphene Heterostructures," *Science,* vol. 335, *(6071),* pp. 947-950, 2012. Available: https://www.jstor.org/stable/41508114. DOI: 10.1126/science.1218461.

1.19 Self-Driven Indium Selenide Heterojunction based Photonic Devices

1.19.1 Introduction

Two-dimensional (2D) semiconducting materials have attracted significant interest as promising photodetector materials due to their tunable bandgap and desirable properties, such as high responsivity, fast response time, broadband photodetection, photo-detective, and low dark current noise [1]-[7]. However, conventional photodetectors based on these materials often suffer from high power consumption and poor photogenerated carrier collection, resulting from the requirement of high bias voltage and the presence of Schottky barriers. This limitation hinders their use in remote operation conditions, extreme environments, biomedical sensing, and portable devices [8]-[11]. To overcome these challenges, self-driven photodetectors have emerged as promising solutions. These devices

operate with photon energies higher than the material's bandgap, enabling better signal-to-noise ratios and reducing the need for high-bias voltages. Recent studies have demonstrated the feasibility of self-driven photodetectors based on 2D materials [9], [12]-[14]. Among the III-VI group of 2D materials, including InSe, GaSe, and GaTe, there has been a growing interest in studying their light-matter interaction properties for optoelectronic applications [15]-[17]. 2D InSe, with its direct bandgap of approximately 1.25 eV [18], has shown remarkable characteristics for ultrasensitive photodetection compared to other 2D semiconducting materials like MoS2 and WSe2 [19]-[22]. By doping these materials with p- and n-type dopants, atomically sharp p-n junctions can be formed, enabling the construction of heterostructure devices with tailored properties [23]-[25]. Overall, the combination of the unique properties of 2D semiconducting materials, such as InSe, and the formation of heterostructures through doping opens exciting possibilities for high-performance photodetectors with improved efficiency and reduced power consumption.

Although there have been comprehensive studies on InSe-based photodetectors in the visible spectrum, their exploration in the near-infrared (NIR) range is still limited [26], [27]. Optoelectronic devices designed for detection, modulation, and sensing applications in the mid-infrared (MIR) spectrum face challenges due to the lack of on-chip sources and high production costs [28]-[30]. InSe-based optoelectronic devices are typically configured as transistors, requiring high electrical bias gating and bias voltage [19], [27], [31]. The NIR wavelength at 980 nm finds widespread use in optical humidity sensing applications, such

as monitoring indoor air quality, controlling industrial production processes, and agricultural instrumentation [32], [33]. Moreover, with the advancement of autonomous vehicle technology, LiDAR-based devices operating at wavelengths between 940 nm and 980 nm are employed for short to medium-range positioning and mapping purposes [34], [35]. InSe, with its direct bandgap of 1.25 eV [18], becomes an attractive material for manufacturing optoelectronic devices targeting these specific wavelengths. Therefore, there exists a need to investigate and explore the potential of InSe-based photodetectors for NIR applications, considering their direct bandgap and the growing demand for optoelectronic devices in the humidity sensing and LiDAR fields operating within the 980 nm wavelength range. By addressing these requirements, InSe-based devices hold promise for advancing optoelectronics in the NIR region.

Here, I demonstrate a self-driven p-InSe/n-InSe heterostructure photodetector for NIR applications. The p- and n- doped 2D InSe flakes form the vertical heterostructure stack showing a ~3 times improvement in responsivity and ~3.5 times lower response time as compared to p- or n-type InSe photodetectors thus demonstrating a novel fast and sensitive InSe heterojunction-based NIR photodetector suitable for low power optical sensors or detector devices.

1.19.2 Results and Discussion

Enhancing light-matter interaction by building heterostructures using 2D materials paves the way toward building high-performance and energy-efficient compact photodetectors [36]. The 2D material-based photodetectors are often limited by the high bias voltage required for photon-generated carrier collection due to high resistance and the Schottky barrier [37]. Here, we demonstrate a pn junction-based photodetector using InSe for NIR detection or sensing applications as seen in Fig. 4.6.1a. The 2D InSe flakes are mechanically exfoliated from bulk crystals grown by the vertical Bridgman method and transferred precisely on prefabricated Au/Ti metal contacts using the novel 2D material transfer system discussed in [38]. The optical microscope image of the device is shown in Fig. 4.6.1b. A cross-sectional scanning transmission electron microscopy (STEM) image of the photodetector is shown in Fig. 4.6.7 of the supporting information. The pn InSe heterojunction is formed by the physical contact between Sn-doped InSe (n-type) and Zn-doped InSe (p-type) materials. The band diagram for the device structure can be seen in Fig. 1c where the built-in heterojunction potential helps in collecting the photogenerated carriers in the absence of external electrical bias potential. The material quality was assured after transfer using Raman spectroscopy by monitoring the relative intensities of Raman active modes at A^1_{1g}, A^2_{1g}, and E^1_{2g} [18].

The photovoltaic properties of the p-InSe/n-InSe heterojunction, p-InSe, and n-InSe-based photodetector device are studied at 980 nm under vertical illumination using a free-space optical setup. Fig. 4.6.2 shows the current-voltage (I-V) characteristics for photocurrent measurement of the pn-InSe junction, p-InSe, and n-InSe, where the illumination power is 111.6 μW. The pn-junction device exhibits an order of magnitude higher photocurrent as compared to the p- and n- InSe devices, thus indicating a higher photo absorption at 980 nm for the vdW heterojunction characteristics. Fig. 4.6.2b shows the power-dependent photocurrent response of the pn junction

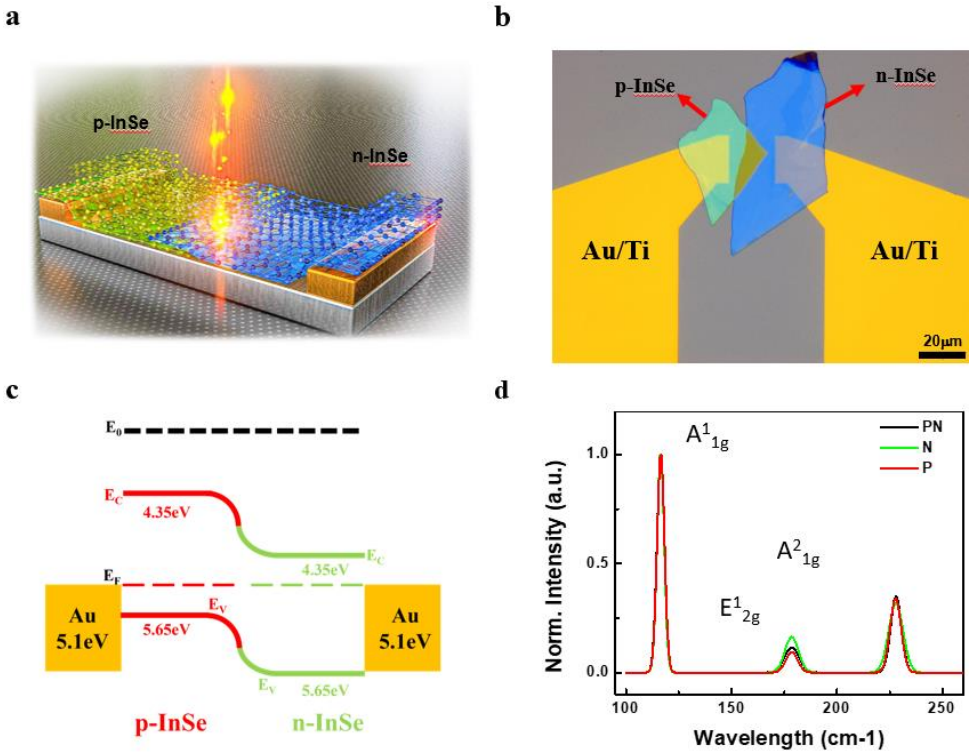

Figure 0.20 PN heterojunction n-InSe/p-InSe photodetector (a) A schematic representation of the n-InSe/p-InSe van der Waals p-n junction photodetector. (b) An optical micrograph image of the

device (top view), where n-InSe was stacked on the top of the p-InSe flake, transferred on Au/Ti electrodes using the 2D printer technique. (c) Band diagram for p-InSe (red), n-InSe (green), and Au contact (yellow). (d) The Raman spectra of the p-InSe, n-InSe, and junction regions. All material-associated Raman peaks of p-InSe, n-InSe, and pn InSe junction are observed to show peak positions and relative intensity associated with out-of-plane vibrational modes (A^1_{1g} and A^2_{1g}) and in-plane vibrational modes (E^1_{2g}).

device. It can be observed that the photocurrent saturates after reaching high optical incident power intensity. The photovoltaic effect is attributed to the built-in electric field in the heterojunction depletion region. Fig. 4.6.2c shows the dark current mapped at different voltages for the device. This shows a very small change in the dark current with an increase in the bias voltage leading to low electrical energy loss. As a result of the built-in potential of the junction, the device can be operated under no external bias for collecting photo-generated carriers. Fig. 4.6.2d shows the relationship between the photocurrent and the input optical power for pn-InSe heterojunction, p-InSe, and n-InSe devices under zero bias voltage at 980 nm light illumination. The built-in potential in the pn junction device shows higher photocurrent generation as compared to the non-junction (p- and n-) type devices.

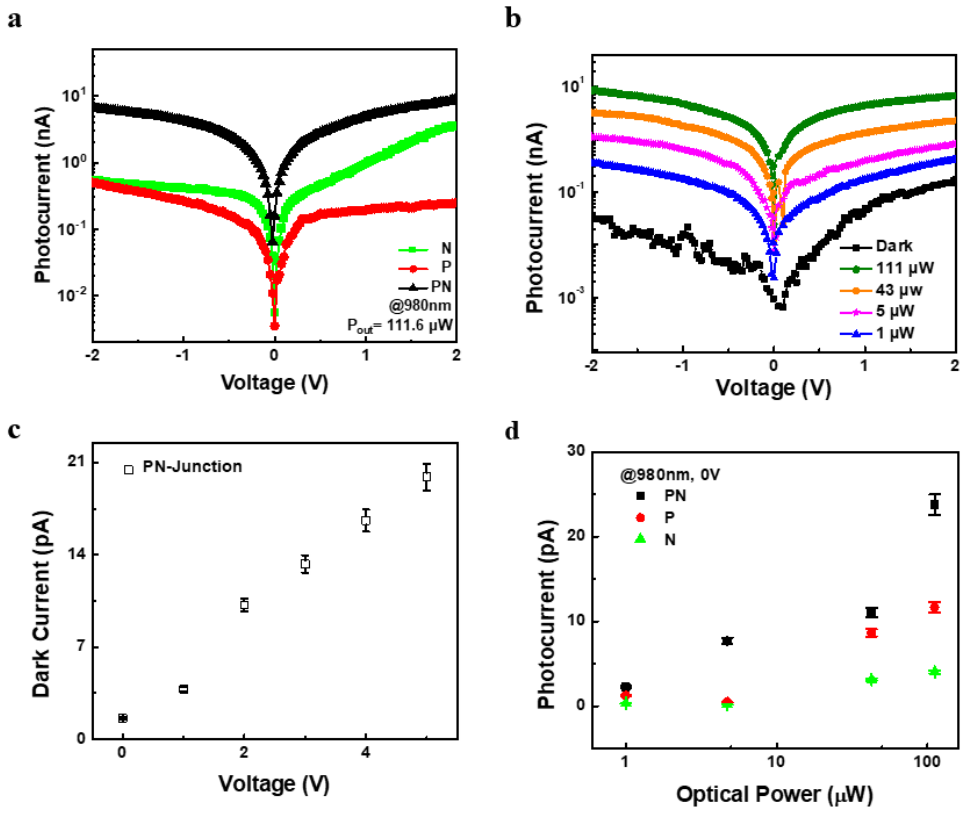

Figure 0.21 The photovoltaic characteristics of pn-InSe heterojunction (a) Typical I–V characteristics of p (red), n (green), and pn junction (black) 2D InSe photodetector. (b) The I-V characteristics of the pn-InSe heterojunction under different optical input power show saturation of photocurrent at higher optical power. (c) Dark current mapping under bias voltage for pn junction device indicates picoamps range currently. This exhibits a noise equivalent power (NEP) of ~2nW/Hz$^{0.5}$ at zero bias. (d) The corresponding fitting curves for the relationship between the photocurrents and the optical power of the p-InSe/n-InSe heterojunction in zero biased voltage, in 980 nm light condition.

Further, the photodetector devices were tested for responsivity as a function of wavelength from 800 nm to 900 nm (supercontinuum source) and at 980 nm (diode laser)

for NIR photodetection. Fig. 4.6.3a shows the responsivity ($R_\lambda=[I_{ph}-I_{dark}]/P_{in}$) of pn heterojunction, p-, and n- InSe at the zero-bias voltage for pn device and 2 V for p- and n-devices. The pn junction device shows enhanced responsivity along the NIR wavelength as compared to n- and p- devices by 3.03 times. It can be found that the maximum responsivity of p-InSe/n-InSe heterojunction is about 0.5 mAW^{-1} at 980 nm under zero bias. The photoluminescence (PL) spectra of the p-InSe, n-InSe, and pn-InSe heterojunctions from 800 nm to 1000 nm were recorded using a 532 nm laser for excitation. The exciton recombination peak at 980 nm (1.265 eV) in the PL spectrum shows the intensity of pn-InSe heterojunction higher than that of p-InSe and n-InSe by ~5.9 times at 980 nm as seen in Fig. 4.6.3b. It is known that the exciton PL is very sensitive to the presence of defects and surface contaminants. The enhanced PL intensity at the pn junction, which is due to the increased photoexcitation volume, provides evidence of a clean interface between the p- and n-InSe flakes. The Raman spectroscopy mapping of the pn junction stack also confirmed the clean heterojunction formed between the two flakes (Fig. 4.6.3c). No additional peaks were observed due to contaminants or defects produced in the material during device fabrication [39].

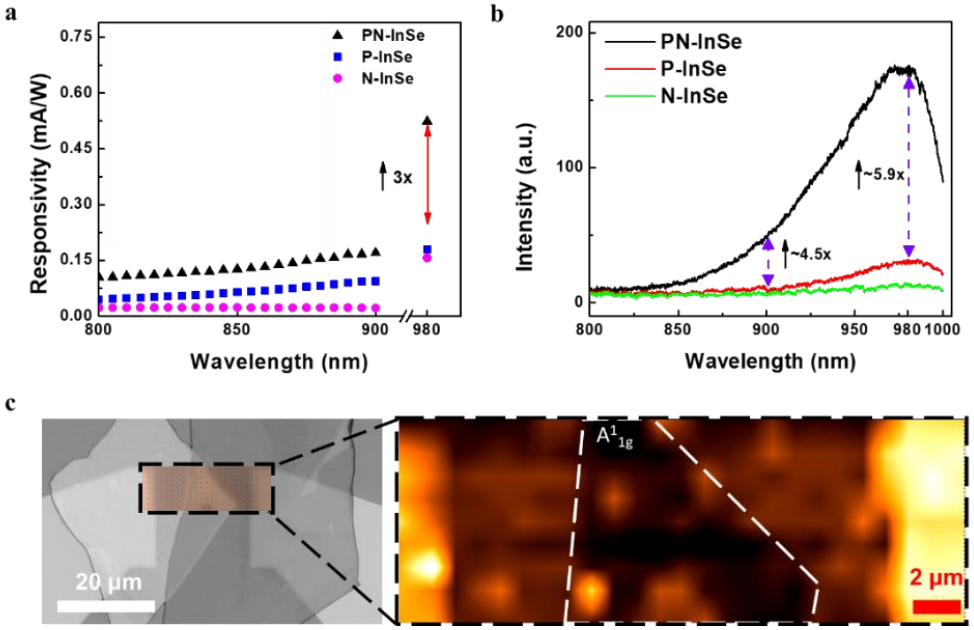

Figure 0.22 Spectral characterization of pn-InSe heterojunction (a) Experimental spectra of responsivity of p-InSe, n-InSe, and pn-InSe heterojunction at 0 V under 800–900 nm and 980 nm light illumination. (b) Photoluminescence spectra of p-InSe, n-InSe, and p-InSe/n-InSe heterojunction show strong agreement with the responsivity spectra. An enhancement of 4.5 times and 5.9 times in intensity is observed at 900 nm and 980 nm, respectively. (c) The quality of the heterojunction created was assessed at the A^1_{1g} Raman peak at the physical position of the heterojunction region (white dashed region), as shown by Raman mapping analysis. A 532 nm laser was used for excitation.

The photoresponse of the pn-InSe photodetector is expected to be higher than the p- and n- InSe due to the built-in potential inside the heterojunction. The on/off switching response for pn-InSe (0 V), p- (-2 V), and n- (2 V) photodetector under 980 nm (111.6 μW) illumination was measured by modulating the optical source power supply. With an

increase in the external electric field, the charge density in the InSe is high leading to a decrease in the mobility of photo-generated carriers because of the decrease in carrier drift velocity. The rise and fall time constants of the pn junction device show a faster response as compared to the p- and n-only InSe photodetectors Fig. 4.6.4. Due to the absence of junction for p- and n- InSe devices, the photocarrier collection is possible only after applying an electrical bias. Therefore, both the devices were tested at 2 V bias for the response time measurement, unlike the built-in electric field of the p-n junction, light-excited electron-hole pairs can be more effectively separated due to the photovoltaic effect versus relying on photoconductivity for the n- and p-only junction devices. The response time of the pn-InSe device shows a rise time/fall time (τ_r/τ_f) response of 8.3 ms/9.6 ms Fig. 4.6.4a, which is reduced as compared to n- and p- InSe device by 18 ms/40 ms **(**Fig. 4.6.4b) and 22 ms/29 ms **(**Fig. 4.6.4c), respectively. This is an interesting result since it shows the engineerability for designing fast-response photodetectors by stacking 2D materials and enhancing the optoelectronic properties of the material for various applications.

The response time of this device is limited by trap states generated in-between material to the substrate and 2D-2D interlayer boundaries. Such trap states help achieve signal detection effectively due to the accumulation of charges but adversely affect the speed response of the device. The trap states generated between the substrate and 2D material majorly contribute to the slow response. This can be improved further by building the device on a 2D substrate material like hBN for preserving the mobility of the material and

achieving a faster response time. The low dark current of the device provides a stable noise floor owing to the presence of built-in potential. As seen in Fig. 4.6.2c, the minute change in dark current with an increase in voltage shows that the device can be operated over a varying range of bias voltage without increasing the noise floor of the device. Such device engineering would provide better solutions to lower power sensing and wearable electronics applications.

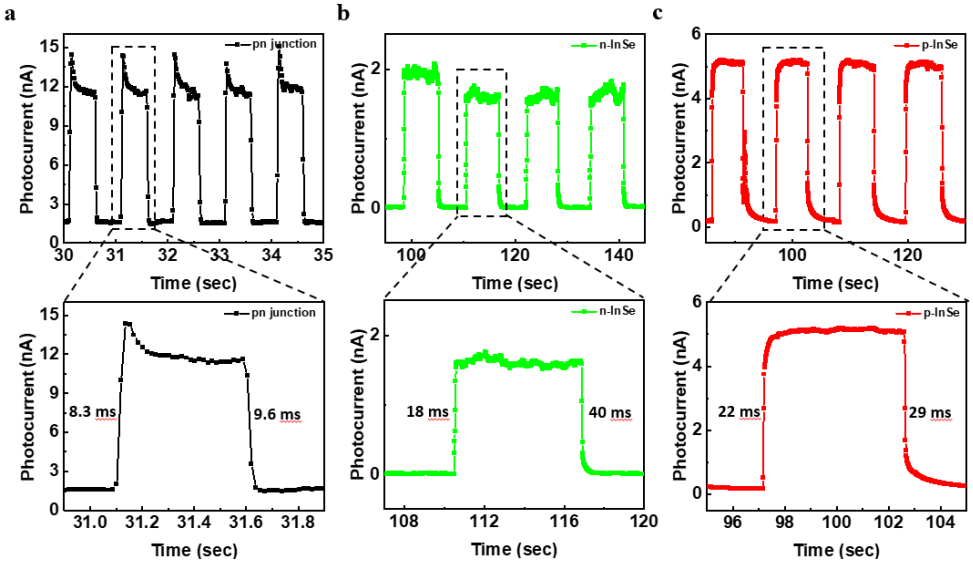

Figure 0.23 Time-dependent photoresponse of (a) pn-InSe photodetector at 0 V with rise time/fall time (τ_r/τ_f) of 8.3 ms/9.6 ms., (b) n-InSe at 2 V with τ_r/τ_f of 18 ms/ 40ms, and (c) p-InSe at -2 V with τ_r/τ_f of 22 ms/29 ms. Under 980 nm light illumination.

Lastly, the pn-junction device was tested for photoresponse and photocurrent mapping at external bias voltages. The gradient map demonstrates a faster response of the device at zero bias and sub-volt forward bias voltages (Fig. 4.6.5a). The nature of the shape of the gradient is governed by the usually observed pn diode I-V characteristics. The separation

of photo-generated electron-hole pairs is better under the influence of external bias voltage. However, the device suffers from high charge density leading to lower drift current velocity in the material. Therefore, the time response and sensitivity of the device are adversely affected by applied external bias. This device shows promising performance for sensing applications in the NIR spectral region owing to its extremely low dark current and response rate at zero external bias. A summary of the tradeoff between the response time of the device and operational voltages is represented in Fig. 4.6.5b based on the current and previously reported photodetector devices for NIR applications [40]-[48]. An additional comparison of performance metrics is shown in Table T1 from previously published work.

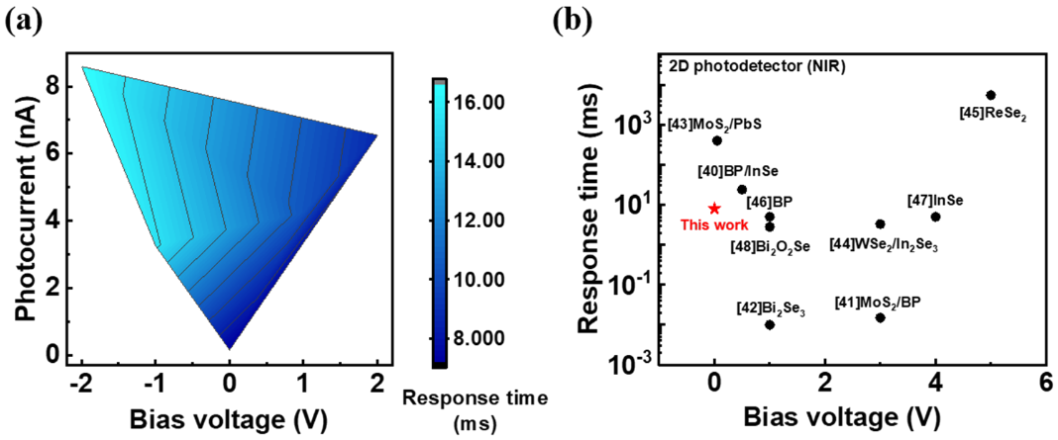

Figure 0.24 Photoresponse mapping under external bias (a) Photoresponse at different bias voltage (-2 V to 2 V) with photocurrent of pn-InSe under 980 nm illumination demonstrated the fastest response under 0 V bias condition. (b) Comparison of the photoresponse under the external bias of 2D photodetectors for NIR applications discussed in the literature.

Materials	λ (nm)	Responsivity (mA/W)	Bias voltage (V)	I_{dark} (nA)	τ_r/τ_f (ms/ms)	Ref.
InSe	700	3.06×10^6	5	~ 200	5/8	[47]
Doped-InSe	980	7.87×10^6	1	800	$0.45/6\times 10^3$	[27]
Bi_2Se_3	1456	274	1	~ 600	54/47	[42]
BP/InSe	633	10^7	0	~100	24/32	[40]
Gr/GaAs	980	5.97	0	0.275	~40	[13]
Te/Ge	980	522	0	-50	14/0.105	[49]
Ge bulk	980	2214	-0.1	~5	-	[50]
MoS_2	473−2712	47.5	1	$\sim 400\times 10^3$	10/16	[51]
InGaAs	1100-2000	3.5×10^6	0.5	144	70/280	[52]
pn-InSe	980	0.5	0	1.5×10^{-3}	8.3/9.6	This work

Table 1.19.1 Comparison of the performance of our n-InSe/p-InSe photodetector with other NIR photodetectors

1.19.3 Conclusion

A self-driven photodetector was realized for NIR applications at 980 nm and an extremely low dark current in the range of a few picoamps was achieved. The photoresponse of the 2D InSe was enhanced by building a pn vdW heterojunction using p- and n- doped InSe showing an increase of ~3 times in responsivity as compared to the control n-InSe and p-InSe photodetector devices. The pn device also exhibits a faster response which is ~3.5 times lower than a p- or n-type InSe photodetector, thus demonstrating a novel fast, and

sensitive InSe heterojunction-based NIR photodetector suitable for low-power optical sensors or detector devices. Such performance of this device shows a high potential for realizing a NIR photodetector for sensing and optical applications. Furthermore, by engineering the interlayer stacking to match closely with the lattice structure and improving the metal contact Schottky barrier, it is expected that the device performance in the NIR region will be further improved. Further investigations are required to determine the chemical and mechanical material stability of the InSe heterojunction structure under various environmental effects for applications like remote sensing and biological sensing.

1.19.4 Methods

Crystal Growth and Characterization

InSe single crystals were grown by the vertical Bridgman-Stockbarger method from non-stoichiometric polycrystalline $In_{1.04}Se_{0.96}$ powders. Tin (2 at. %) and Zn (as ZnSe, 0.3 at.

Figure 0.25 Photograph of a p-InSe ingot cleaved parallel to the c-plane.

%) were added during the powder synthesis to obtain n- and p-typed doped crystals, respectively. The InSe melt in a graphitized quartz ampoule was equilibrated at 720 °C for several hours, then the ampoule was translated across a temperature gradient at a rate of 0.5 mm/h. A representative picture of an InSe ingot is shown in Fig. 4.6.6. The crystal structure was determined using annular dark-field scanning transmission electron microscopy (ADF-STEM) which confirmed the γ phase of InSe (Fig. 4.6.7). Electrical properties were determined from Hall effect measurements in the Van der Pauw geometry at room temperature. For n-InSe (p-InSe), the carrier concentration and Hall mobility are 1.5×10^{16} cm^{-3} and 616 $cm^2V^{-1}s^{-1}$ (7.9×10^{13} cm^{-3} and 43 $cm^2V^{-1}s^{-1}$), respectively.

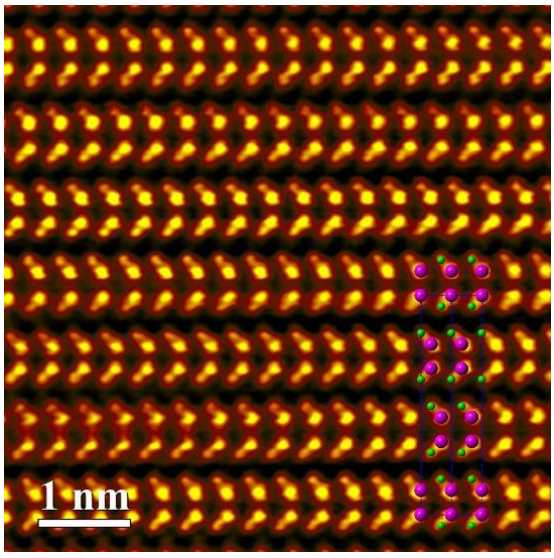

Figure 0.26 Atomic resolution annular dark-field scanning transmission electron microscopy (ADF-STEM) image of InSe showing a good match with the overlapped atomic model of γ-InSe. Green and purple dots in the atomic model represent Se and In atoms, respectively.

Device Fabrication

The InSe pn junction heterostructure is formed using 2D flakes exfoliated from the bulk crystals and transferred using the micro stamp-assisted transfer system on prefabricated electrical contacts [38]. Here, the p- and n-type InSe flakes were obtained by mechanical exfoliation from the bulk crystals using Nitto tape and were transferred to thin (17 mils) PDMS film. Briefly, this method comprises a micro stamper to transfer the material from PDMS which can be aligned under a microscope precisely at any desired device location via micro-positioners as seen in Fig. 4.6.8. We scan the PDMS film from the top to find a flake of interest under the PDMS film and transfer it at a targeted location (between metal contacts) without any cross-contamination of other 2D material flakes on PDMS on the substrate. The micro-stamper guides a flake to the target location and transfers it onto the substrate by pressing the PDMS film gently. The sample is rinsed cleaned using acetone and isopropyl alcohol and dried using nitrogen gas after each transfer of layer. The sample is soft-baked at 85 ˚C for 2 min (APR). We added a video link in the manuscript as a reference, with the published 2D printer work [53], [54] which describes our rapid, clean, and precise transfer method. Note, the video shows the rapid integration of van der Waals heterostructure on top of a Si photonic chip (IMEC) by precisely placing two different 2D materials (2H-$MoTe_2$ and hBN), by using our novel 2D printer technique for on-chip photonic devices. The electrical contacts were formed using electron beam lithography for a channel length of 20 μm. The metal Ti/Au (5 nm/45 nm) contacts were formed by

deposition using the electron beam evaporation method. The lift-off was performed using acetone at room temperature followed by rinsing in isopropyl alcohol and nitrogen drying.

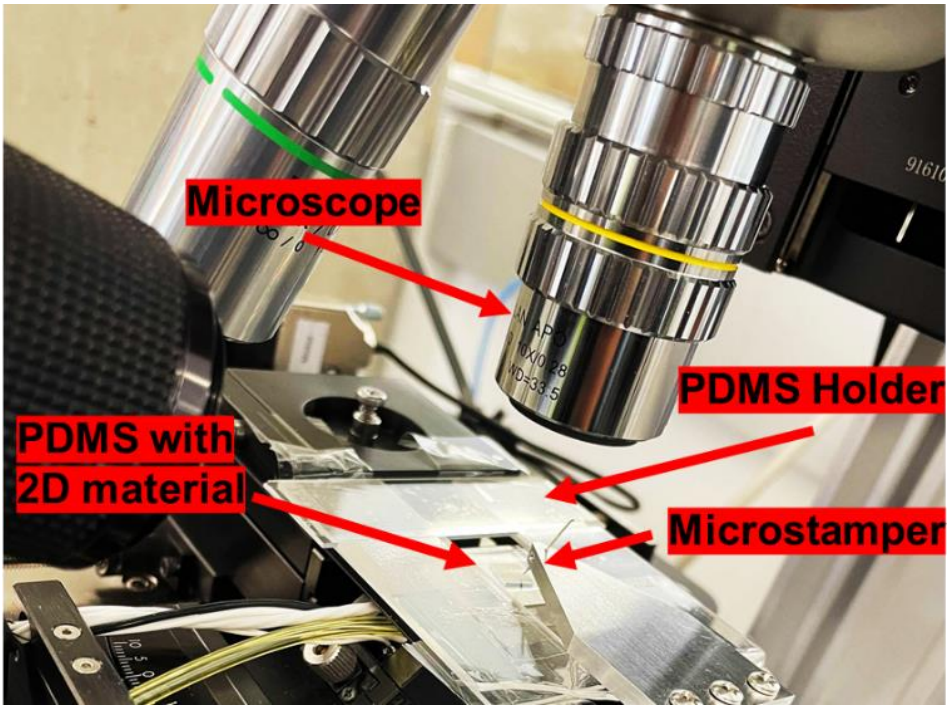

Figure 0.27 2D Printer transfer setup used for building the pn heterojunction photodetector.

Scanning transmission electron microscopy (STEM) characterization

An FEI Nova NanoLab 600 dual-beam system (SEM/FIB) was employed to prepare an electron-transparent cross-sectional sample. Electron-beam-induced deposition of 100 nm thick Pt was initially deposited on top of the 2D pn junction device to protect the sample surface, then followed by 2 µm ion-beam induced Pt deposition. To reduce Ga-ions damage, in the final stage of FIB preparation, the sample was thinned with 2 kV Ga-ions using a low beam current of 29 pA and a small incident angle of 3 degrees. An FEI Titan 80-300

STEM/TEM equipped with a probe spherical-aberration corrector was employed to obtain annular dark field (ADF) STEM images with an operating voltage of 300 kV, probe convergence semi-angle of 14 mrad, and collection angle of 34-195 mrad. A typical cross-sectional ADF-STEM image of the pn InSe photodetector shown in Fig. 4.6.9 suggests the 2D flakes have good contact with the Au/Ti electrode, as well as in the p-n junction region.

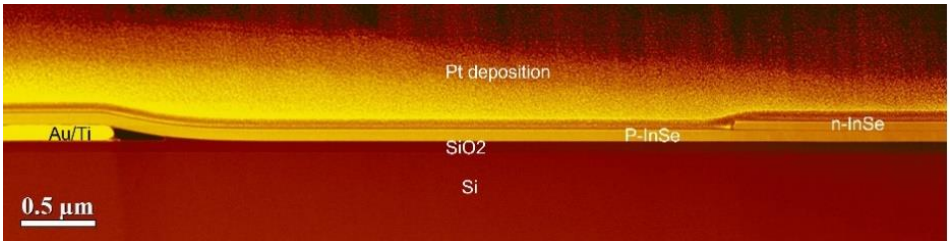

Figure 0.28 Cross-sectional ADF-STEM image of the pn-InSe photodetector fabricated using the 2D printer transfer setup.

Device Experimentation

The experimental setup for measuring the 2D InSe pn junction heterostructure devices comprises a tunable (NKT SUPERCONTINUUM Compact) source and a fixed wavelength laser diode module (CPS980 Thorlabs, INC.) at 980 nm wavelength. The light beam was focused on the device using an objective lens. A source meter (Keithley 2600B) was used for electrical response measurements. The response time of the device was measured by modulating the electrical power supply to the laser. The Raman and photoluminescence measurements were performed at room temperature using a 532 nm laser. InSe crystal structure and interface quality of the pn photodetectors were examined

using an FEI Titan 80-300 probe-corrected scanning transmission electron microscope (STEM) operating at 300 keV.

1.19.5 References

[1] M. Buscema *et al*, "Photovoltaic effect in few-layer black phosphorus PN junctions defined by local electrostatic gating," *Nature Communications,* vol. 5, *(1),* pp. 1-6, 2014.

[2] Y. Chen *et al*, "Two-dimensional WSe2/SnSe pn junctions secure ultrahigh thermoelectric performance in n-type Pb/I Co-doped polycrystalline SnSe," *Materials Today Physics,* vol. 16, pp. 100306, 2021.

[3] S. Kang *et al*, "2D semiconducting materials for electronic and optoelectronic applications: potential and challenge," *2D Materials,* vol. 7, *(2),* pp. 022003, 2020.

[4] L. Lv *et al*, "Design and tailoring of two-dimensional Schottky, PN and tunnelling junctions for electronics and optoelectronics," *Nanoscale,* vol. 13, *(14),* pp. 6713-6751, 2021.

[5] R. Maiti *et al*, "Strain-engineered high-responsivity MoTe 2 photodetector for silicon photonic integrated circuits," *Nature Photonics,* vol. 14, *(9),* pp. 578-584, 2020.

[6] X. Yuan *et al*, "Wafer-scale arrayed pn junctions based on few-layer epitaxial GaTe," *Nano Research,* vol. 8, *(10),* pp. 3332-3341, 2015.

[7] T. Zheng *et al*, "Layer-number dependent and structural defect related optical properties of InSe," *RSC Advances,* vol. 7, *(87),* pp. 54964-54968, 2017.

[8] Y. Wang *et al*, "Applications of 2D-Layered Palladium Diselenide and Its van der Waals Heterostructures in Electronics and Optoelectronics," *Nano-Micro Letters,* vol. 13, *(1),* pp. 1-52, 2021.

[9] X. Zhang *et al*, "High performance broadband self-driven photodetector based on MXene (Ti3C2Tx)/GaAs Schottky junction," *Mater Des,* pp. 109850, 2021.

[10] Q. Han *et al*, "Integrating Near-Infrared Visual Fluorescence with a Photoelectrochemical Sensing System for Dual Readout Detection of Biomolecules," *Anal. Chem.,* vol. 93, *(7),* pp. 3486-3492, 2021.

[11] Q. Wu *et al*, "A simple-structured silicon photodetector possessing asymmetric Schottky junction for NIR imaging," *Physics Letters A,* pp. 127586, 2021.

[12] H. Shang *et al*, "A mixed-dimensional 1D Se–2D InSe van der Waals heterojunction for high responsivity self-powered photodetectors," *Nanoscale Horizons,* vol. 5, *(3),* pp. 564-572, 2020.

[13] J. Wu *et al*, "Enhanced performance of a graphene/GaAs self-driven near-infrared photodetector with upconversion nanoparticles," *Nanoscale,* vol. 10, *(17),* pp. 8023-8030, 2018.

[14] Y. Liu *et al*, "Self-powered and high responsivity photodetector based on a n-Si/p-GaTe heterojunction," *Nanotechnology,* vol. 32, *(22),* pp. 225204, 2021.

[15] H. Zhong, Z. Bai and B. Zou, "Tuning the luminescence properties of colloidal I–III–VI semiconductor nanocrystals for optoelectronics and biotechnology applications," *The Journal of Physical Chemistry Letters,* vol. 3, *(21),* pp. 3167-3175, 2012.

[16] Z. Yang and J. Hao, "Recent progress in 2D layered III–VI semiconductors and their heterostructures for optoelectronic device applications," *Advanced Materials Technologies,* vol. 4, *(8),* pp. 1900108, 2019.

[17] C. Ho, "Thickness-dependent carrier transport and optically enhanced transconductance gain in III-VI multilayer InSe," *2D Materials,* vol. 3, *(2),* pp. 025019, 2016.

[18] M. R. Molas *et al*, "Raman spectroscopy of GaSe and InSe post-transition metal chalcogenides layers," *Faraday Discuss.,* vol. 227, pp. 163-170, 2021.

[19] Z. Chen, J. Biscaras and A. Shukla, "A high performance graphene/few-layer InSe photo-detector," *Nanoscale,* vol. 7, *(14),* pp. 5981-5986, 2015.

[20] W. Feng *et al*, "Ultrahigh photo-responsivity and detectivity in multilayer InSe nanosheets phototransistors with broadband response," *Journal of Materials Chemistry C,* vol. 3, *(27),* pp. 7022-7028, 2015.

[21] O. Lopez-Sanchez *et al*, "Ultrasensitive photodetectors based on monolayer MoS 2," *Nature Nanotechnology,* vol. 8, *(7),* pp. 497-501, 2013.

[22] D. A. Nguyen *et al*, "Highly enhanced photoresponsivity of a monolayer WSe2 photodetector with nitrogen-doped graphene quantum dots," *ACS Applied Materials & Interfaces,* vol. 10, *(12),* pp. 10322-10329, 2018.

[23] R. Cheng *et al*, "Electroluminescence and photocurrent generation from atomically sharp WSe2/MoS2 heterojunction p–n diodes," *Nano Letters,* vol. 14, *(10),* pp. 5590-5597, 2014.

[24] S. R. Tamalampudi *et al*, "High performance and bendable few-layered InSe photodetectors with broad spectral response," *Nano Letters,* vol. 14, *(5),* pp. 2800-2806, 2014.

[25] F. Wang *et al*, "Tunable GaTe-MoS2 van der Waals p–n junctions with novel optoelectronic performance," *Nano Letters,* vol. 15, *(11),* pp. 7558-7566, 2015.

[26] M. Dai *et al*, "A dual-band multilayer InSe self-powered photodetector with high performance induced by surface plasmon resonance and asymmetric Schottky junction," *ACS Nano,* vol. 12, *(8),* pp. 8739-8747, 2018.

[27] H. Jang *et al*, "High-Performance Near-Infrared Photodetectors Based on Surface-Doped InSe," *Advanced Functional Materials,* vol. 31, *(3),* pp. 2006788, 2021.

[28] E. Heidari *et al*, "On-chip Fourier transform spectrometer on silicon-on-sapphire," *Opt. Lett.,* vol. 44, *(11),* pp. 2883-2886, 2019.

[29] E. Heidari *et al*, "Hexagonal transverse-coupled-cavity VCSEL redefining the high-speed lasers," *Nanophotonics,* vol. 9, *(16),* pp. 4743-4748, 2020.

[30] A. Rostamian *et al*, "Towards lab-on-chip ultrasensitive ethanol detection using photonic crystal waveguide operating in the mid-infrared," *Nanophotonics,* vol. 10, *(6),* pp. 1675-1682, 2021.

[31] L. Liu *et al*, "Ferroelectric-gated InSe photodetectors with high on/off ratios and photoresponsivity," *Nano Letters,* vol. 20, *(9),* pp. 6666-6673, 2020.

[32] H. Li *et al*, "Optical humidity sensor based on ZnO nanomaterials," in *2020 IEEE 5th Optoelectronics Global Conference (OGC),* 2020, .

[33] S. Sikarwar *et al*, "Fabrication of nanostructured yttria stabilized zirconia multilayered films and their optical humidity sensing capabilities based on transmission," *Sensors Actuators B: Chem.,* vol. 232, pp. 283-291, 2016.

[34] H. J. Lee, K. Y. Jung and Y. Kim, "Nanostructured Fe 2 O 3/TiO 2 composite particles with enhanced NIR reflectance for application to LiDAR detectable cool pigments," *RSC Advances,* vol. 11, *(28),* pp. 16834-16840, 2021.

[35] A. Jha, "A review of visible, near-IR, and mid-IR transitions in rare-earth doped glass waveguides for remote sensing and LIDAR," in *Lidar Remote Sensing for Environmental Monitoring VII,* 2006, .

[36] R. Maiti *et al*, "Loss and coupling tuning via heterogeneous integration of MoS 2 layers in silicon photonics," *Optical Materials Express,* vol. 9, *(2),* pp. 751-759, 2019.

[37] C. Patil, R. Maiti and V. J. Sorger, "WS2 monolayer integrated photodetector," in *CLEO: QELS_Fundamental Science,* 2020, .

[38] R. A. Hemnani *et al*, "2D material printer: a deterministic cross contamination-free transfer method for atomically layered materials," *2D Mater.*, vol. 6, *(1)*, pp. 015006, 2018. Available: https://doi.org/10.1088/2053-1583/aae62a. DOI: 10.1088/2053-1583/aae62a.

[39] S. Gupta, E. Heintzman and J. Jasinski, "Multiphonon Raman spectroscopy properties and Raman mapping of 2D van der Waals solids: graphene and beyond," *J. Raman Spectrosc.*, vol. 46, *(2)*, pp. 217-230, 2015.

[40] S. Zhao *et al*, "Highly Polarized and Fast Photoresponse of Black Phosphorus-InSe Vertical p–n Heterojunctions," *Advanced Functional Materials*, vol. 28, *(34)*, pp. 1802011, 2018.

[41] L. Ye *et al*, "Near-infrared photodetector based on MoS2/black phosphorus heterojunction," *Acs Photonics*, vol. 3, *(4)*, pp. 692-699, 2016.

[42] F. Wang *et al*, "Submillimeter 2D Bi2Se3 Flakes toward High-Performance Infrared Photodetection at Optical Communication Wavelength," *Advanced Functional Materials*, vol. 28, *(33)*, pp. 1802707, 2018.

[43] D. Kufer *et al*, "Hybrid 2D–0D MoS2–PbS quantum dot photodetectors," *Adv Mater*, vol. 27, *(1)*, pp. 176-180, 2015.

[44] H. J. Jin *et al*, "Ultrasensitive WSe2/α-In2Se3 NIR Photodetector Based on Ferroelectric Gating Effect," *Advanced Materials Technologies*, vol. n/a, *(n/a)*, pp.

2100494, Available: https://onlinelibrary.wiley.com/doi/abs/10.1002/admt.202100494. DOI: 10.1002/admt.202100494.

[45] M. Hafeez *et al*, "Chemical vapor deposition synthesis of ultrathin hexagonal ReSe2 flakes for anisotropic raman property and optoelectronic application," *Adv Mater,* vol. 28, *(37),* pp. 8296-8301, 2016.

[46] H. Fu *et al*, "Different-sized black phosphorus nanosheets with good cytocompatibility and high photothermal performance," *RSC Advances,* vol. 7, *(24),* pp. 14618-14624, 2017.

[47] W. Feng *et al*, "Ultrahigh photo-responsivity and detectivity in multilayer InSe nanosheets phototransistors with broadband response," *Journal of Materials Chemistry C,* vol. 3, *(27),* pp. 7022-7028, 2015.

[48] B. Chitara *et al*, "Ultrathin Bi 2 O 2 S nanosheet near-infrared photodetectors," *Nanoscale,* vol. 12, *(30),* pp. 16285-16291, 2020.

[49] B. Zheng *et al*, "Large-Area Tellurium/Germanium Heterojunction Grown by Molecular Beam Epitaxy for High-Performance Self-Powered Photodetector," *Advanced Optical Materials,* vol. 9, *(20),* pp. 2101052, 2021.

[50] C. Hsin *et al*, "Si/Ge/Si photodetector by rapid-melting-growth technique," *IEEE Transactions on Nanotechnology,* vol. 17, *(3),* pp. 607-610, 2018.

[51] Z. Huang *et al*, "Amorphous MoS2 photodetector with ultra-broadband response," *ACS Applied Electronic Materials,* vol. 1, *(7),* pp. 1314-1321, 2019.

[52] H. Tan *et al*, "Single-crystalline InGaAs nanowires for room-temperature high-performance near-infrared photodetectors," *Nano-Micro Letters*, vol. 8, *(1)*, pp. 29-35, 2016.

[53] C. Patil *et al*, "Highly accurate, reliable and non-contaminating two-dimensional material transfer system," in *2021 26th Microoptics Conference (MOC)*, 2021, .

[54] Anonymous (). *2D Material Printer*. Available: https://sorger.seas.gwu.edu/2d-material-printer.html.

TCO Integrated High-Speed Electro-Optical Modulator

1.20 Introduction

Photonic integrated circuits (PIC) have recently been investigated for the interconnectivity functions of neural networks that need condensed on-chip solutions. With the increased need for large data processing, transport, and storage; optimizing the energy consumption of present systems is getting more difficult. Inter-chip and on-chip photonic interconnects, photonic analog to digital conversion, communications, and sensors all use integrated electro-optic (EO) modulators [1]. The FOM (figure of merit) for modulators is typically characterized by high-speed, superior-energy efficiency [2], high extinction ratio, low insertion loss, and compact footprint. Integrated plasmonic modulators facilitate the enhancement of light-matter interaction, resulting in high-bandwidth and compact footprint-devices. However, the substantial insertion loss due to the plasmonic mode is high, limiting the signal propagation distance and operation energy [3]. Silicon (Si) suffers

from weak index tuning due to the low carrier-induced plasma dispersion, and low bandgap. The low EO response of Si in monolithically integrated EO components, on the other hand, results in a huge footprint. Among the most used TCO materials are indium tin oxide (ITO), tin oxide (SnO_2), zinc oxide (ZnO), and indium oxide (In_2O_3). However, the design and synthesis of enhanced TCO materials that result in a significant increase in conductivity and resilience are still widely required, and a better knowledge of the conductivity mechanisms is essential for continued advancement. The advantages of using ITO over Si in PIC modulation are governed by the high carrier concentration in ITO enabling higher modulation of the dispersion behavior. Further facilitating strong effective index modulation under the influence of electrical bias owing to the lower permittivity of ITO and the presence of epsilon near zero (ENZ) region. The complementary metal–oxide semiconductor (CMOS) compatibility of ITO provides a foundry-level integration with the Si photonic process.

Here we demonstrate a compact heterogeneously integrated ITO-based modulator on Si photonic platform. Here, we select indium-tin-oxide (ITO) as the EO material and aluminum oxide (Al_2O_3) as dielectric forming an ITO-Al_2O_3 capacitive gate-stack on a Si photonic directional coupler (Si-DC) waveguide structure to form a heterogeneously integrated modulator. ITO provides the carrier concentration modulation in the order of ~1020 cm^{-3}, which results in a refractive tuning in unity order [4], unity-strong optical index modulation ($\Delta n \sim 1$; epsilon-near-zero (ENZ)) condition [5], and belongs to the class

of transparent conducting oxides (TCO) family massively for touch screens and transparent low-resistive front-end contact, respectively [6] paving the way towards large scale foundry production. The concept of using imaginary part index tunings for modulation is indeed interesting and an integral part of the novel tunable critical coupling modulation with isolation of dynamic insertion loss from the output bus introduced in the work discussed in this manuscript.

1.21 Loss-induced index mismatch for coupling-based modulation

The ITO-based directional switch for Si DC devices was first introduced by [7], with an ITO/metal stack placed on a waveguide to enhance the light-matter (ITO) interaction and realize a large index mismatch between both waveguides to control the coupling conditions. The low mode overlap of the photonic mode does not enable us with a high extinction ratio for switching in free carrier-based modulators. In contrast, we experimentally investigate a unique modulation mechanism characterized by the stacking of the ITO/Al_2O_3 layer across both waveguides with the ITO layer being disconnected by a gap between the input waveguide and the coupling waveguide (Fig. 5.3.1a). The effective index-sensitive coupling mechanism here provides an efficient modulation technique. The independent ITO coverage over both waveguides maintains the symmetricity between both the waveguides preserving the designed effective beating length for coupling conditions for Si DC. In the framework of coupled-mode theory, the device shown in Fig. 1 is described with coupled-mode equations.

$$\frac{d}{dz}\begin{bmatrix}a_1\\a_2\end{bmatrix} = i\begin{bmatrix}i\gamma_0 & \kappa\\ \kappa & i\gamma_0 + i\gamma(V) + \delta(V)\end{bmatrix}\begin{bmatrix}a_1\\a_2\end{bmatrix} \quad \text{——————(1)}$$

where, $a_{1,2}(z)$ represent the complex modal amplitudes of the electric field in the two channels, κ is the coupling coefficient, γ_0 is the unbiased ITO loss in either channel, while γ and δ respectively represent the loss and detuning induced by the applied voltage in the second channel. Assuming the loss dominates the detuning, i.e., $\gamma \gg \delta$, one can show that with respect to a reference loss value of $\gamma_0 + \gamma/2$, this system exhibits parity-time (PT) symmetry [8]. In this case, the propagation constants of the two super modes of the complex coupler are obtained as $\beta_{1,2} = \beta_0 + i(\gamma_0 + \gamma/2) \pm \sqrt{\kappa^2 - \gamma^2/4}$, where β_0 is the propagation constant of an individual waveguide with an unbiased ITO. This system exhibits an exceptional point singularity at the critical loss level of $\gamma = 2\kappa$. Accordingly, one can show that by increasing the loss in one arm of this complex coupler, the transmission in the other arm unedges an interesting transition, where the transmission first decreases and then increases beyond a critical level of loss [8]. This interesting effect, called loss-induced transparency, forms the foundations of the proposed ITO modulator. The optical mode profile and transmission were observed for the device using three-dimensional finite difference time domain simulations (FDTD). The effective refractive index of the coupled waveguide was tuned by introducing loss using an imaginary part of the refractive index.

1.22 Results and Discussion

Alterations in the refractive index disrupt the symmetry conditions (n_bus = n_coupled), thereby instigating a modification in the device's effective beating length as well as the conditions of the effective coupling gap. The increase in loss on the coupling waveguide decreases the transparency of the coupled waveguide. This guides the signal in the bus waveguide leading to a switching effect. The signal suffers from coupling losses and inherits insertion loss caused due to the presence of the ITO on the bus waveguide. The transmission change can be observed in Fig. 5.3.1b, where the decrease in the transmission in coupled waveguide induced due to loss using external electrical bias leads to switching of the signal to the bus waveguide. The mode profile obtained from simulations for change in imaginary refractive index (K) can be observed in Fig. 5.3.1c. The mode profile shows the loss in signal due to the coupling conditions due to the presence of a high loss

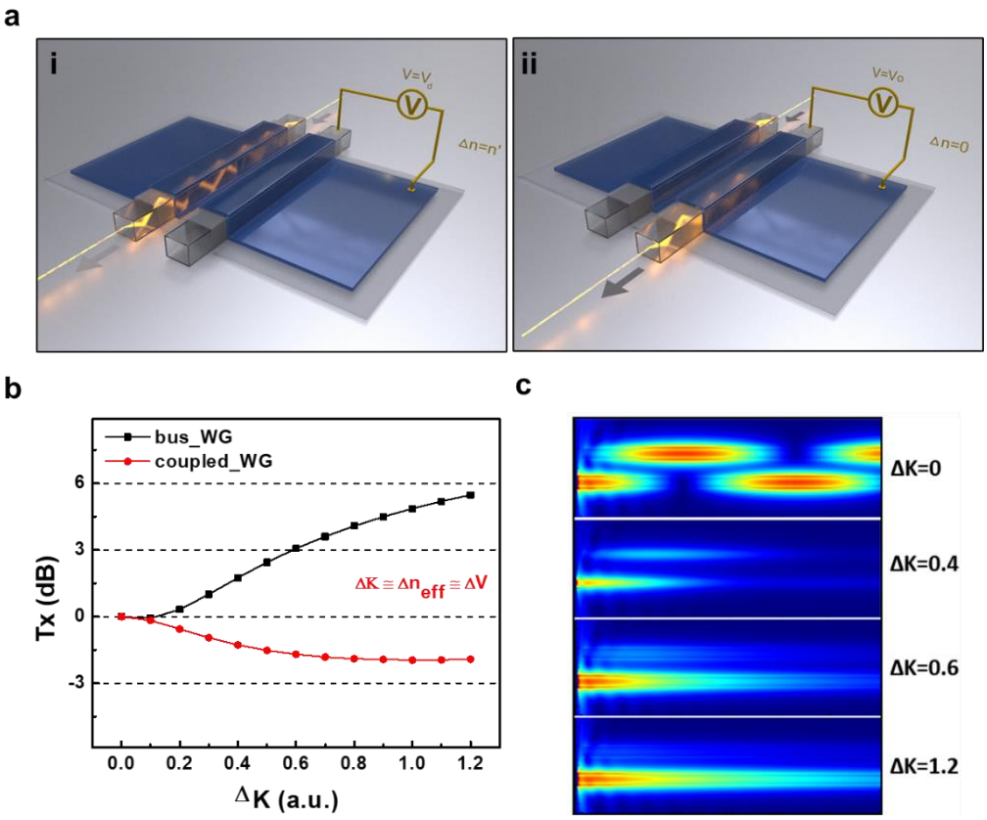

Figure 0.1 Loss Enabled Coupling Effect in Si Directional Coupler (a) Conceptual schematic diagram representing that a low-loss system will be more critically coupled to its environment than a high-loss system because of impedance matching. A Si directional coupler undergoes asymmetricity under the influence of external bias resulting in decreased transparency of the coupling waveguide due to optical loss insertion. (b) The signal tends to guide through the bus waveguide (bus_WG) avoiding the high loss system in the coupled waveguide(coupled_WG) with an increase in bias voltage. 3D FDTD simulation results show (b) the change in optical signal with a variation of the imaginary index (Δk) part with the application of external electrical bias in both waveguides. (c) Optical mode profile simulation shows the switching of the signal as the loss is induced in the coupling waveguide of Si-DC.

system and due to the Rayleigh scattering losses due to the curved edge shape of the waveguide due to fabrication effects. The simulation was performed on the close-to-experimental physical structure of the device investigated using SEM and FIB-SEM. This helps in understanding the losses observed in experimental results much more effectively in comparison to the simulation results. The material properties were considered for 1.55 μm wavelength throughout the simulation. The independent tuning of the coupling waveguide by isolation of the ITO layer helps in reducing the dynamic insertion loss in the bus waveguide caused due to carrier injection under the influence of external bias. Usually, the free carrier-based modulators suffer high insertion loss for the comparable active area of the device (ref!). By covering both the waveguide with the active tuning layers a significant energy is consumed to tune the coupling state. This limits the energy efficiency and also the bandwidth of the device due to an increase in parasitic electrical impedance.

The Si DC-based ITO modulator structurally consists of a silicon photonic waveguide and another coupling waveguide separated 900 nm away from the bus. Both the waveguides have grating couplers for the input and output of optical signal and are of the same length to form symmetricity (Fig. 5.3.2a). Silicon waveguides are etched using induced plasma dry etching which shows the side and the Al_2O_3 is deposited on top of the coupling region using the atomic layer deposition technique, where the oxide serves as electrical isolation and dielectric medium for the capacitance. It is important to observe that the coupling

waveguide is curved from the bus waveguide to reduce the back reflection of light due to the abrupt effective index change for the propagation, minimizing the insertion loss from the Si waveguide coupling into the device due to backscattering. The ITO layer is deposited using ion beam deposition and further annealed for the curing process. Both ITO/Al_2O_3 layers cover conformally the entire coupling/active region with a separation of the ITO layer in the gap as seen in the schematic in Fig. 5.3.2b verified by FIB-SEM in Fig. 5.3.2d.

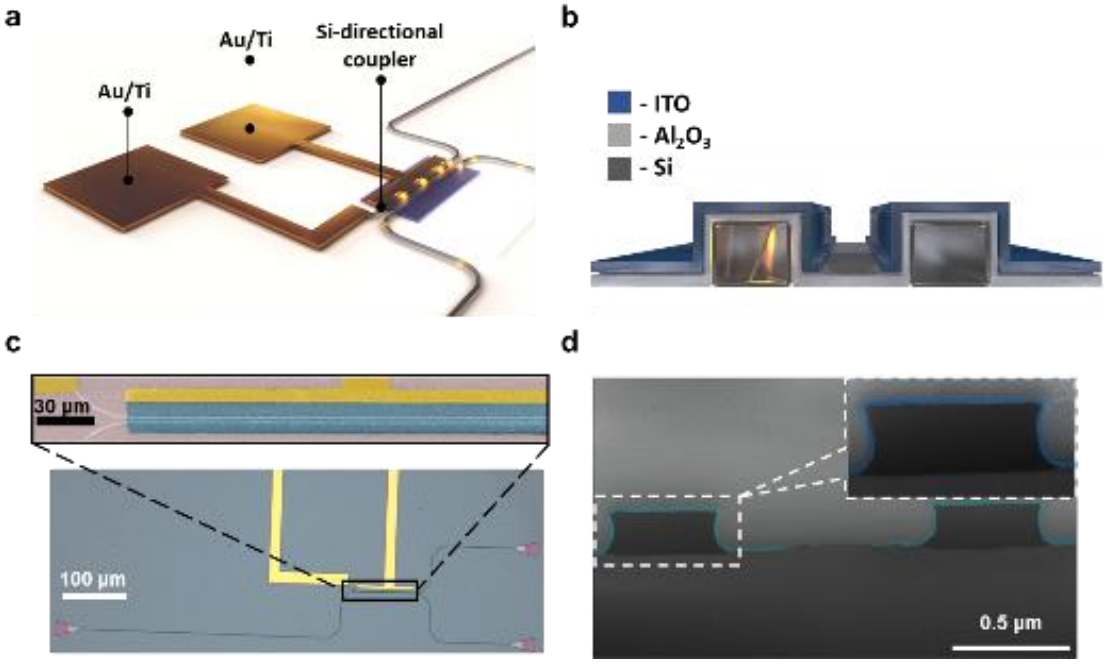

Figure 0.2 Integrated ITO Modulator device design (a) Schematic representation of heterogeneously integrated ITO modulator device on a silicon photonic directional coupler waveguide. (b) Schematic cross-section of the device showing the ITO layer of ~10 nm separated by a ~10 nm interlayer Al_2O_3 dielectric forming a parallel-plate capacitor configuration. (c) Optical micrograph showing bus waveguide, coupling waveguide, and Ti/Au metallization. The magnified image above shows the SEM of the cross-section for the layers atop the device with the inset

showing a microscope image of the device showing the top view of the electrical contact structure and the input and output grating couplers. (d) FIB-SEM image showing the separated ITO layers (false-colored) between the two waveguides.

With 0.2V bias, the strong free-carrier absorption from ITO increases the linear absorption of the super mode in the coupling waveguide. Thus, more optical energy transfers from the coupling waveguide to the input waveguide due to changes in critical coupling conditions. Hence, the tunned coupling coefficient from real index modulation and higher free-carrier absorption accompanying the effective index change contributes to the intensity modulation, resulting in an ER= 3.4 dB as seen in Fig. 5.3.3a. As compared to short active area ITO modulator devices [8] we achieved very low channel resistance (~50 Ω) due to long channel length and reduced the electrical biasing by a factor of 10^2 for similar ER. This further improves the bandwidth response of the device to 40 GHz as seen in Fig. 5.3.3b and a modulation energy consumption in the range of 1 fJ/bit. The spectral response of the device shows dual-band operation in the C-band wavelength range as shown in Fig. 5.3.4b. The device was also tested for thermal stability from 20^{o}C to 100^{o}C as shown in Fig. 5.3.3b. The thermal stability was tested by heating the sample over a heated stage while monitoring the change in the output signal. The sample was tested at room temperature and ambient air.

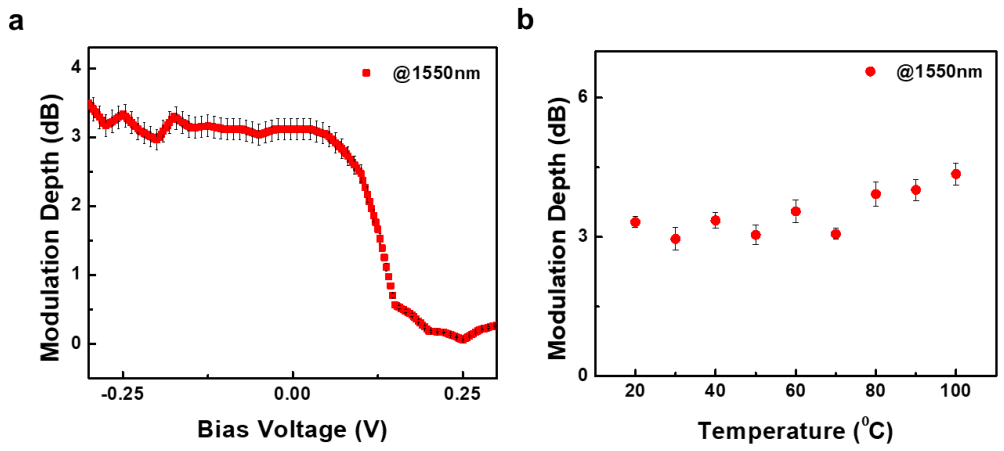

Figure 0.3 Electro-optic performance (a) Modulation depth as a function of electrical biasing observed in the input waveguide highlighting the 3.4 dB ER at 0.2 V of applied bias voltage. (b) A Dual-band operation response was observed due to the resonance condition of the directional coupler.

The device shows a high bandwidth small signal response (S_{21}) of 40 GHz intensity modulation for a 3dB roll-off. The measurement setup schematic can be seen in Fig. S3. All the measurement conditions were calibrated, and parameters were normalized for 1.55 μm wavelength operation. The bandwidth characteristics can be seen in Fig. 5.3.4.

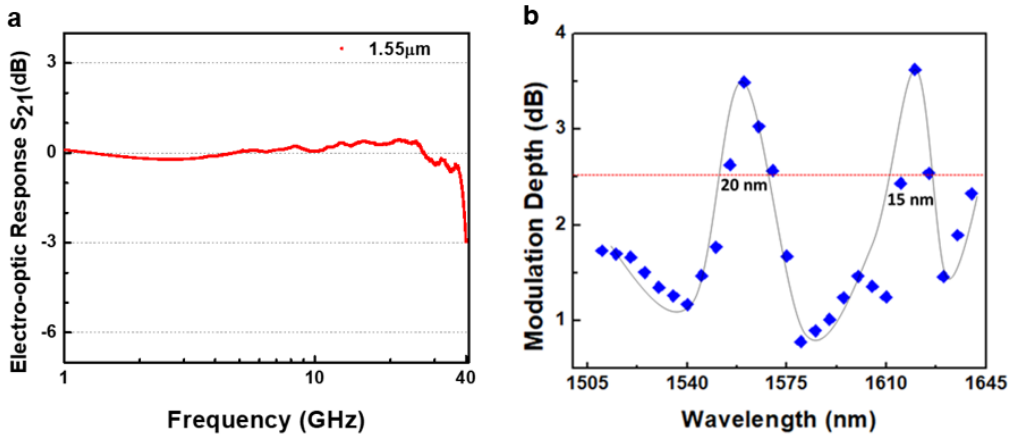

Figure 0.4 **Bandwidth Response** The experimentally measured small-signal response S_{21} of the modulator shows the bandwidth of the device up to 40 GHz for 3 dB roll-off at λ=1550 nm.

1.23 Conclusion

The ITO and Si are electrically contacted using Au/Ti on the coupling waveguide to alter both the absorption and beating length of the DC and achieve critical coupling modulation. The coupling conditions are electrically controlled by tuning the loss in the coupling waveguide, isolating the dynamic insertion loss from the input waveguide. Therefore, we observe a static insertion loss (~5.8 dB) along the input waveguide due to small scattering and absorptive losses from ITO/Al_2O_3 layer and grating coupler efficiency. Under the absence of electrical bias, both ITO layers on waveguides are in flat band condition. The capacitive gating, to the ITO layer on the coupling waveguide, achieves a higher linear absorption compared to zero-bias states due to carrier accumulation. The carrier accumulation reduces the refractive index of ITO; thus, the beating length between two waveguides of Si DC is altered. As the coupling coefficient depends on the gap size and coupling length, lower optical power is transferred to the coupling waveguide with applied electrical bias due to induced absorption loss [7]. Therefore, we observe an increase in transmission of the input waveguide forming the ON state of the device due to asymmetric coupling conditions. We claim that the effective real and imaginary index parts of ITO contribute synergistically to the modulation depth, but the imaginary part tends to dominate owing to the high carrier concentration in ITO.

We propose and experimentally demonstrate a novel loss tunable coupling modulation using ultra-low energy/bit and heterogeneously integrating ITO on a symmetric Si DC waveguide system. This modulator device shows high optical index modulation of the ITO/Al_2O_3/Si stack that majorly contributes towards the modulation at very sub-volt bias. We achieve a 3.4 dB ER modulation while being 120 μm compact with an insertion loss of 5.8 dB for a Vpp bias of 0.2 V. The heterogeneous monolithic integration of ITO material provides high bandwidth ultra-low power consumption modulator device demonstrating a compact tunable critical-coupling modulator on a Si photonic platform paving the way towards CMOS-compatible compact, energy-efficient, and high-speed devices.

1.24 Method

Device Fabrication

A silicon photonic waveguide-based directional coupler from the Si DC-based ITO modulator (W x H: 500 nm x 220 nm) separated by a 900 nm gap. Both waveguides include grating couplers for optical signal input and output. Induced plasma dry etching with SF_6 and O_2 gases is used to etch silicon waveguides and grating couplers after lithography. The Al_2O_3 thin film is deposited using the atomic layer deposition process on the devices with the oxide serving as electrical isolation and a dielectric medium for the modulator. The ITO layer was deposited using ion beam deposition in the patterned region to isolate the ITO coverage in between the gap of two waveguides, covering the complete

coupling/active region length of 120 μm conformally. Electron beam lithography is used to pattern the electrical connections, which is then followed by Au / Ti (45 nm / 5 nm) electron beam evaporation deposition process. The sample was then annealed at 250°C for 2 hours at a 10°C / minute ramp rate. Finally, the sample was spin-coated with ~4 μm thick PMMA to function as cladding and improve the light coupling efficiency of the grating couplers. Using electron-beam lithography, a photoresist was developed on top of the electrical pads to open the contacts for rf probing after the clad deposition. The fabrication process flowchart schematic can be seen in Fig. 5.5.

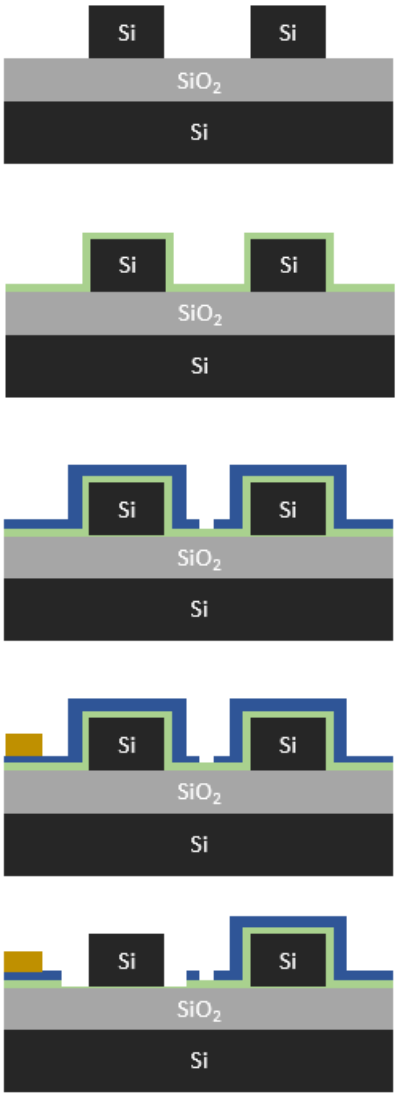

Figure 0.5 Nano-Fabrication Process steps for ITO integrated silicon directional coupler modulator

Device testing

A continuous wave laser at $\lambda = 1.55$ μm is coupled into the device being tested using a lensed fiber coupler and grating couplers. A high-speed photodetector is used to monitor the optical transmission and bandwidth response of the device. A vector network analyzer (65 GHz) is used for small signal response analysis. The signal was boosted using EDFA and an optical bandpass filter to overcome setup and device losses. The experimental setup for device characterization is detailed in Fig. 5.5.2.

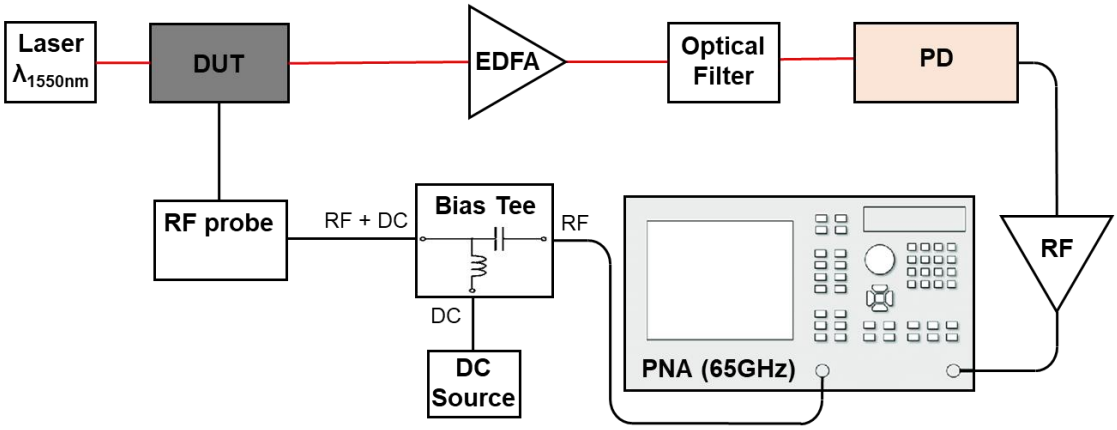

Figure 0.6 Schematic representation of the electro-optic measurement setup for high-speed small signal analysis.

1.25 References

[1] M. H. Tahersima et al, "Coupling-enhanced dual ITO layer electro-absorption modulator in silicon photonics," Nanophotonics, vol. 8, (9), pp. 1559-1566, 2019.

[2] V. J. Sorger et al, "Scaling vectors of attoJoule per bit modulators," Journal of Optics, vol. 20, (1), pp. 014012, 2017.

[3] J. B. Khurgin, "How to deal with the loss in plasmonics and metamaterials," Nature Nanotechnology, vol. 10, (1), pp. 2-6, 2015.

[4] E. Feigenbaum, K. Diest and H. A. Atwater, "Unity-order index change in transparent conducting oxides at visible frequencies," Nano Letters, vol. 10, (6), pp. 2111-2116, 2010.

[5] X. Liu et al, "Epsilon-near-zero Si slot-waveguide modulator," ACS Photonics, vol. 5, (11), pp. 4484-4490, 2018.

[6] E. Fortunato et al, "Transparent conducting oxides for photovoltaics," MRS Bull, vol. 32, (3), pp. 242-247, 2007.

[7] C. Ye et al, "A compact plasmonic MOS-based 2× 2 electro-optic switch," Nanophotonics, vol. 4, (3), pp. 261-268, 2015.

[8] A. Guo, G. J. Salamo, D. Duchesne, R. Morandotti, M. Volatier-Ravat, V. Aimez, G. A. Siviloglou, D. N. Christodoulides, "Observation of P T-symmetry breaking in complex optical potentials," Physical review letters, 103(9), 093902 (2009).

Hybrid Material Integration for Mid-Infrared Photonic Devices

1.26 Introduction

Integration of hybrid materials has emerged as a promising approach for developing mid-infrared (mid-IR) photonic devices with enhanced performance and functionality. By combining different materials with complementary properties, we can harness the advantages of each constituent to create novel and efficient photonic platforms operating in the mid-IR range. One notable hybrid integration strategy involves combining traditional semiconductor materials, such as silicon or germanium, with emerging two-dimensional materials, such as graphene, transition metal dichalcogenides (TMDs), or black phosphorus. These hybrid structures offer unique opportunities for tailoring the bandgap, carrier mobility, and light-matter interactions, crucial for mid-IR photonic devices. For example, [1] highlights the integration of graphene with silicon waveguides to achieve efficient light modulation and detection in the mid-IR range. Graphene's excellent conductivity, broad spectral response, and tunable Fermi level make it an ideal candidate for enhancing the

performance of mid-IR photonic devices. However, the absence of bandgap and flat band absorption response hinders the enhancement of light-matter interaction.

In addition, the integration of plasmonic materials, such as gold or silver nanoparticles, with dielectric waveguides has been extensively explored for mid-IR applications. Plasmonic structures enable subwavelength confinement and strong light-matter interactions, enhancing light absorption and emission in the mid-IR range. Moreover, the hybrid integration of quantum cascade lasers (QCLs) with photonic crystal cavities has shown promise for mid-IR light generation and sensing. By combining the high gain and tunability of QCLs with the mode confinement and enhanced light-matter interaction in photonic crystal structures, researchers have achieved compact and efficient mid-IR sources. The monolithic integration of QCLs with photonic crystal platforms for mid-IR applications enables a plethora of on-chip applications for sensing [2].

The integration of hybrid materials offers a versatile platform for developing mid-IR photonic devices with improved performance, such as enhanced light absorption, modulation, detection, and light generation. By leveraging the unique properties of different materials and exploiting their synergistic effects, researchers are pushing the boundaries of mid-IR photonics and paving the way for advancements in sensing, imaging, communications, and other mid-IR applications.

Topological insulators (TIs) have gained significant attention in the field of photodetection, particularly for mid-infrared (mid-IR) applications. These materials,

characterized by their nontrivial band topology, exhibit unique electronic and optical properties that make them highly suitable for efficient light detection in the mid-IR range. TIs possess a band gap in the bulk, but at the surface or interface, they host topologically protected surface states, known as Dirac states. These surface states have a linear dispersion relation, allowing for high carrier mobility and enhanced light-matter interactions. In the mid-IR region, where conventional photodetectors often face challenges, TIs offer a promising alternative for high-performance photodetection.

Mxene materials have shown great potential for mid-infrared (mid-IR) photodetection, offering unique advantages for this spectral range. Mxenes' unique properties, such as high conductivity, large surface area, and tunability, enable the realization of efficient mid-IR photodetectors with improved sensitivity and performance. These advancements pave the way for the development of advanced sensing technologies and open possibilities for the next generation of mid-IR photodetection devices. Mxenes, which are two-dimensional transition metal carbides, nitrides, or carbonitrides, possess remarkable electrical conductivity and large surface areas, making them attractive candidates for photodetector applications. Researchers have explored the performance of Mxene-based photodetectors in the mid-IR range, aiming to enhance responsivity, detectivity, and operational stability [3]-[5]. Several studies have demonstrated the excellent photodetection capabilities of Mxene materials in the mid-IR spectrum. The material exhibits a high responsivity and an impressive detectivity at room temperature. Furthermore, such a device demonstrates fast

response times and low dark current noise, essential for efficient mid-IR sensing and imaging applications. The Mxene heterostructures exhibit enhanced photoresponse and wide spectral range, making them promising for mid-IR photodetection [6]-[8].

1.27 Results and Discussion

Here, I investigate materials from MXene and topological insulator families for mid-IR photonics applications. The microscope image of the device can be seen in Fig. 6.2.1a showing the patterned contact opening and device structure. The Fourier transform infrared (FTIR) spectroscopy absorption response of Mxene materials can be observed from Fig. 6.2.1b showing broadband photodetection in the mid-IR range for $Ti_3C_2T_x$, Ti_3CNT_x, and $V_4C_3T_x$. The device was electrically characterized for resistance properties using current-voltage measurement as shown in Fig. 6.2.1c-d. The total resistance of the device is experimentally observed to be around 3.5 ohms. The experimental resistance measurement shows potential towards gigahertz bandwidth operation for high-speed photodetectors and modulators in mid-IR regime Fig. 6.2.1d.

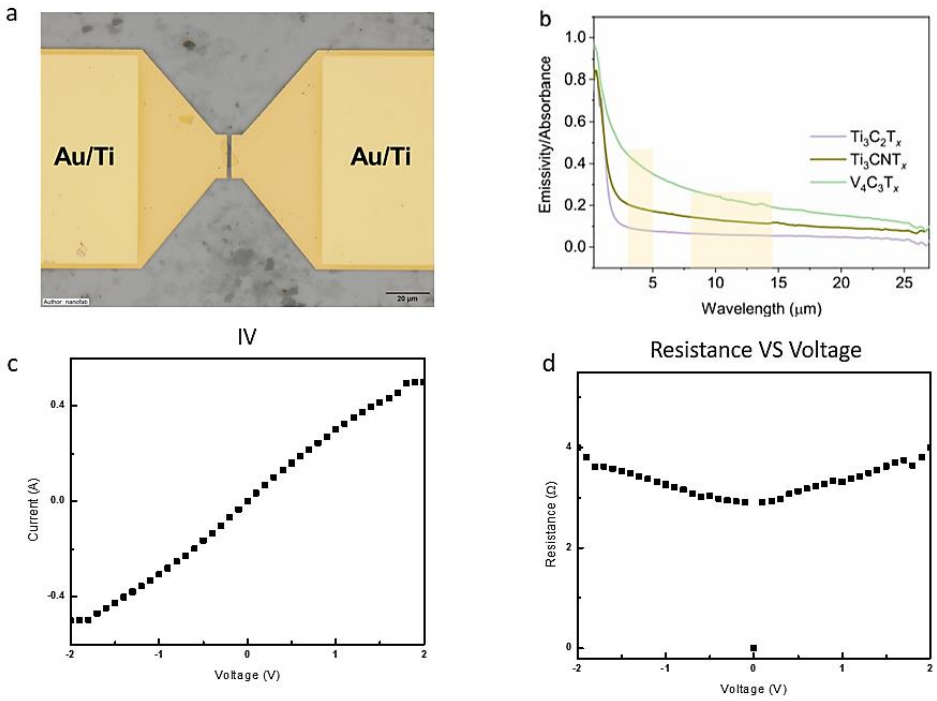

Figure 0.1 MXene-based mid-IR Photodetector (a) Optical image of the free space photodetector device (b) Fourier transform infrared spectroscopy response of the $Ti_3C_2T_x$, Ti_3CNT_x, and $V_4C_3T_x$ materials showing high bandwidth photodetection capability and photo absorbance (c) I-V characteristics of the device tested at 2 μm wavelength (d) Resistance change as a function of voltage calculated to show linear electrical response.

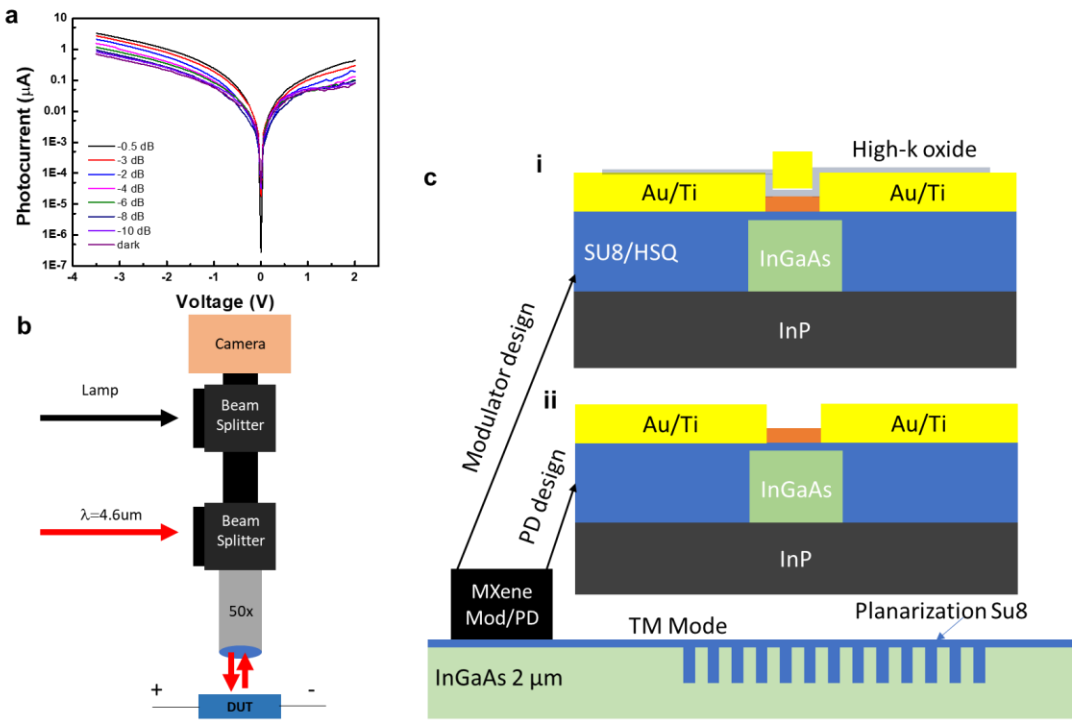

Figure 0.2 Mid-IR Photodetector (a) Optical image of the free space photodetector device (b) Optical response of the Ti3C4 compared to other Mxene materials showing high bandwidth photodetection capability (c) I-V characteristics of the device (d) Resistance change as a function of voltage calculated to show linear electrical response.

I further investigated materials from the topological insulators family for designing a polarization-sensitive pn-junction heterogeneous structure-based photodetector. The bandgap of Bi_2Te_3 and Sb_2Te_3 is favorable for building mid-IR photodetectors and modulators. A pn-junction was built using Bi_2Te_3 and Sb_2Te_3 and was electrically contacted with Au/Ti pads as seen in Fig. 6.2.3a. A spectral response at a fixed polarization for maximum detection was tested with a range of wavelengths (500 nm to 900 nm). The

hybrid absorption peak due to the formation of heterojunction was observed at around 795 nm. This peak response can be modulated by changing the polarization of the incident light on the device. Such unique attributes of the device can be further engineered for on-chip integrated photodetectors and free space photo-absorbers or sensors.

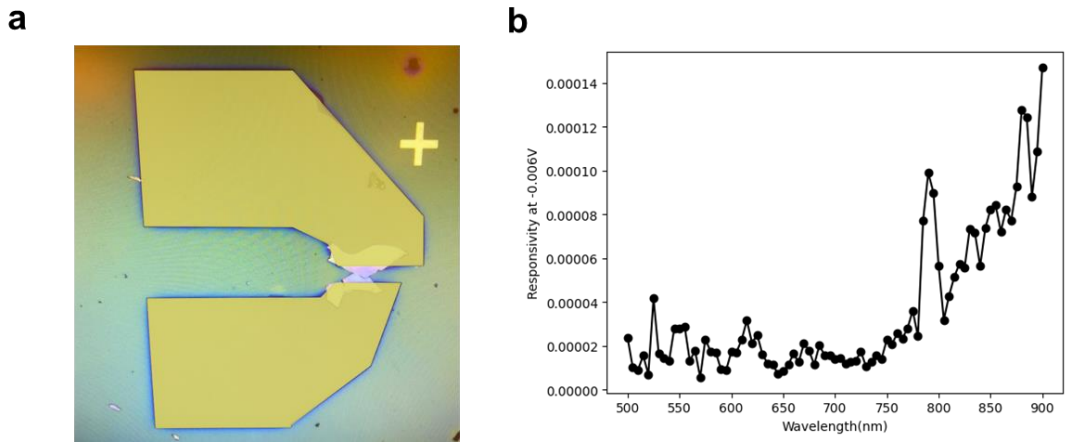

Figure 0.3 Topological Insulator-based polarization-sensitive photodetector (a) Optical image of the free space pn-junction-based photodetector device built by Bi_2Te_3 and Sb_2Te_3 flakes (b) Optical response of the device over 500 nm – 900 nm wavelength for broadband operation. The response was captured by tunning polarization of the device until the maximum output was observed.

1.28 Method

The solution of 15% Ti3C4 flakes suspended in DI water was spin-coated on a 50 nm thin SiO2 substrate on Si. The flakes were patterned using an e-beam lithography process to design electrical contacts on top. Pre-designed metal alignment markers on the chip were used to precisely align the position of the flakes on the substrate to form electrical contacts. The channel length for the device here is 2 μm and contact pads are 80x80 μm.

1.29 Conclusion

In conclusion, the integration of hybrid materials, particularly topological insulators, and MXenes, has shown great potential for the development of mid-infrared (mid-IR) photonic devices. Topological insulators exhibit unique electronic and optical properties that enable efficient light-matter interactions in the mid-IR range, making them promising candidates for photodetection, modulators, and sensors. MXenes, on the other hand, offer exceptional electrical conductivity, tunable optical properties, and high carrier mobility, which can be leveraged for enhancing the performance of mid-IR photonic devices.

The combination of topological insulators and MXenes in hybrid structures allows for the exploitation of their complementary properties. For instance, the topological surface states in topological insulators can enable efficient photogeneration and detection of mid-IR photons, while the conductivity and tunability of MXenes enhance device performance and enable dynamic control of light-matter interactions. This hybrid integration approach opens new avenues for designing and fabricating mid-IR photonic devices with improved sensitivity, responsivity, and functionality.

The development of hybrid mid-IR photonic devices based on topological insulators and MXenes holds great promise for various applications. For instance, in sensing and imaging, these devices can enable high-resolution and selective detection of specific mid-IR wavelengths, facilitating the identification of chemical compounds and biomolecules.

In communication systems, the integration of topological insulators and MXenes can lead to high-speed and energy-efficient modulators for mid-IR optical signal processing.

However, further research and development are still needed to fully exploit the potential of hybrid mid-IR photonic devices based on topological insulators and MXenes. Challenges such as material integration, device fabrication, and optimization of device performance need to be addressed. Nonetheless, the progress made so far in this field highlights the exciting opportunities and potential breakthroughs that can be achieved by combining these two classes of materials in hybrid structures for mid-IR photonics. Such devices and novel material families provide a great platform for potential high-performance photonic and optoelectronic devices.

1.30 References

[1] S. Yuan *et al*, "Room Temperature Graphene Mid-Infrared Bolometer with a Broad Operational Wavelength Range," *ACS Photonics*, vol. 7, *(5)*, pp. 1206-1215, 2020. Available: http://dx.doi.org/10.1021/acsphotonics.0c00028. DOI: 10.1021/acsphotonics.0c00028.

[2] S. Chakravarty *et al*, "Monolithic integration of quantum cascade laser, quantum cascade detector and slotted photonic crystal waveguide for absorbance sensing from λ=3-15μm," in Jan 1, 2018, pp. 1.

[3] Y. Tian *et al*, "Air-Stable Flexible Photodetector Based on MXene–Cs3Bi2I9 Microplate Schottky Junctions for Weak-Light Detection," *ACS Applied Materials &*

Interfaces, vol. 15, *(10),* pp. 13332-13342, 2023. Available: http://dx.doi.org/10.1021/acsami.2c22691. DOI: 10.1021/acsami.2c22691.

[4] L. Gao *et al,* "Applications of Few-Layer Nb2C MXene: Narrow-Band Photodetectors and Femtosecond Mode-Locked Fiber Lasers," *ACS Nano,* vol. 15, *(1),* pp. 954-965, 2021. Available: http://dx.doi.org/10.1021/acsnano.0c07608. DOI: 10.1021/acsnano.0c07608.

[5] C. Yi *et al*, "MXene-GaN van der Waals Heterostructures for High-Speed Self-Driven Photodetectors and Light-Emitting Diodes," *Advanced Electronic Materials,* vol. 7, *(5),* pp. 2000955-n/a, 2021. Available: https://onlinelibrary.wiley.com/doi/abs/10.1002/aelm.202000955. DOI: 10.1002/aelm.202000955.

[6] Z. Wang *et al,* "MXene Photonic Devices for Near-Infrared to Mid-Infrared Ultrashort Pulse Generation," *ACS Applied Nano Materials,* vol. 3, *(4),* pp. 3513-3522, 2020. Available: http://dx.doi.org/10.1021/acsanm.0c00241. DOI: 10.1021/acsanm.0c00241.

[7] C. Wei *et al,* "MXene-Ti 3 C 2 T x for watt-level high-efficiency pulse generation in a 2.8 μm mid-infrared fiber laser," *Photonics Research (Washington, DC),* vol. 8, *(6),* pp. 972, 2020. . DOI: 10.1364/PRJ.388930.

[8] C. Shang *et al,* "Nonlinear optical properties of MXene and applications in broadband ultrafast photonics," *Journal of Alloys and Compounds,* vol. 918, pp. 165580, 2022.

Available: https://dx.doi.org/10.1016/j.jallcom.2022.165580. DOI:

10.1016/j.jallcom.2022.165580.

Conclusion and Outlook

In conclusion, the integration of emerging materials holds great promise for the development of high-performance photonic devices. The combination of topological insulators and MXenes, along with the integration of other 2D materials and transparent conductive oxides like ITO, enables enhanced light-matter interaction and paves the way for advanced photonic devices such as modulators and photodetectors. These materials offer unique properties such as high carrier mobility, tunable optical properties, and strong light-matter interaction, which are crucial for achieving efficient and compact photonic integrated circuits (PICs). By effectively integrating these materials, researchers can overcome challenges in coupling light between different components and enhance the overall performance of PICs in terms of size, speed, and power efficiency.

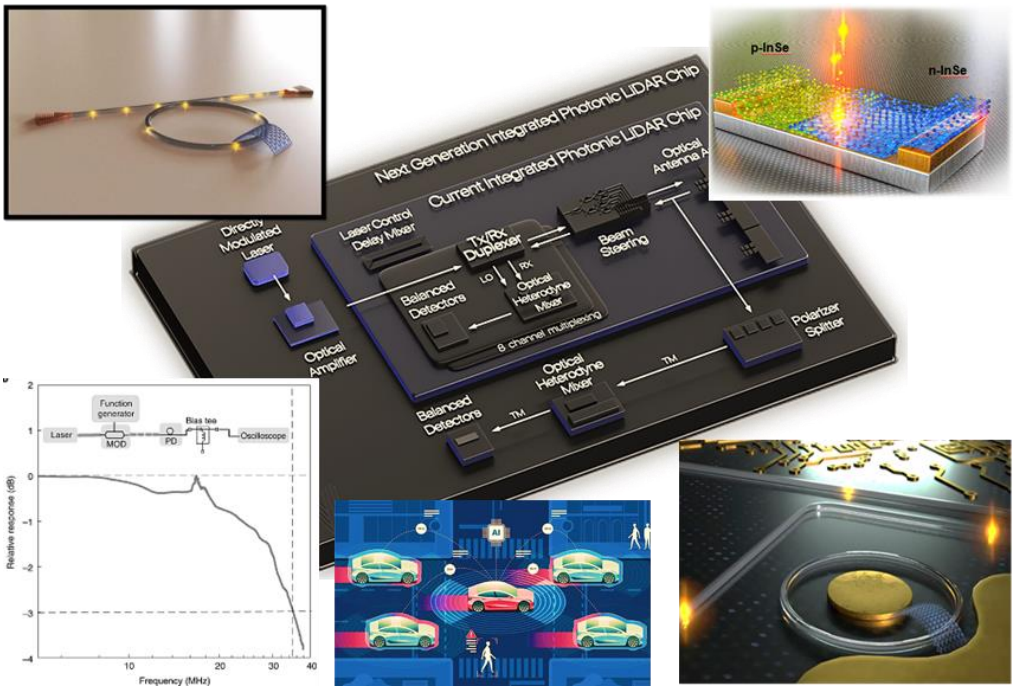

Figure 0.1 Hybrid Heterogeneous integration of novel materials for high-performance photodetectors and sensors for LiDAR detection and SWAP applications

The integration of emerging materials also opens possibilities for various applications in fields such as communication systems, data centers, telecommunication networks, and quantum computing. The development of efficient modulators based on topological insulators, MXenes, and other advanced materials enables high-speed and energy-efficient optical signal processing. Additionally, the utilization of these materials in photodetectors allows for sensitive and selective detection of specific wavelengths in the mid-infrared range, enabling advancements in fields such as sensing, imaging, and LiDAR technology.

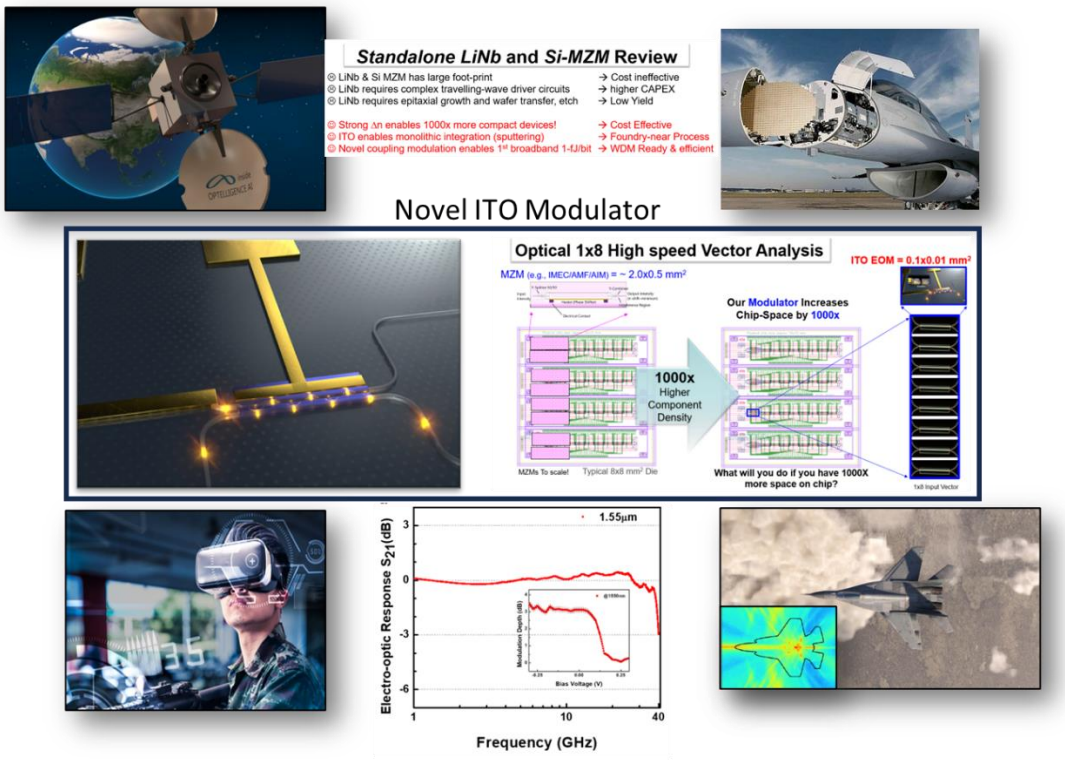

Figure 0.2 Towards High-Speed Energy Efficient photonic integrated circuits (PICs) development for Next Generation LIDAR and Photonics Computing

However, further research and development are still needed to fully unlock the potential of emerging material integration for high-performance photonic devices. Challenges such as material compatibility, fabrication techniques, and optimization of device performance need to be addressed. Nonetheless, the progress made so far in this field shows promising results and points toward a future where photonic devices can achieve unprecedented performance and open up new frontiers in technology and scientific advancements.

I plan to further develop solutions to such challenges by focusing on LiDAR signal detection and signal generation using beam steering. Using novel materials like ITO, TIs,

Mxene, and 2D materials and heterogeneously integrating these on PICs will further open wide applications in the field of photonics. Developing mid-IR photonic devices would be another aspect of the future to be pursued for FSO communication and gas sensing.